Model-based control-oriented scenario construction in tokamaks

Xiao Song

▶ To cite this version:

Xiao Song. Model-based control-oriented scenario construction in tokamaks. Automatic Control Engineering. COMUE Université Côte d'Azur (2015 - 2019), 2019. English. NNT : 2019AZUR4089 . tel-02869594

HAL Id: tel-02869594
https://theses.hal.science/tel-02869594

Submitted on 16 Jun 2020

$$\rho\left(\frac{\partial v}{\partial t} + v \cdot \nabla v\right) = -\nabla p + \nabla \cdot T + f$$

$$e^{i\pi} + 1 = 0$$

THÈSE DE DOCTORAT

Optimisation automatisée de scénarios pour le système
de champ magnétique poloïdal dans les tokamaks

Model-based control-oriented scenario construction in tokamaks

Xiao Song

Laboratoire Jean-Alexandre Dieudonné (LJAD)

Présentée en vue de l'obtention du grade de docteur en Sciences pour l'ingénieur
d'Université Côte d'Azur

Dirigée par : Blaise FAUGERAS
Co-encadrée par : Holger HEUMANN

Soutenue le 29 novembre 2019 **devant le jury composé de :**
Guido HUIJSMANS, Professor, Eindhoven University of Technology (Rapporteur)
Emmanuel WITRANT, Maître de Conférence, Université Grenoble Alpes (Rapporteur)
Jacques BLUM, Professeur Emérite, Université Côte d'Azur
Hervé GUILLARD, Directeur de Recherche, INRIA, Sophia Antipolis
Blaise FAUGERAS, Ingénieur de Recherche, CNRS, Université Côte d'Azur
Holger HEUMANN, Docteur, Ingénieur dans l'industrie bancaire
Eric NARDON, Ingénieur de Recherche, CEA (Encadrant CEA)

Abstract

This thesis is concerned with developing and applying numerical tools in order to optimize the operation of the poloidal magnetic field (PF) system in tokamaks. The latter consists of a set of coils and power supplies which have the purpose of controlling the plasma shape and position, as well as driving the plasma current. The global context of our work is introduced in **Chapter 1**.

Chapter 2 describes our approach, which consists in applying optimal control methods to the Free-Boundary plasma Equilibrium (FBE) problem, which is composed of force balance equations in the plasma coupled to Maxwell's equations in the whole tokamak. The numerical tool employed here is the FEEQS.M code, which can be used either (in the "direct" mode) as a solver of the FBE problem or (in the "inverse" mode) to minimize a certain function under the constraint that the FBE equations be satisfied. Each of these 2 modes ("direct" and "inverse") subdivides into a "static" mode (which solves only for a given instant) and an "evolution" mode (which solves over a time window). The code is written in Matlab and based on the Finite Elements Method. The non-linear nature of the FBE problem is dealt with by means of Newton iterations, and Sequential Quadratic Programming (SQP) is used for the inverse modes. We stress that the "inverse evolution" mode is a unique feature of FEEQS.M, as far as we know.

After describing the FBE problems and the numerical methods and some tests of the FEEQS.M codes, we present 2 applications.

The first one, described in **Chapter 3**, concerns the identification of the operating space in terms of plasma equilibrium in the ITER tokamak. This space is limited by the capabilities of the PF system, such as the maximum

possible currents, field or forces in the PF coils. We have implemented penalization terms in the "objective" function (i.e. the function to be minimized) of the "inverse static" mode of FEEQS.M in order to take some of these limits into account. This allows calculating in a fast, rigorous and automatic way the operating space, taking these limits into account. This represents a substantial progress compared to "traditional" methods involving much heavier human intervention.

The second application, presented in **Chapter 4**, regards the development of a fast transition from limiter to divertor plasma configuration at the beginning of a pulse in the WEST tokamak, with the motivation of reducing the plasma contamination by tungsten impurities. Here, FEEQS.M is used in "inverse evolution" mode. Data from a WEST experimental pulse is used to set up the simulation. The FEEQS.M calculation then provides optimized waveforms for the PF coils currents and power supplies voltages to perform a fast limiter to divertor transition. These waveforms are first tested on the WEST magnetic control simulator (which embeds FEEQS.M in "direct evolution" mode coupled to a feedback control system identical to the one in the real machine) and then on the real machine. This allowed speeding up the transition from ~ 1 s to 200 ms.

Keyword : Tokamak, plasma scenario, ITER, optimal control.

Résumé

Cette thèse concerne le développement et l'application d'outils numériques permettant d'optimiser l'utilisation du système de champ magnétique poloïdal dans les tokamaks. Ce dernier est constitué d'un ensemble de bobines et d'alimentations électriques dont le rôle est de contrôler la forme et la position du plasma ainsi que de générer le courant plasma. Le contexte général de notre travail est décrit dans le Chapitre 1.

Le Chapitre 2 présente notre approche du problème, qui consiste à appliquer des méthodes de contrôle optimal au problème d'Equilibre à Frontière Libre (EFL). Ce dernier est composé d'une équation d'équilibre des forces dans le plasma couplée aux équations de Maxwell dans l'ensemble du tokamak. L'outil numérique employé ici est le code FEEQS.M, qui peut être utilisé soit (dans le mode dit « direct ») pour résoudre le problème EFL soit (dans le mode dit « inverse ») pour minimiser une certaine fonction-coût sous la contrainte que les équations d'EFL soient satisfaites. Chacun de ces deux modes (« direct » et « inverse ») se subdivise en un mode « statique » (qui s'applique à un instant donné) et un mode « évolutif » (qui s'applique sur un intervalle de temps). Le code est écrit en langage Matlab et utilise la méthode des éléments finis. La nature non-linéaire du problème d'EFL est traitée au moyen d'itérations de Newton, et une méthode de type programmation séquentielle quadratique est appliquée pour les modes inverses. Nous soulignons que le mode « inverse évolutif » est, à notre connaissance, une caractéristique unique de FEEQS.M.

Après avoir décrit les problèmes d'EFL ainsi que les méthodes numériques utilisées et quelques tests de FEEQS.M, nous présentons deux applications. La première, décrite dans le Chapitre 3, concerne l'identification du domaine opérationnel en termes d'équilibre plasma pour le tokamak ITER. Ce domaine est contraint par les limites du système de champ poloïdal portant par exemple sur les courants, forces ou champs magnétiques dans les bobines. Nous avons implémenté des termes de pénalisation dans la fonction-coût du mode « statique inverse » de FEEQS.M pour prendre en compte ces

limites. Ceci nous a permis de calculer de façon rapide, rigoureuse et automatique le domaine opérationnel, ce qui représente un progrès substantiel par rapport aux méthodes ≪ traditionnelles ≫ qui impliquent une intervention humaine beaucoup plus lourde.

La seconde application, présentée au Chapitre 4, concerne le développement d'une transition rapide d'une configuration plasma ≪ limitée ≫ à une configuration ≪ divergée ≫ au début d'une décharge dans le tokamak WEST. La motivation est ici la réduction de la contamination du plasma par les impuretés de tungstène. A cette fin, le code FEEQS.M est utilisé dans son mode ≪ inverse évolutif ≫. Des données expérimentales de WEST sont utilisées pour paramétrer la simulation. Le calcul FEEQS.M fournit alors des trajectoires optimales pour les courants des bobines poloïdales et les voltages de leurs alimentations afin d'obtenir une transition ≪ limité ≫ - ≪ divergé ≫ rapide. Ces trajectoires sont testées d'abord sur le ≪ simulateur de vol ≫ WEST (qui embarque FEEQS.M en mode ≪ direct évolutif ≫ couplé à un système de rétroaction identique à celui utilisé dans WEST) et ensuite expérimentalement sur WEST. Ceci a permis de passer d'une transition durant 1s à une transition durant 200ms.

Mots − clés : Tokamak, scénario plasma, ITER, contrôle optimal.

Acknowledgment

I would like to thank firstly my thesis director Blaise Faugeras. Thank you to read my manuscript point by point and give very fruitful suggestions, and thank you to prepare the paper works for administration at the university that sounded easily but time-consumed in reality. I wish to show my great gratitude to thesis co-director Holger Heumann, your attitude toward work and distinguished mathematical knowledge influence me so much, and I am sure they will benefit me in the rest of my life. I also want to appreciate you to develop the FEEQS.M code and the dedicated works, which help me to finish the main parts of manuscript. Your fast response to my requests, always solves the problems in time. This is not easy for you, especially after you changed your work which is totally different to the previous one. I would also like to thank Jacques Blum from the Nice university, for his supporting of the collaboration between LJAD and CEA IRFM.

I am also grateful to my thesis co-director Eric Nardon at CEA, you have spent a lot of time to work with me, from the PhD proposal to the work direction, publication, manuscript etc. You help me not only on the academical points, but also on the life spent in France, and you serve me more than a student, but like a friend and brother. All the help you have done for me, will also make me beneficial in the rest of my career.

I would like to thank Rémy Nouailletas, who is the control engineer at CEA, thank you to teach me the knowledge about magnetic control, and allow me to use your simulator to test and analysis my simulation results. I also wish to show my special thanks to J.F. Artaud, your expertise in plasma physics gives me an open way to deal with the encountered problems. I also would like to appreciate P. Moreau, P. Spuig, D. Douai, S. Sanchez, E. Poitevin and K. Ruiz, thank you to help me when I am working at CEA.

Many thanks to my colleagues and friends, Drs. X.L. Zou, Zh.X. Chen, Y. Sun, T.B. Wang, and the PhD candidates R. Mao, A.Sh. Liang and S. Sridhar at CEA Cadarache, without your accompaniment and leisure conversations, it is impossible for me to spend such a long time in France.

Contents

CONTENTS

Chapter 1

Introduction

1.1   Energy consumption and nuclear energy

1.1.1   Energy consumption around the world
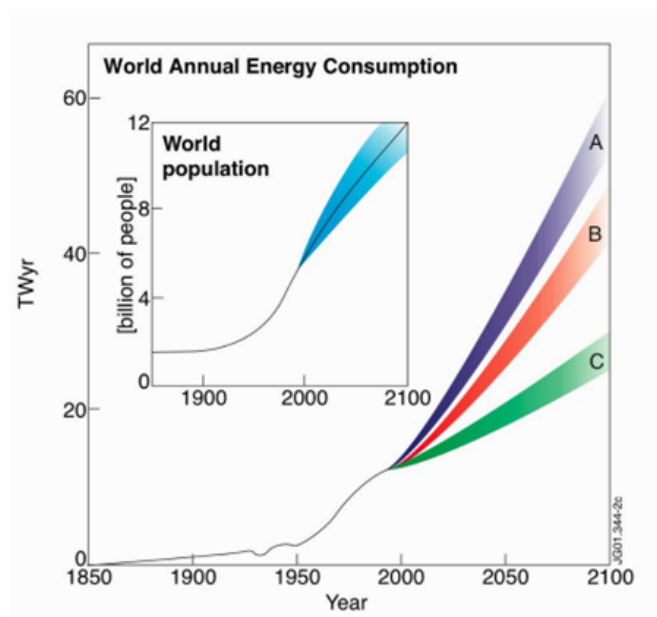
Figure 1.1: World annual energy consumption and population (inserted). - The statistic and estimations of the evolution of annual world primary energy consumption and world population. Note that the predictions are based on three methods in [1], and the colored bands are the error bars in the predictions.

People nowadays are more and more worried about energy issues on Earth, since the

1. INTRODUCTION

energy consumption is soaring with the growth of the total population. It is reported in [2] that the total world annual energy consumption and the population are raised shapely from the early 1950s, and they will *"explode"* from now to 2100, just as it is shown in figure 1.1, where the predictions by three different scenarios [1] are given in colored bands.

When taking a look at the compositions of energy production in table 1.1 and the contributions of different energy sources in table 1.2, one can find that nearly 90 percents of the energy consumption now on Earth are produced by burning fossil fuels. Worst of all, those fuels will be ran out of in a few hundred years if the current situation is not changed.

Fuel	Reserved (2009)	Years left at the current consumed rate
Coal	0.9×10^{12} ton	210
Crude oil	1.3×10^{12} barrels	$30 \sim 40$
Natural gas	$190 \times 10^{12}\ m^3$	$60 \sim 70$
Uranium (ore)	4.7×10^6 ton	$85 \sim 270$ *
Uranium (sea water)	4.5×10^9 ton	$81000 \sim 260000$ **

$*$ assuming light water reactor;

$**$ when breeder technology is available.

Table 1.1: Available years for different fuels at the current consumption rate [2].

Primary energy source	Contribution to energy production/ % (2008)
Oil	33.7
Coal	23.8
Gas	29.6
Fission	5.2
Hydro-electricity	6.4
Solar,wind,wood,waste	1.3

Table 1.2: Contributions of different energy sources to the total energy production [3].

In addition to the shortage of those fossil fuels, the emission of CO_2 (shown in figure 1.2), from their burning, is increasing exponentially. The large amount of released CO_2 will pollute the atmosphere, modify the climate, rise the sea level, and break the ecological balance on Earth.
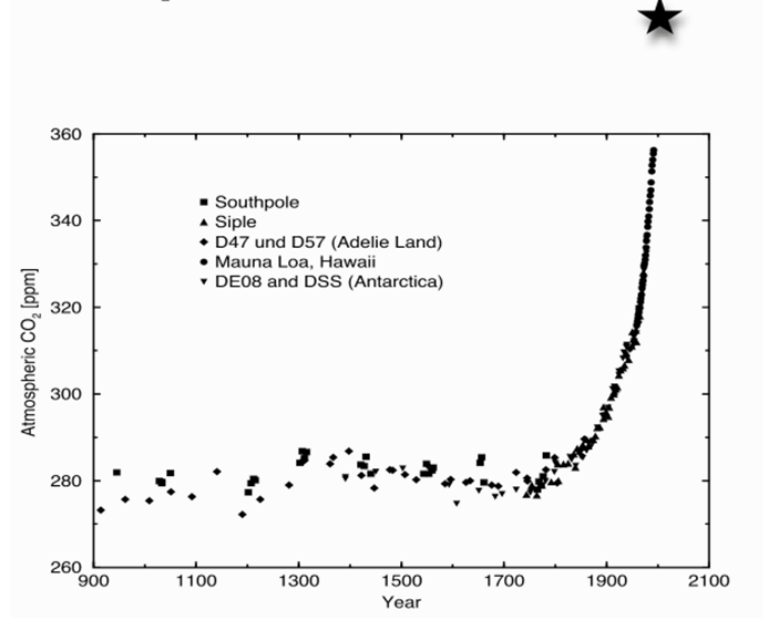
Figure 1.2: CO_2 **concentration in the atmosphere (in ppm).** - The black star out of the figure is the CO_2 level in 2008 [4].

1.1.2 Nuclear fusion energy and controlled fusion reaction

In order to solve the energy crisis addressed above, people have to seek some other ways to explore the clean (less or no environmental pollution) and sustainable (for an adequate long time) energies.

Nuclear fusion may be a way to produce relative clean and tremendous amount of energy, which could fulfill the world energy consumption for billions of years. The possible fusion reactions are the combinations of deuterium (D) and deuterium (D) plasma (in which the density of electron equals to the charged number × ion density), deuterium (D) and its isotope tritium (T) plasma, deuterium (D) and helium (He) plasma:

$$
\begin{aligned}
{}_1^2D + {}_1^2D &\rightarrow {}_2^3He(0.82\ MeV) + {}_0^1n(2.45\ MeV) \\
{}_1^2D + {}_1^3T &\rightarrow {}_2^4He(3.52\ MeV) + {}_0^1n(14.06\ MeV) \\
{}_1^2D + {}_2^3He &\rightarrow {}_2^4He(3.67\ MeV) + {}_1^1p(14.67\ MeV)
\end{aligned}
\tag{1.1}
$$
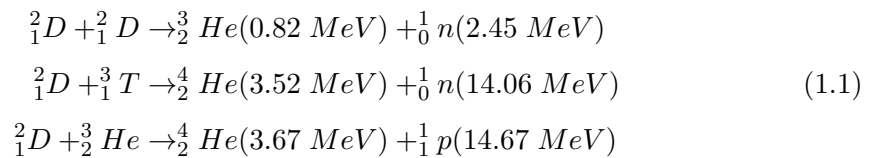
The products of the fusion reactions in equation (1.1) are charged helium (He^{2+}, which is also called α particle), high energy neutron (n) and proton (p^+). The second

one is usually investigated in the daily laboratories on Earth, since it can release huge energy ($n \sim 14.06$ MeV) and has the largest reaction cross-section in low energy of the range of 10 keV from figure 1.3.
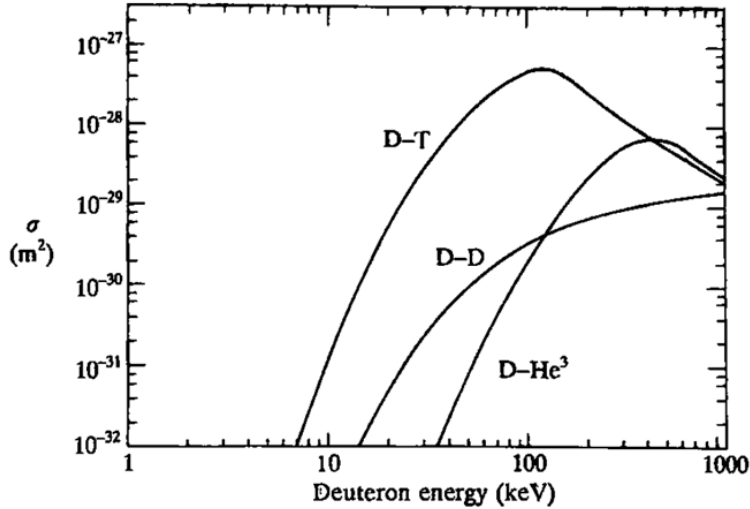
Figure 1.3: Cross-sections for the reactions D-D, D-T and D-^{3}He. - The data in this figure are from [5]

The ignition condition for the fusion reactions in equation (1.1) is given generally as a candidate on the fusion triple product in [6]:

$$n_i T_i \tau_E \geqslant 3 \times 10^{21} m^{-3} keV \cdot s \tag{1.2}$$

where n_i and T_i are the density and temperature of the ions, τ_E is the energy confinement time which is defined as $\tau_E = W/P$, where W is the thermal energy stored in the hot plasma and P is the heating power.

There are two kinds of schemes being explored to obtain fusion in daily experiment. One is called inertial confinement fusion, e.g., the National Ignition Facility (NIF) [7] in Lawrence Livermore National Lab of the US. It utilizes tested energetic lasers to bombard a solid target that is constituted of D and T, in order to trigger fusion reaction in the time range of several nanoseconds (10^{-9}s), this kind of fusion reaction is usually designed with the military intentions. The other main scheme is named as magnetic confinement fusion, in which a strong magnetic field is produced to confine the plasma in a torus, such as tokamak [5], stellarator [8], and spheromak [9], typically

the τ_E in these machines varies from several milliseconds (ms) to one second (s). The tokamak is considered as the most plausible way to achieve the aim of nuclear fusion energy utilization, and it is the most popular device around the world to research the *controllable* fusion energy.

1.2   Tokamak

Tokamak is a magnetic confinement fusion device, where the magnetic field is produced by external coils and the plasma current. The plasma is *controlled* by the magnetic field in a vacuum vessel, and external powers are injected into the plasma to increase the triple product in (1.2), then approach ignition.
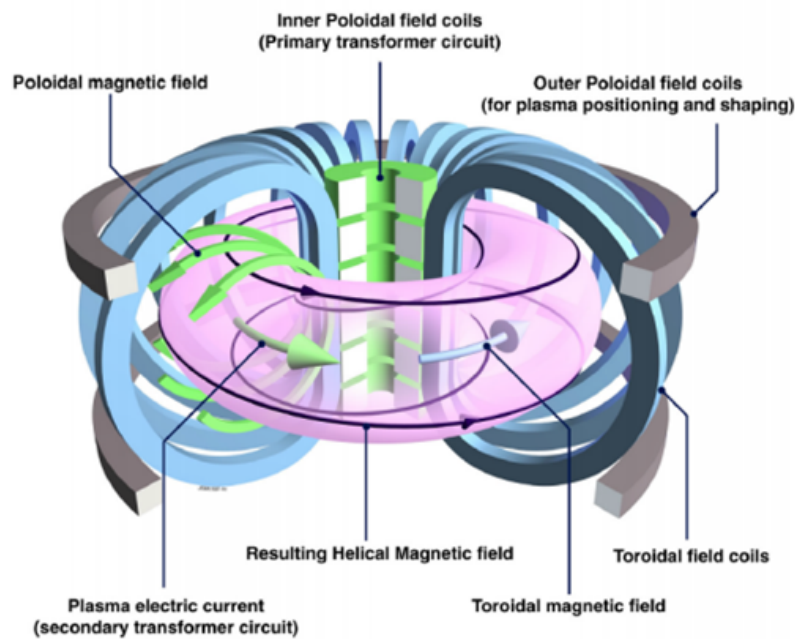
Figure 1.4: Simplified tokamak structure -

A simple sketch of a tokamak is shown in figure 1.4. There are two kinds of magnetic fields, i.e. toroidal and poloidal magnetic fields. The toroidal magnetic field is produced by the toroidal field (TF) coils (the sky-blue coils in figure 1.4), it is the principal magnetic field to control plasma. The poloidal magnetic field is produced by the plasma current and the poloidal field coils. The poloidal field coils are divided into two parts,

one is the green coil in the inner center of the torus (see figure 1.4), it is called central solenoid (CS) coil, which is used to provide the energy to start the plasma and sustain the plasma current. The other poloidal field coil is called poloidal field (PF) coil, i.e. the gray coil in figure 1.4, it is used to control the plasma position and achieve different shapes. Tokamak works as a transformer, in which the toroidal plasma current is the secondary winding and the CS coil is the primary winding.
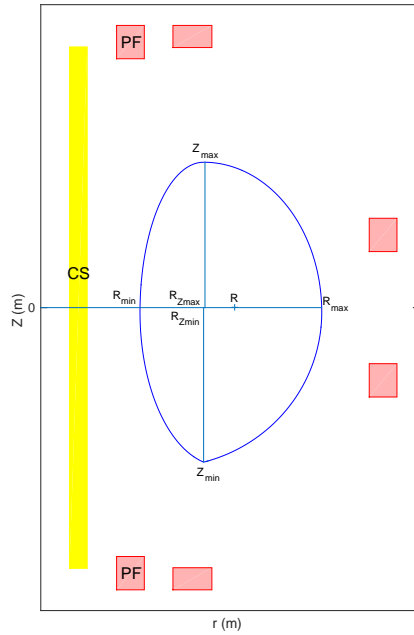
Figure 1.5: Cross-section of a tokamak. - The yellow rectangle is the CS coil and red ones are the PF coils, the blue ellipsoid is the plasma boundary.

Figure 1.5 shows the cross-section of a tokamak. The plasma is confined inside the blue ellipsoid, which is called the plasma boundary. It is assumed that the toroidal plasma current is only inside the boundary. There are some basic definitions for the plasma geometry in a tokamak:

- Major radius: R (m).

- Minor radius: a (m) $=(R_{max} - R_{min})/2$.

- Aspect ratio: A = R/a; inverse aspect ration $\epsilon = 1/A$.

- Elongation: $\kappa_{up} = Z_{max}/a$; $\kappa_{down} = -Z_{min}/a$.

- Triangularity: $\delta_{up} = (R - R_{Zmax})/a$; $\delta_{down} = (R - R_{Zmin})/a$.

The D and T fusion reaction will not happen in a tokamak if there is no external power injected into the plasma, because the plasma resistivity decreases as $T^{-3/2}$, so when the plasma current and temperature rise, the Ohmic heating (heat only by the CS and PF coils) decreases [10]. In addition to increasing the triple product, additional heating schemes may be used to drive plasma current, allowing access to steady-state operation. The cardinal categories of the heating schemes are:

- Waves drive: electron cyclotron current drive (ECCD) [11, 12], ion cyclotron current drive (ICCD) [13] and lower hybrid current drive (LHCD) [14].

- Beam drive: neutral beam current drive (NBCD) [15].

The only tokamaks around the world that have produced non-negligible fusion power are the Tokamak Fusion Test Reactor (TFTR) in Princeton [16] and the Joint European Torus (JET) in Oxford [17]. The maximum fusion power are 10.7 MW and 16.1 MW, respectively.

1.2.1 ITER project

It is generally known [18] that the ignition condition of (1.2) is easier to reach in a large tokamak, as can be seen in the τ_E scaling law [19]:

$$\tau_E^L = 0.023 I_P^{0.96} B_T^{0.03} P_{aux}^{-0.73} n_0^{0.40} M_P^{0.20} R^{1.83} \epsilon^{0.06} \kappa^{0.64}$$
$$\tau_{E,IPB98(y,2)}^{ELMy} = 0.0562 I_P^{0.93} B_T^{0.15} P_{aux}^{-0.69} n_0^{0.41} M_P^{0.19} R^{1.97} \epsilon^{0.58} \kappa^{0.78} \tag{1.3}$$

where I_P and B_T are the plasma current and toroidal magnetic field, n_0 is the plasma line averaged density, M_P is the averaged ion mass and P_{aus} is the injected power. It is indeed visible from the scaling law that τ_E increases fast with R. The L and $ELMy$ in equation (1.3) denote the confinement modes which are called L-mode and H-mode. H-mode has a higher confinement than L-mode, and that is why the H-mode selected as a reference for ITER operation. H-mode was obtained in many devices (ASDEX [20], ASDEX-U [21], JET[22], JT-60U [23], DIIID [24], Alcator C-Mod [25], TCV [26],HL-2A[27], EAST [28] and KSTAR [29] etc).

The International Thermonuclear Experimental Reactor (ITER) in figure 1.6 is the largest tokamak under construction in the world [30]. Its budget up to 2010 is more

than 15 billion Euros, which is invested by the six main economic powers [31]. The objective of ITER is to demonstrate the scientific and technological feasibility of fusion energy [32]. The main parameters are given in table 1.3. One of the prime targets of the ITER project is to validate $Q_{fusion} = 10$:

$$Q_{fusion} = \frac{P_{fusion}}{P_{auxiliary}} \tag{1.4}$$

where P_{fusion} is the fusion power, and $P_{auxiliary}$ is the external input power. It means the output power will be 10 times more than the total input power, and ITER will be the first tokamak where plasma self-heating will dominate over external heating.
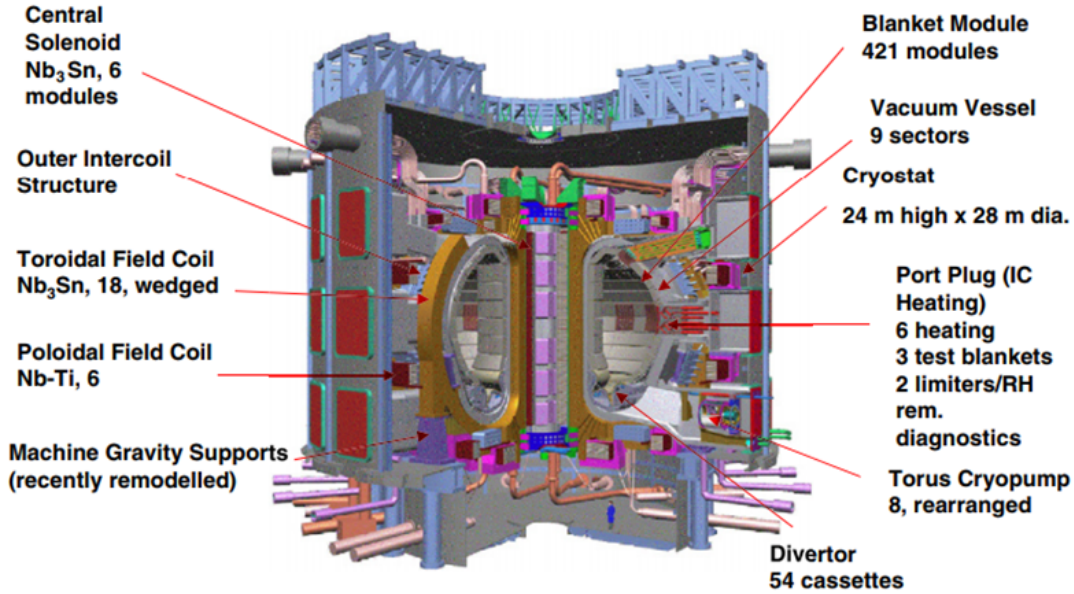
Figure 1.6: ITER - the largest tokamak under construction in the world.

1.2.2 WEST tokamak

In order to provide reliable data and experience for future ITER operation, the study of present tokamaks is mainly focused on the physical and engineering problems that are relevant for ITER.

The Tungsten (W) Environment in Steady State Tokamak (WEST) [33] is an upgrade from the Tore Supra tokamak [34] in order to test the ITER-like plasma wall interaction material and validate steady-state plasma scenarios in a W machine[35].

Parameter	Attributes
Fusion power (P_{fusion})	500 MW ($700 MW$)*
Fusion power gain (Q_{fusion})	$\geqslant 10$ (for 400s inductive scenario)
	$\geqslant 5$ (for steady-state scenario)
Plasma major/minor (R/a) radius	6.2/2.0 m
Plasma vertical elongation/triangularity	1.85/0.48
Plasma current (I_P)	15 MA ($17 MA$)*
Toroidal field at 6.2 m	5.3 T
Injected power ($P_{auxiliary}$)	73 MW ($110 MW$)**
Plasma volume (V_P)/surface area (S_P)/cross section area	830 m^3/690 m^2/ 22 m^2

$*$Can be increased with limitation on burn duration.

** A total plasma heating power of 110 MW may be installed.

Table 1.3: ITER main parameters and operational capabilities.
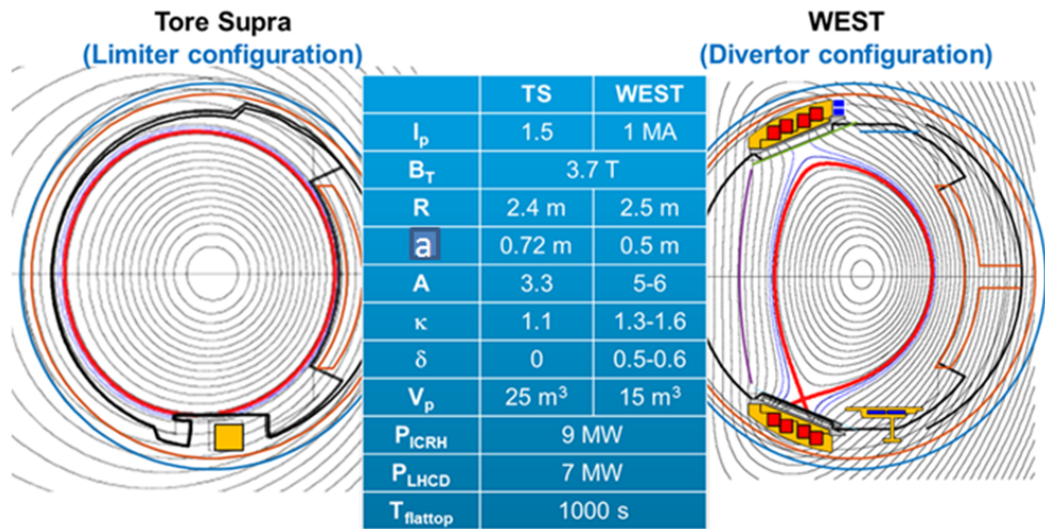
Figure 1.7: Tore Supra is updated to WEST - Left: Tore Supra cross-section and circular shape (red line); middle: the main parameters of Tore Supra and WEST;right: west cross-section and elongated (divertor) shape (red line).

The main difference between Tore Supra and WEST is shown in figure 1.7. The divertor coils (symmetrical red rectangles) are installed in WEST to form the divertor configuration. There are also some passive plates in WEST, e.g. the casings of the divertor coils (yellow area), and the magnetic configuration will be changed by the induced currents on these passive plates, especially when the plasma current is increased (decreased) sharply in the ramp up (down) phase.

1.3   Tokamak operation
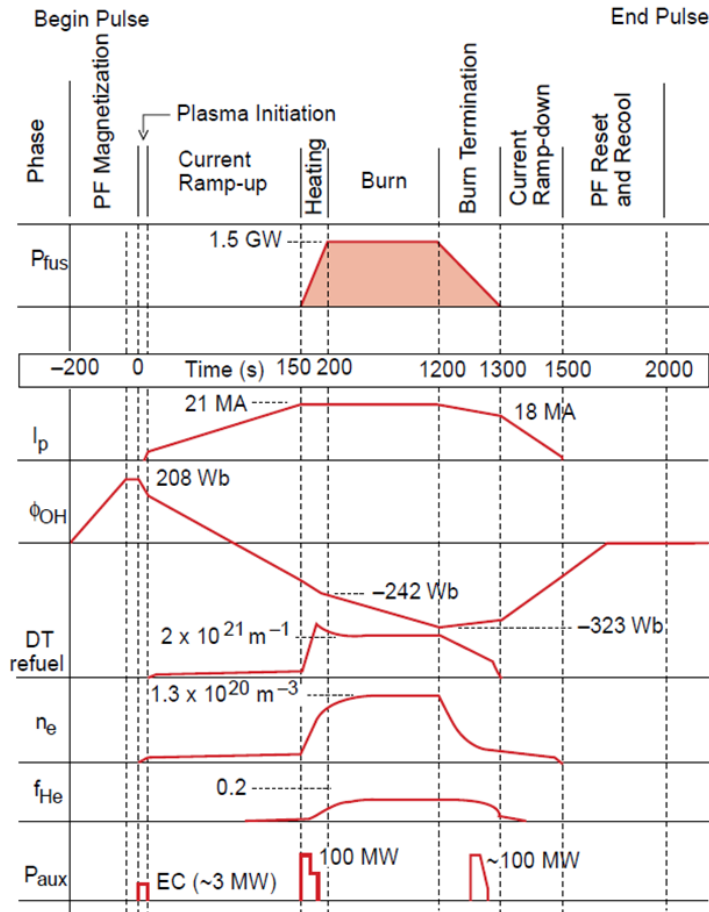
Figure 1.8: Plasma operation waveforms for ITER 1.5 GW inductively sustained ignition -

Tokamak operation is a complicated task. In order to reach a certain objective in a given tokamak, e.g., $Q_{fusion} = 10$ in ITER, one needs to design a so-called "scenario",

i.e. a trajectory in time of the plasma parameters. This scenario has to be feasible, in the sense that the plasma and the tokamak systems have to remain within a certain operational domain.

1.3.1 The schedule of plasma scenario

The plasma scenario in a tokamak aims at achieving the possible goals with the available actuators, such as the CS and PF coils, various external powers, the fueling and pumping systems. Figure 1.8 shows the schedule of ITER 21 MA plasma operation for 1.5 GW power output, which is released from the ≪ ITER Physics Basis 1999, chapter 8 ≫ [36]. It should be noted that the updated ITER targets are 15 MA plasma current and 500 MW fusion power [32].

The whole plasma scenario is divided into several phases mainly based on the plasma current (I_P):

- Pre-magnetization ($-200s \rightarrow 0$), $I_P = 0$: the CS and PF coils currents are well configured to provide enough Ohmic flux (Φ_{OH}) and poloidal magnetic field-null configuration (poloidal magnetic field B_p less than 2 mT), meanwhile, an appropriate working gas (D) pressure is prepared.

- Plasma initiation ($0 \rightarrow 1s$), $0 \leqslant I_P \leqslant 0.1MA$: the Φ_{OH} begins to swing down to produce a loop voltage, which breakdowns the working gas and accelerates the charged electrons and ions to generate toroidal I_P. For ITER 3 MW electron cyclotron (EC) wave is used to assist the plasma initiation.

- Current ramp-up ($1s \rightarrow 150s$), $0.1MA \leqslant I_P \leqslant 21MA$: the Φ_{OH} continues to swing down to provide the energy to increase the I_P to its target value of 21 MA.

- Flat-top ($150s \rightarrow 1200s$), $I_P = 21MA$: the main phase in tokamak pulse, where enough $P_{auxiliary}$ and fuels are injected into plasma to make the fusion reaction occur. The $P_{fusion} \sim 1.5$ GW is produced in this duration.

- Burn termination ($1200s \rightarrow 1300s$), $21MA \geqslant I_P \geqslant 18MA$: the burning plasma begins to terminate with the decreasing of the $P_{auxiliary}$ and I_P.

- Current ramp-down ($1300s \rightarrow 1500s$), $18MA \geqslant I_P \geqslant 0$: I_P continues to go down until 0.

- PF reset ($1500s \rightarrow 2000s$), $I_P = 0$: the CS and PF currents come back to 0 and the pulse is finished.

The evolution of the reference plasma boundaries for different phases is shown in figure 1.9. It can be seen that the plasma is initialized at the outer part with a circular shape, then it is elongated vertically and transits to a diverted shape (with an X-point at the bottom) with the increased I_P until its target 21 MA.
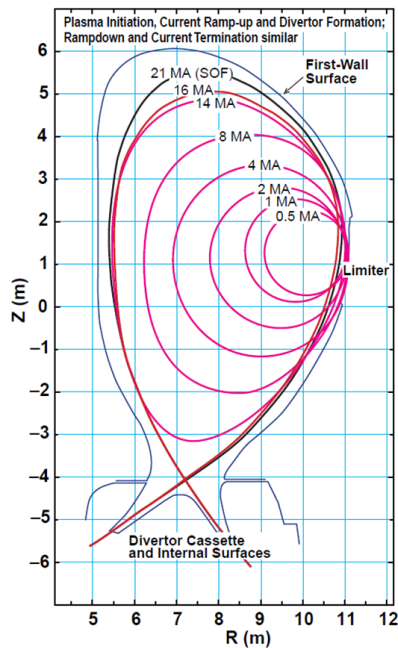
Figure 1.9: The evolution of the reference plasma shapes. - It is evolved from limiter to lower X-point divertor configurations with the increased I_P.

1.3.2 Notion of operating space

The operating space in a tokamak is typically constituted of two parts, i.e. the limits of various instabilities in plasma (e.g. MagnetoHydroDynamic (MHD) [37]) and the accessible engineering limits of the external actuators.

The electron density (n_e) limit is one of the basic instabilities in tokamak plasma operation. Figure 1.10 gives the operating space on the I_P and n_e for a tokamak by Hugill [38].
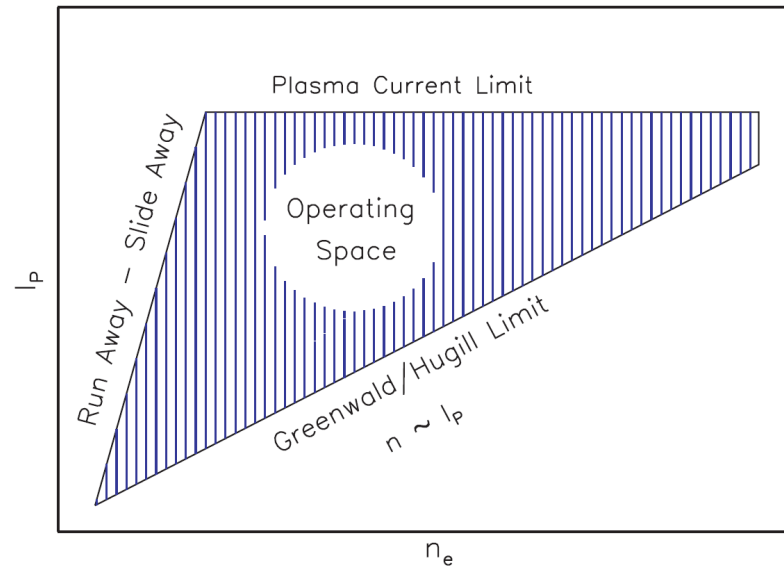
Figure 1.10: The operating space on the plasma current and density limits for a tokamak. -

It shows that the plasma operation in a tokamak is bounded by a low-density region where the electrons can be accelerated as the run-away particles, and in a high-density area where the maximum n_e limit is proportional to I_P and a (minor radius). Moreover, there is also a limit on the maximum I_P that is due to the MHD kink instabilities [39]. The plasma operation will typically terminate outside the operating space of figure 1.10 by disruptions.

The engineering limits in a tokamak operation include, e.g., the maximum CS and PF coils currents/voltages, field (for the super-conducting coils) and forces. The plasma operation will also go to termination, or even the machine may be damaged if these engineering limits are violated.

1.4   Plasma control

In order to perform the plasma scenario introduced in Section 1.3.1, a dedicated control system has to be designed. Plasma control is a key area in tokamak research, but with highly complicated workflow. The complexity of the control system, is related to the large number of parameters to be controlled and to the strong and often non-linear

coupling exists between them.

The typical strategy is to use a combination of the feedforward (FF) and feedback (FB) schemes. In linear systems, FB is enough to maintain the target. Since tokamak is a non-linear system and the control targets in different plasma scenario phases are varied, i.e. the plasma currents, shapes and so on. FF is therefore used to help the FB controller to make the control items closed to the reference values.

The problems in plasma control can be separated into two classes: magnetic control and kinetic control.

1.4.1 Magnetic control

The objects of the plasma magnetic control [40] include typically the plasma current, plasma position and the selected gaps between plasma boundary and the first wall. In the magnetic control system, the actuators are the CS and PF systems. The main work in this thesis concerns the magnetic control.
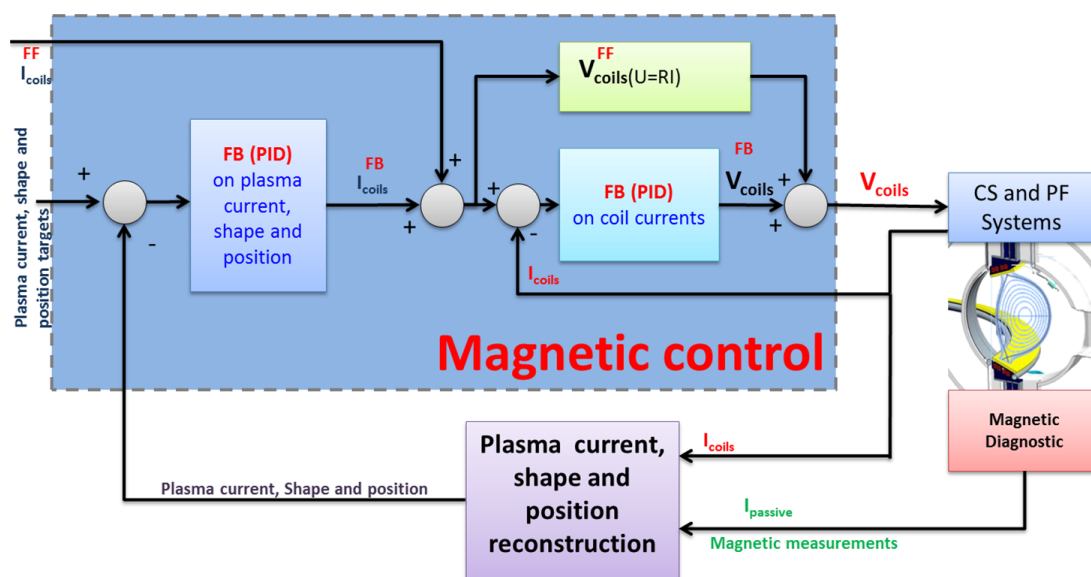
Figure 1.11: The block diagram of the WEST magnetic control loop for the plasma current, shape and position -

Figure 1.11 presents the principle of the WEST magnetic control loop, where the

control targets are the plasma current, shape and position. The FF waveforms of the CS and PF coils currents are calculated by some numerical models [41, 42], while the FF waveforms of the CS and PF coils voltages are based on the coils currents and resistances.

There are two FB control loops, i.e. one for the plasma parameters (plasma current, shape and position) and the other for the coils currents. In the plasma parameters FB loop, the output coils currents are based on the deviations between the input targets and the reconstructed ones from the magnetic measurements. While in the second FB scheme for coils currents, the output coils voltages are derived from the differences between the actual coils currents and sum of I_{coils}^{FF} and I_{coils}^{FB}, which are the output of the first FB loop. Proportional, integral as well as derivative (PID) [43] controllers are applied in both FB loops.

The CS and PF coils voltages, which are the sums of the FF and FB waveforms, are the real signals sent to the actuators to perform the magnetic control in WEST tokamak plasma operation.

Magnetic control is a mature scheme in tokamak operations, thanks to the robustness of the accurate magnetic measurements and reliable actuators.

1.4.2 Kinetic control

The objects of the kinetic control in tokamaks [44] may include, the density and temperature profiles, the plasma profile parameters, fusion power, impurity content, plasma pressure, the radiated power fraction, etc. The control actuators are the auxiliary heating and current driving systems, the fueling system and the pumping system.

The control strategy for kinetic control is also the combination of FF and FB loops. The FF waveforms are based on the solutions of the flux diffusion and energy balance equations, while the FB results are also obtained according the PID controller. The applications of these kinetic control algorithms can be found in [45, 46, 47, 48, 49].

The kinetic control is interconnected to the magnetic control, because plasma profiles and the magnetic equilibrium mutually influence each other. In this thesis, we will ignore this aspect and assume that the plasma profiles are given.

1.5   Thesis scope and organization

The main topic in this manuscript is the construction of scenarios in tokamaks, with specific focus on the CS and PF systems. The tool used to address this topic is a free-boundary equilibrium code FEEQS.M, which is developed by Holger Heumann at INRIA. It is introduced in **Chapter 2**.

The first step to design new scenarios for a new tokamak, is exploring the operating space and this work has been done in the present work with the inverse static mode (see **Chapter 2**, Section 2.2) of FEEQS.M. It is applied in the ITER case, which is given in **Chapter 3**.

Scenario construction itself can be done, with the inverse evolution mode (see **Chapter 2**, Section 2.3) of FEEQS.M. This work is also done for the fast transition from limiter to divertor on WEST, and the FF trajectory of CS and PF coils currents has been validated by a virtual tokamak control workflow and the WEST real experiment, details are presented in **Chapter 4**.

At last in **Chapter 5**, we give conclusions of the whole thesis and perspective for the future work.

Chapter 2

Free-boundary equilibrium problems and the FEEQS.M code

Plasma equilibrium is one of the basic problems in tokamak engineering and physical research, it is widely applied in the areas of plasma control, scenario construction and MHD stability analysis.

In this chapter, the basic free-boundary equilibrium (FBE) equations are firstly introduced in section 2.1. Then, the two kinds of FBE problems, i.e. *direct* and *inverse* (both of which can be either *static* or *evolutive*), are formulated in section 2.2 and section 2.3, respectively. The ideas and methods of the numerical code FEEQS.M are detailed in section 2.4. Section 2.5 contains verification results regarding the calculation of the derivatives in FEEQS.M. Section 2.6 presents first tests of the *inverse evolution* mode in the WEST and HL-2M tokamaks. A short summary of this chapter is given in section 3.8.

2.1 Free-boundary plasma equilibrium

The essential equations for describing plasma equilibrium in a tokamak are force balance, the solenoidal condition and Ampères law, that read respectively

$$\nabla p = \mathbf{J} \times \mathbf{B} \,, \quad \nabla \cdot \mathbf{B} = 0 \,, \quad \nabla \times \frac{1}{\mu} \mathbf{B} = \mathbf{J} \,, \tag{2.1}$$

where p is the plasma kinetic pressure, $\mathbf{B}$ is the magnetic field, $\mathbf{J}$ is the current density and μ the magnetic permeability. In the quasi-static approximation these equations

2. FREE-BOUNDARY EQUILIBRIUM PROBLEMS AND THE FEEQS.M CODE

are augmented by Faraday's law in all other conducting structures, and by Ohm's law in coils and passive structures. Hence for the resistive timescale the plasma is in equilibrium and (2.1) holds at each instant of time [50].

Under the assumption of perfect axial symmetry, it is convenient to put (2.1) in a cylindrical coordinate system (r, φ, z) and to consider only a meridian section of the tokamak. The primal unknown is the *poloidal magnetic flux* $\psi := r\mathbf{A} \cdot \mathbf{e}_\varphi$, the scaled toroidal component of the vector potential $\mathbf{A}$, i.e. $\mathbf{B} = \nabla \times \mathbf{A}$ and $\mathbf{e}_\varphi$ the unit vector for φ. We introduce $\mathbb{H} = [0, \infty] \times [-\infty, \infty]$, the positive half plane, to denote the meridian plane that contains the cross section of the tokamak device. The geometry of the tokamak determines the various subdomains (see figure 2.1):
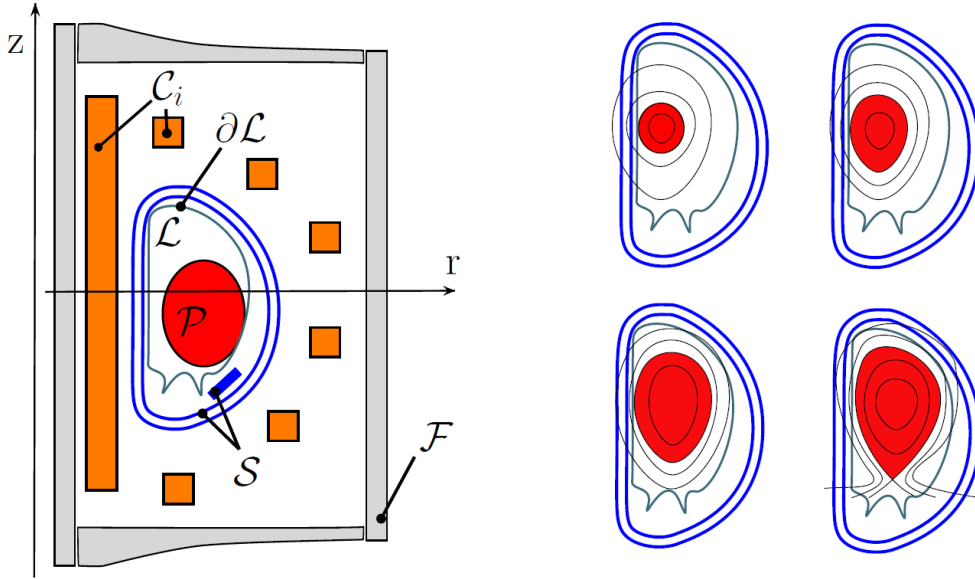
Figure 2.1: Left: Geometric description of the poloidal cross section of the tokamak device. Right: Sketch for characteristic plasma shapes during the so-called ramp-up phase. - The ψ-isolines are indicated by black lines. In the beginning (first three pictures) the plasma touches the limiter and becomes more and more elongated (limiter configuration) while finally, it moves into the divertor configuration, where the plasma boundary contains an X-point of the poloidal flux.

- the domain $\mathcal{F} \subset \mathbb{H}$ corresponds to those parts that are made of ferromagnetic circuit, i.e. the iron core and return limbs typically;

- the domain $\mathcal{C}_i \subset \mathbb{H}, 1 \leq i \leq M$ correspond to the M poloidal field coils, where each coil $\mathcal{C}_i$ has n_i wire turns, total resistance R_i and cross section $|\mathcal{C}_i|$. The coils are part of an electric circuit that contains also N voltage suppliers;

- the domain $\mathcal{S} \subset \mathbb{H}$ corresponds to the passive structures, with conductivity σ;

- the domain $\mathcal{L} \subset \mathbb{H}$, bounded by the limiter $(\partial \mathcal{L})$, corresponds to the domain that is accessible by the plasma.

Then (see [51] or [52]), the plasma equilibrium equations in a tokamak at each instant t can be written:

$$L\psi(r, z, t) = j(r, \psi(r, z, t), t) \quad \text{in} \quad \mathbb{H};$$
$$\psi(0, z, t) = 0;$$
$$\lim_{\|(r,z)\| \to +\infty} \psi(r, z, t) = 0;$$
$$\psi(r, z, 0) = \psi^0(r, z),$$

(2.2)

where L is a non-linear second-order elliptic differential operator

$$L\psi := -\frac{\partial}{\partial r}\left(\frac{1}{\mu(\psi)r}\frac{\partial \psi}{\partial r}\right) - \frac{\partial}{\partial z}\left(\frac{1}{\mu(\psi)r}\frac{\partial \psi}{\partial z}\right) := -\nabla \cdot \left(\frac{1}{\mu(\psi)r}\nabla\psi\right), \qquad (2.3)$$

with

$$\mu[\psi](r, z) = \mu_{\mathrm{f}}(|\nabla\psi(r, z)|^2 r^{-2}) \begin{cases} \geq \mu_0 & \text{in } \mathcal{F} \\ = \mu_0 & \text{elsewhere.} \end{cases} \qquad (2.4)$$

Here, ∇ is the 2D gradient in the (r, z)-plane.

The toroidal current density j is a non-linear function of ψ:

$$j\big(r, \psi(r, z, t), t\big) = \begin{cases} rp'\big(\psi(r, z, t)\big) + \frac{1}{\mu_0 r}ff'\big(\psi(r, z, t)\big) & \text{in } \mathcal{P}[\psi(t)]; \\ \frac{I_i}{|\mathcal{C}_i|} & \text{in } \mathcal{C}_i, \ 1 \leqslant i \leqslant M; \\ j_{\mathcal{S}} & \text{in } \mathcal{S}; \\ 0 & \text{elsewhere}, \end{cases} \qquad (2.5)$$

where the plasma section $\mathcal{P}[\psi(t)]$ is the domain bounded by the last closed poloidal magnetic flux line inside $\mathcal{L}$ and containing the magnetic axis $(r_{\mathrm{ax}}, z_{\mathrm{ax}})$. The magnetic axis is the point $(r_{\mathrm{ax}}, z_{\mathrm{ax}}) = (r_{\mathrm{ax}}[\psi], z_{\mathrm{ax}}[\psi])$, where ψ has its global maximum in $\mathcal{L}$. The equation in the plasma domain is the well-known **Grad − Shafranov** (G-S) equation [53, 54, 55]. The current density $j_{\mathcal{P}(\psi)} := rp'(\psi) + \frac{1}{\mu_0 r}ff'(\psi)$ in the plasma domain is non-linear in ψ due to the non-linear functions p' and ff', and due to the definition

of the plasma domain $\mathcal{P}(\psi)$. Here, $p = p(\psi)$ is the pressure and $f = f(\psi)$ is the *diamagnetic function*, i.e $f(\psi) = r\mathbf{B} \cdot \mathbf{e}_\varphi$.

For convenience, we introduce also the coordinates $(r_{\mathrm{bd}}, z_{\mathrm{bd}}) = (r_{\mathrm{bd}}[\psi], z_{\mathrm{bd}}[\psi])$ of the point that determines the plasma boundary. $(r_{\mathrm{bd}}, z_{\mathrm{bd}})$ is either a hyperbolic point of ψ (in the case of a divertor configuration) or the contact point with the limiter $\partial\mathcal{L}$ (in the case of a limiter configuration). The different characteristic shapes of $\mathcal{P}(\psi)$ are illustrated in figure 2.1 (right): the boundary of $\mathcal{P}(\psi)$ either touches the boundary of $\mathcal{L}$, the limiter, or the boundary contains one or more corners (X-points of ψ).

The total coil current I_i, relates to the voltages $\vec{V}(t) = [V_1(t), V_2(t), \dots, V_N(t)]$ in the suppliers and to self and mutual induction via electric circuit equations:

$$\frac{I_i}{|\mathcal{C}_i|} = \sum_{j=1}^{N} \mathbf{R}_{ij} V_j(t) + \sum_{k=1}^{M} \mathbf{S}_{ik} \int_{\mathcal{C}_k} \frac{\partial \psi(t)}{\partial t} \, dr \, dz \,, \quad 1 \le i \le M \,, \tag{2.6}$$

In the case of *simple electrical circuits*, e.g. circuits where each coil is connected to only one voltage supplier, we have

$$\mathbf{R}_{ij} = \begin{cases} 0 & i \ne j \\ \frac{n_i}{R_i |\mathcal{C}_i|} & i = j \end{cases} \quad \text{and} \quad \mathbf{S}_{ij} = \begin{cases} 0 & i \ne j \\ -\frac{2\pi n_i^2}{R_i |\mathcal{C}_i|^2} & i = j \end{cases}$$

and we refer to **Appendix A** for the general case.

Faraday's law in the passive structure $\mathcal{S}$ yields

$$j_{\mathcal{S}} = -\frac{\sigma}{r} \frac{\partial \psi(t)}{\partial t} \tag{2.7}$$

2.1.1 Plasma current profile

The plasma current density $j_{\mathcal{P}}$ in equation (2.5) is non-linear in ψ due to the non-linear functions p' and ff' and the definition of the plasma domain $\mathcal{P}(\psi)$. While $\mathcal{P}(\psi)$ is fully determined for a given ψ, the two functions p' and ff' are not determined by the model (2.2)-(2.5). The model (2.2)-(2.5) needs to be augmented by the so-called transport and diffusion equations [56], which determine p' and ff'. In this thesis, we will assume that, up to some scaling coefficient λ, the functions p' and ff' are known. But, the domain of p' and ff' is the interval $[\psi_{\mathrm{bd}}, \psi_{\mathrm{ax}}]$ with the scalar values ψ_{ax} and ψ_{bd} being the flux values at the magnetic axis and at the boundary of the plasma:

$$\psi_{\mathrm{ax}}[\psi] := \psi(r_{\mathrm{ax}}[\psi], z_{\mathrm{ax}}[\psi]) \,, \qquad \psi_{\mathrm{bd}}[\psi] := \psi(r_{\mathrm{bd}}[\psi], z_{\mathrm{bd}}[\psi]) \,. \tag{2.8}$$

So, since the domain of p' and ff' depends on the poloidal magnetic flux itself, it is more practical to supply those profiles as functions of the normalized poloidal flux $\overline{\psi}(r, z)$:

$$\overline{\psi}(r, z) := \frac{\psi(r, z) - \psi_{\text{ax}}[\psi]}{\psi_{\text{bd}}[\psi] - \psi_{\text{ax}}[\psi]}. \tag{2.9}$$

these two functions, subsequently termed $S_{p'}$ and $S_{ff'}$, have, independently of ψ, a fixed domain $[0, 1]$. In this thesis, we will use the following parameterization for $S_{p'}$ and $S_{ff'}$:

$$S_{p'}\big(\overline{\psi}(r, z)\big) = \frac{\beta}{R_0}\big(1 - \overline{\psi}(r, z)^\alpha\big)^\gamma$$
$$S_{ff'}\big(\overline{\psi}(r, z)\big) = (1 - \beta)\mu_0 R_0\big(1 - \overline{\psi}(r, z)^\alpha\big)^\gamma \tag{2.10}$$

where R_0 is the major radius of the vacuum vessel and α, β, γ are given parameters. The detail of the physical interpretation of these parameters can be found in [57].

The parameter β is related to the poloidal beta β_p:

$$\beta_p = \frac{\overline{p}}{B_{pa}^2/2\mu_0};$$
$$\overline{p} = \frac{\int_{\mathcal{P}} pr\, ds}{\int_{\mathcal{P}} r\, ds} \tag{2.11}$$
$$B_{pa} = \frac{\int_{\Gamma_p} B_p dl}{\int_{\Gamma_p} dl} = \frac{\mu_0 I_P}{L_p}$$

where B_p is the poloidal magnetic field, Γ_p is the plasma boundary and L_p is its perimeter.

The parameters α and γ describe the peakedness of the plasma current profile, which is related to the plasma internal inductance $l_i(3)$:

$$l_i(3) = \frac{2\int_{\mathcal{P}} B_p^2 dV}{(\mu_0 I_P)^2 R_0} \tag{2.12}$$

The above parameterization of $S_{p'}$ and $S_{ff'}$ is convenient for many applications, but it does not necessarily represent realistic profiles, especially for H-mode plasmas, where a pedestal exists in the boundary, such as the works presented in the EPED codes [58, 59]. It is also possible in FEEQS.M to use arbitrary profiles.

The total plasma current $I_p(t)$ is given as:

$$\lambda(t) \int_{\mathcal{P}(\psi)} \left(rS_{p'}\big(\overline{\psi}(r, z, t), t\big) + \frac{1}{\mu_0 r} S_{ff'}\big(\overline{\psi}(r, z, t), t\big) \right) dr dz = I_p(t). \tag{2.13}$$

2.2 The direct FBE problems

In this section, we present the so-called "direct" FBE problems, which consist in finding the ψ map for given PF coils currents or PF power supply voltages. We distinguish the *direct static* problem, which concerns a snapshot at a given time, and the *direct evolution* problem, which concerns the dynamic evolution of the plasma equilibrium. These problems are formulated as follows.

Problem 1 (Direct static) *Let parameters α, β and γ in the definition (2.10) of $S_{p'}(\overline{\psi}(r,z))$ and $S_{ff'}(\overline{\psi}(r,z))$ be known, and let the currents I_i in the coils $\mathcal{C}_i$ as well as the total plasma current I_P and current density j_S in the passive structures be given. Find ψ and λ such that (2.2), (2.5) and (2.13) hold, with $p'(\psi(r,z)) = \lambda S_{p'}(\overline{\psi}(r,z))$ and $ff'(\psi(r,z)) = \lambda S_{ff'}(\overline{\psi}(r,z))$ at time t fixed.*

The *direct static* FBE problem consists in finding the plasma equilibrium for given coils currents at a given instant. An example of application of this problem is the calculation of an initial condition for the *direct evolution* problem.

Problem 2 (Direct evolution) *Let the evolution of parameters $\alpha(t), \beta(t)$ and $\gamma(t)$ in the definition (2.10) of $S_{p'}(\overline{\psi}(r,z,t),t)$ and $S_{ff'}(\overline{\psi}(r,z,t),t)$ be known. Let the evolution of the voltages $\vec{V}(t)$ in the poloidal field circuits and the initial data $\psi_0(r,z)$ be given. Additionally assume that the evolution of $I_P(t)$ is given. Find the evolution of $\psi(t)$ and $\lambda(t)$ such that (2.2), (2.5)-(2.7) and (2.13) hold, with $p'(\psi(r,z,t),t) = \lambda(t)S_{p'}(\overline{\psi}(r,z,t),t)$ and $ff'(\psi(r,z,t),t) = \lambda(t)S_{ff'}(\overline{\psi}(r,z,t),t)$.*

The *direct evolution* FBE problem combines the plasma equilibrium equations with equations describing the evolution of PF coils currents as well as currents in the passive structures. It is applied, e.g., in the WEST magnetic control simulator presented in **Chapter 4**.

2.3 The inverse FBE problems

In the last section, we have discussed the *direct static* and *evolution* FBE problems, where the coils currents $\vec{I} = (I_1, I_2, \cdots, I_M)$ or poloidal circuits voltages $\vec{V}(t)$ are given. In this section, we introduce the *inverse* FBE problems, which consist in finding the currents $\vec{I}$ or voltages $\vec{V}(t)$ to satisfy a desired plasma scenario. Solving these problems

is challenging due, among other reasons, to their ill-posedness, their non-linear nature and, especially in the case of the *inverse evolution* problem, their large size.

Typically, the way to deal with such *inverse* FBE problems, is an optimal control approach. The currents $\vec{I}$ or voltages $\vec{V}(t)$ are the *control variables*, and the ψ or $\psi(t)$ map describing the equilibria is the *state variable*. We encode the design goal in an objective function, which is large when the design goal is violated and small otherwise.

The *direct static* and *evolution* FBE problems are formulated as follows.

Problem 3 (Inverse static) *Let parameters α, β and γ in the definition (2.10) of $S_{p'}(\overline{\psi}(r,z))$ and $S_{ff'}(\overline{\psi}(r,z))$ be known, and assume additionally that the total plasma current I_P and current density j_S in the passive structures are given. Moreover, let objective$(\psi(r,z), \vec{I})$ be a non-negative function that is small if $\psi(r,z)$ is close to the design goal. Solve the following minimization problem:*

$$\min_{\psi(r,z),\vec{I}} objective\big(\psi(r,z), \vec{I}\big) \quad \text{subject to (2.2), (2.5) and (2.13)} \quad \text{at time t fixed} \quad (2.14)$$

with $p'(\psi(r,z)) = \lambda S_{p'}(\overline{\psi}(r,z))$ and $ff'(\psi(r,z)) = \lambda S_{ff'}(\overline{\psi}(r,z))$.

In general, the objective function $(\psi(r,z), \vec{I})$ is divided into two parts, i.e. *cost function* (denoted by C) and *regularization term* (denoted by R):

$$\text{objective}\big(\psi(r,z), \vec{I}\big) = C\big(\psi(r,z)\big) + R(\vec{I}) \tag{2.15}$$

Examples of *cost function* and *regularization term* for the *inverse static* FBE problem are:

$$C\big(\psi(r,z)\big) = \frac{1}{2} \sum_{i=2}^{N_{\text{desi}}} \big(\psi(r_i, z_i) - \psi(r_1, z_1)\big)^2, \tag{2.16}$$

and

$$R(\vec{I}) = \frac{1}{2} \sum_{i=1}^{M} w_i \, I_i^2, \tag{2.17}$$

where (r_i, z_i) describes the desired plasma boundary and coefficients $w_i \geq 0$ are called regularization weights. $C(\psi(r,z))$ "'incites" $\psi(r,z)$ to be constant on a prescribed set of N_{desi} points (r_i, z_i). The *regularization term* $R(\vec{I})$ enables to work with a well-posed problem, i.e. a problem that is stable to perturbations on the data.

The *static inverse* solver is used to find the PF coils currents $\vec{I}$, which allow the best match with a given plasma shape at a given time.

2. FREE-BOUNDARY EQUILIBRIUM PROBLEMS AND THE FEEQS.M CODE

In **Chapter 3**, we use the *static inverse* solver to identify the plasma equilibrium operating space for the ITER inductive scenario, but with more complex objective functions, involving *penalization terms* to take into account limits on the coils currents, field and forces.

Problem 4 (Inverse evolution) . *Let the evolution of parameters $\alpha(t), \beta(t)$ and $\gamma(t)$ in the definition of (2.10) of $S_{p'}(\overline{\psi}(r, z, t), t)$ and $S_{ff'}(\overline{\psi}(r, z, t), t)$ be known. Additionally assume that the evolution of the total plasma current $I_P(t)$ and initial data $\psi_0(r,z)$ are given. Moreover, let objective$(\psi(r, z, t), \vec{V}(t))$ be a non-negative function that is small if $\psi(r, z, t)$ is close to the design goal. Solve the following minimization problem:*

$$\min_{\psi(r,z,t),\vec{V}(t)} objective\big(\psi(r, z, t), \vec{V}(t)\big) \quad subject \ to \quad (2.2), \ (2.5) - (2.7) \ and \ (2.13)$$

(2.18)

with $p'(\psi(r, z, t), t) = \lambda(t)S_{p'}(\overline{\psi}(r, z, t), t)$ and $ff'(\psi(r, z, t), t) = \lambda(t)S_{ff'}(\overline{\psi}(r, z, t), t)$.

As for the *inverse static* case, the objective function here is also split into $C(\psi(r, z, t))$ + $R(\vec{V}(t))$.

Examples for $C(\psi(r, z, t))$ and $R(\vec{V}(t))$ are:

$$C\big(\psi(r, z, t)\big) = \frac{1}{2}\int_0^T w(t)\sum_{i=2}^{N_{\text{desi}}} \Big(\psi\big(r_i(t), z_i(t), t\big) - \psi\big(r_1(t), z_1(t), t\big)\Big)^2 dt \qquad (2.19)$$

and

$$R\big(\vec{V}(t)\big) = \frac{1}{2}\int_0^T \sum_{i=1}^N \mathbf{D}_i \, V_i^2(t) \, dt \,, \qquad (2.20)$$

where the $\big(r_i(t), z_i(t)\big)$ describe the prescribed plasma boundaries at discrete times in the interval [0,T]. The weights $w(t)$ should be non-negative and $\mathbf{D}$ positive definite. $C(\psi(r, z, t))$ tends to make $\psi(r, z, t)$ constant on a prescribed set of N_{desi} points $(r_i(t), z_i(t))$ at each instant t and hence can be used to encode a certain desired evolution of the plasma shape. Other choices of *cost function* could include penalization of induced currents, voltages in suppliers or loop voltages or any other design goal that can be quantified in terms of the poloidal flux ψ and the voltages $V_i(t)$. Tests involving different *cost functions* for scenario design are presented in section 2.6.

In **Chapter 4**, we use the *inverse evolution* FBE solver to develop a fast limiter to divertor transition in WEST.

2.4 The FEEQS.M code and its numerical methods

We introduce in this thesis the numerical code FEEQS.M (Finite Element EQuilibrium Solver based on Matlab) [60], which utilizes finite elements formulation and inherits the basic ideas of the FBE codes SCED [61] and CEDRES++ [62], to solve the *direct/inverse static/evolution* FBE problems. FEEQS.M uses well established and tested external modules for mesh generation [63], linear solvers (such as UMFPACK [64]) and algebraic solver [65]. The finite element method in FEEQS.M allows for a straightforward implementation of Newton methods to handle the strong non-linearities related to the FBE problems. FEEQS.M is based on methods for axisymmetric free boundary plasma equilibria that are described in [51] and utilizes in large parts vectorizations. Therefore, the running time is comparable to C/C++ implementations. Moreover, FEEQS.M is also publicly available[1] now.

The general idea to solve the *direct* and *inverse* FBE problems in FEEQS.M is to find variational formulations of the partial differential equations (PDEs) (2.2), (2.5)-(2.7). Then, standard linear Lagrangian finite elements are used to discretize the variational formulations and the objective functions. A sequential quadratic programming (SQP) approach is used to solve the optimal control problems, i.e., *inverse* FBE problems in FEEQS.M.

There are two different approaches to arrive at the finite dimensional SQP formulations for the optimal control problems 3 and 4, which have been stated in section 2.3. In the first one, the *optimize-then-discretize* approach, one computes first the optimality conditions for the continuous optimization problem, and then discretizes them. The second approach, the *discretize-then-optimize* approach, discretizes directly the optimization problems. This yields a finite dimensional constrained optimization problem for which a SQP formulation follows immediately from the literature [66, 67].

In FEEQS.M, we prefer to work with the *discretize-then-optimize* approach for the following reason: *discretize-then-optimize* yields the exact gradient of the discrete objective function, while the *optimize-then-discretize* approach yields only an approximation. Both approaches involve approximation, but the *optimize-then-discretize* approach does not yield the exact gradient of either the continuous objective in (2.15), (2.19) and (2.20), or the discretized objective [68]. Therefore, the validation of the

---

[1]`http://www-sop.inria.fr/members/Holger.Heumann/Software.html`

implementation of a *discretize-then-optimize* approach is relatively easy compared to an *optimize-then-discretize* approach.

It remains to specify the discretization of non-linear constraints (2.2), (2.5) and (2.6), as well as the discretization of the objective functionals. Moreover, as we use SQP, we will also have to provide some details on first and second order derivatives of the discretized objective functionals and constraints. The implementation itself is kept flexible, so that objective functionals can be easily changed and modified. Adding new cost functionals encoding new design goals is simple.

The following subsections will introduce the detailed ideas and methods applied in FEEQS.M, including the variational formulations for the *static* and *evolution* FBE problems (section 2.4.1), the discretization formulations for the FBE problems (section 2.4.2 and 2.4.3) and the SQP approaches for the *inverse static* and *inverse evolution* FBE problems (section 2.4.4).

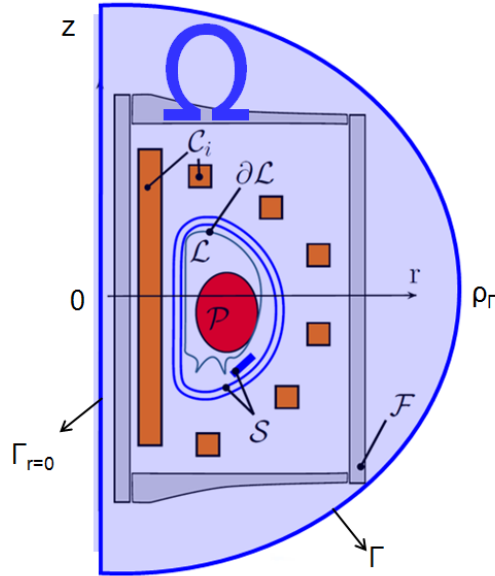### 2.4.1 Variational formulation on the truncated domain

Figure 2.2: The bounded domain in FEEQS.M -

In FEEQS.M, a semi-circle area $\Omega \subset \mathbb{H}$ in figure 2.2 with a sufficiently large radius ρ_Γ, that is centered at the origin and contains the geometry of the tokamak, is selected.

The boundary $\partial\Omega$ splits into $\Gamma_{r=0} := \{(r,z)\,,\, r=0\}$ and $\Gamma = \partial\Omega \setminus \Gamma_{r=0}$. The Sobolev space [69] V is used:

$$V := \left\{ \psi : \Omega \to \mathbb{R}, \int_\Omega \psi^2 r\, drdz < \infty, \int_\Omega (\nabla\psi)^2 r^{-1}\, drdz < \infty, \psi_{|\Gamma_{r=0}} = 0 \right\} \cap C^0(\Omega). \tag{2.21}$$

In the domain of Ω, the equation (2.2) can be written after multiplying the test function $\xi \in V$ and doing the integration over the whole area as :

$$\int_\Omega L\psi\, \xi\, drdz = \int_\Omega j(r,\psi,t)\, \xi\, drdz \tag{2.22}$$

The weak variational formulation of the equation (2.22) can be given after doing integration by parts as:

$$\int_\Omega \frac{1}{\mu(\psi)r}\nabla\psi \cdot \nabla\xi\, drdz + \int_{\partial\Omega} \frac{1}{\mu(\psi)r}(\nabla\psi \cdot \mathbf{n})\, \xi dl = \int_\Omega j(r,\psi,t)\, \xi\, drdz \tag{2.23}$$

where $\mathbf{n}$ is the inward pointing normal.

The second term in the LHS of the equation (2.23) can be divided into two parts on Γ and $\Gamma_{r=0}$:

$$\int_{\partial\Omega} \frac{1}{\mu(\psi)r}\frac{\partial\psi}{\partial n}\, \xi dl = \int_\Gamma \frac{1}{\mu_0 r}\frac{\partial\psi}{\partial n}\, \xi dl + \int_{\Gamma_{r=0}} \frac{1}{\mu_0 r}\frac{\partial\psi}{\partial n}\, \xi dl \tag{2.24}$$

where the second term of RHS is 0, so the weak variational formulation of equation (2.23) on the bounded domain Ω is:

$$\int_\Omega \frac{1}{\mu(\psi)r}\nabla\psi \cdot \nabla\xi\, drdz + \int_\Gamma \frac{1}{\mu_0 r}\frac{\partial\psi}{\partial n}\, \xi dl = \int_\Omega j(r,\psi,t)\, \xi\, drdz \tag{2.25}$$

2.4.2 Galerkin discretizations and their weak variational formulations

In FEEQS.M, we introduce a triangulation Ω_h of the domain Ω that resolves the subdomains $\mathcal{L}, \mathcal{F}, \mathcal{C}_i, \mathcal{S}$ and use standard Lagrangian finite elements with nodal degrees of freedom.

Let $b_k(r,z)$ denote the Lagrangian basis functions associated to the vertices of the mesh, e.g., b_k vanishes at all mesh vertices except one. Basis functions associated to vertices at $r=0$ are excluded from this finite element space X_h, as, due to axisymmetry $\psi(0,z) = 0$.

For the *static* case at a fixed time, the finite element approximation ψ_h of ψ is:

$$\psi_h(r,z) = \sum_{k=1}^{|X_h|} \psi_k b_k(r,z) \text{ with } \psi_k \in \mathbb{R},\, 1 \le k \le |X_h|. \tag{2.26}$$

2. FREE-BOUNDARY EQUILIBRIUM PROBLEMS AND THE FEEQS.M CODE

For the discretization in time we introduce $N_T + 1$ not necessarily equidistant collocation points $T_0 \leq t_s \leq T_1$, $0 \leq s \leq N_T$. Hence, for the *evolution* case, the finite element approximation ψ_h^t of ψ at $t = t_s$ is:

$$\psi_h^s(r, z) = \sum_{k=1}^{|X_h|} \psi_{ks} b_k(r, z) \text{ with } \psi_{ks} \in \mathbb{R}, \ 1 \leq k \leq |X_h|, \ 0 \leq s \leq N_T. \tag{2.27}$$

The *domain of the plasma* $\mathcal{P}(\psi_h)$ of a finite element function ψ_h is bounded by a continuous, piecewise straight, closed line. The critical points $(r_{\text{ax}}(\psi_h), z_{\text{ax}}(\psi_h))$ and $(r_{\text{bd}}(\psi_h), z_{\text{bd}}(\psi_h))$ are the coordinates of certain vertices of the mesh. The saddle point of a piecewise linear function ψ_h is some vertex (r_0, z_0) with the following property: if $(r_1, z_1), (r_2, z_2) \dots (r_N, z_N)$, denote the counterclockwise ordered neighboring vertices the sequence of discrete gradients $\psi_0 - \psi_1, \ \psi_0 - \psi_2 \dots \psi_0 - \psi_N$ changes at least four times the sign.

Therefore, we can get the following discretized version (modulo quadrature) of equation (2.25) in the *static* mode: For given coils currents $\vec{I} = (I_1, I_2, \cdots, I_M)$ and I_P, and for given current density j_S in the passive structures S, we find the coefficients $\psi_k \in \mathbb{R}, 1 \leq k \leq |X_h|$ of ψ_h, and $\lambda \in \mathbb{R}$ such that:

$$\int_\Omega \frac{1}{\mu(\psi_h)r} \nabla \psi_h \cdot \nabla \xi \, drdz - \lambda \int_{\mathcal{P}(\psi_h)} \left(r S_{p'}(\overline{\psi}_h) + \frac{S_{ff'}(\overline{\psi}_h)}{\mu_0 r} \right) \xi \, drdz \quad + \mathsf{c}(\psi_h, \xi)$$

$$- \sum_{i=1}^M \frac{I_i}{|\mathcal{C}_i|} \int_{\mathcal{C}_i} \xi drdz - j_S \int_S \xi drdz = 0 \quad \forall \xi \in X_h,$$

$$\lambda \int_{\mathcal{P}(\psi_h)} \left(r S_{p'}(\overline{\psi}_h) + \frac{1}{\mu_0 r} S_{ff'}(\overline{\psi}_h) \right) drdz = I_P \,.$$

$$\tag{2.28}$$

The bilinear form $\mathsf{c} : V \times V$ on Γ, accounting for the boundary conditions at infinity [70], is the second term of LHS in equation (2.25):

$$\begin{aligned} \mathsf{c}(\psi, \xi) :=& \frac{1}{\mu_0} \int_\Gamma \psi(\mathbf{P}_1) N(\mathbf{P}_1) \xi(\mathbf{P}_1) dS_1 \\ &+ \frac{1}{2\mu_0} \int_\Gamma \int_\Gamma (\psi(\mathbf{P}_1) - \psi(\mathbf{P}_2)) M(\mathbf{P}_1, \mathbf{P}_2)(\xi(\mathbf{P}_1) - \xi(\mathbf{P}_2)) dS_1 dS_2. \end{aligned} \tag{2.29}$$

with $\mathbf{G}(\mathbf{P}_1, \mathbf{P}_2) \approx \log(\| \mathbf{P}_1 - \mathbf{P}_2 \|)$, which is the fundamental solution of $\nabla \cdot \frac{1}{\mu_0 r} \nabla$ and

$$M(\mathbf{P}_1, \mathbf{P}_2) = \frac{k_{\mathbf{P}_1,\mathbf{P}_2}}{2\pi(r_1 r_2)^{\frac{3}{2}}} \left(\frac{2 - k_{\mathbf{P}_1,\mathbf{P}_2}^2}{2 - 2k_{\mathbf{P}_1,\mathbf{P}_2}^2} E(k_{\mathbf{P}_1,\mathbf{P}_2}) - K(k_{\mathbf{P}_1,\mathbf{P}_2}) \right)$$

$$N(\mathbf{P}_1) = \frac{1}{r_1} \left(\frac{1}{\delta_+} + \frac{1}{\delta_-} - \frac{1}{\rho_\Gamma} \right) \text{ and } \delta_\pm = \sqrt{r_1^2 + (\rho_\Gamma \pm z_1)^2} \,,$$

where $\mathbf{P}_i = (r_i, z_i)$. K and E are the complete elliptic integrals of first and second kind, respectively and

$$k_{\mathbf{P}_j,\mathbf{P}_k} = \sqrt{\frac{4 r_j r_k}{(r_j + r_k)^2 + (z_j - z_k)^2}} \,.$$

The details of the above derivation are shown in [71, Chapter 2.4]. Alternative approaches, that incorporate the boundary conditions at infinity are recently presented in [72]. The bilinear form $\mathbf{c}(\cdot, \cdot)$ follows basically from the so-called *uncoupling procedure* in [73] for the usual coupling of boundary integral and finite element methods. In FEEQS.M, it can be shown that for all $\mathbf{P}_1$, $\mathbf{P}_2$ the integral term $(\psi(\mathbf{P}_1) - \psi(\mathbf{P}_2)) M(\mathbf{P}_1, \mathbf{P}_2)(\xi(\mathbf{P}_1) - \xi(\mathbf{P}_2))$ remains bounded. The Green's function that is used in the derivation of the boundary integral method for the above problem, was used earlier in finite difference methods for the Grad-Shafranov-Schlüter equations [74].

The same way, we get the following discretized version of equation (2.25) in the *evolution* mode: For given evolution $\vec{V}(t) = (V_1(t), V_1(t), \cdots, V_N(t))$ and $I_P(t)$ of the voltages and the total plasma current and for given initial conditions $\psi_h^0(r, z) = \sum_{k=1}^{|X_h|} \psi_{k0} b_k(r, z)$ we find for $1 \le s \le N_T$ the coefficients $\psi_{ks} \in \mathbb{R}, 1 \le k \le |X_h|$ of ψ_h^s, the values $I_{is} \in \mathbb{R}, 1 \le i \le M$ and $\lambda^s \in \mathbb{R}$ such that:

$$\int_\Omega \frac{1}{\mu(\psi_h^s) r} \nabla \psi_h^s \cdot \nabla \xi \, dr dz - \lambda^s \int_{\mathcal{P}(\psi_h^s)} \left(r S_{p'}(\overline{\psi}_h^s, t_s) + \frac{S_{ff'}(\overline{\psi}_h^s, t_s)}{\mu_0 r} \right) \xi \, dr dz$$

$$- \sum_{i=1}^M \frac{I_{is}}{|\mathcal{C}_i|} \int_{\mathcal{C}_i} \xi dr dz + \int_S \frac{\sigma}{r} \frac{\psi_h^s - \psi_h^{s-1}}{t_s - t_{s-1}} \xi \, dr dz + \mathbf{c}(\psi_h^s, \xi) = 0 \quad \forall \xi \in X_h \,,$$

$$\sum_{j=1}^N \mathbf{R}_{ij} V_j(t_s) + \sum_{k=1}^M \mathbf{S}_{ik} \int_{\mathcal{C}_k} \frac{\psi_h^s - \psi_h^{s-1}}{t_s - t_{s-1}} \, dr dz = \frac{I_{is}}{|\mathcal{C}_i|} \quad 1 \le i \le M \,,$$
(2.30)

$$\lambda^s \int_{\mathcal{P}(\psi_h^s)} \left(r S_{p'}(\overline{\psi}_h^s, t_s) + \frac{1}{\mu_0 r} S_{ff'}(\overline{\psi}_h^s, t_s) \right) dr dz = I_P^s \,.$$

2.4.3   Quadrature rules and discretization of the objective functions

The integration over the domain Ω is split into a sum of integrals over the triangles T of the mesh, and we use the barycenter quadrature rule to approximate these integrals: For a triangle with vertex coordinates $\mathbf{a}_i, \mathbf{a}_j, \mathbf{a}_k \in \mathbb{R}^2$ the quadrature point is the barycenter $\mathbf{b}_T := \frac{1}{3}(\mathbf{a}_i + \mathbf{a}_j + \mathbf{a}_k)$ and the quadrature weight ω_T is the size $|T|$ of the triangle.

Besides the integrals over Ω, the weak formulations (2.28) and (2.30) involve also integrals over the plasma domain $\mathcal{P}(\psi_h)$. As the mesh does not resolve the boundary of the plasma domain $\mathcal{P}(\psi_h)$, we need to specify also the quadrature rule that is used to approximate integrals over intersections $T \cap \mathcal{P}(\psi_h)$ of triangles with the plasma domain. We use again barycenter quadrature, but here the quadrature point and weight will depend non-linearly on ψ_h, which needs to be taken into account when we use linearizations of (2.28) and (2.30), e.g. in Newton or SQP iterations. The technical details of such linearizations can be also found in [68].

The line integrals over Γ in the definition of $\mathsf{c}(\cdot, \cdot)$ are split into line integrals over edges on triangles whose vertices are on Γ. Then, the trapezoidal quadrature rule yields an approximation of sufficient accuracy.

For the discretization of the objective functions in the *inverse* FBE problems. The same barycentric quadrature rule is used to approximate area integrals, while time integrals are approximated by the composite trapezoidal rule.

The discretization of the regularization functionals likewise uses the composite trapezoidal rule for time integrals. Moreover, we represent each voltage as a finite series

$$V_i(t) = \sum_{j=1}^{N_c} V_{ij} B_j(t), \quad 1 \leq i \leq n \,,$$

where the $B_j(t)$ are the basis functions of a polynomial or spline space over $[0, T]$.

This yields expressions that are algebraic in the principal unknowns (ψ_k and I_i for the static case, and ψ_{ks} and V_{ij} for the evolution case, with $1 \leq k \leq |X_h|$, $1 \leq i \leq m$, $1 \leq s \leq N_T$ and $1 \leq j \leq N_c$). So, computation and implementation of first and second order derivatives of such functionals become a mechanical iterated application of the usual rules of differential calculus.

2.4.4 SQP formulation for the inverse FBE solvers

Combining the discretized *inverse* FBE equations with discretized cost and regularization functionals, we arrive at discretized versions of the optimal control formulation (2.30) that is of the general form

$$\min_{\mathbf{u},\mathbf{y}} J(\mathbf{y},\mathbf{u}) \quad \text{s.t.} \quad \mathbf{b}(\mathbf{y},\mathbf{u}) = 0\,. \tag{2.31}$$

The state variable $\mathbf{y}$, in the case of the *evolution* problem, contains the unknowns ψ_{ks} $1 \leq k \leq |X_h|$, $1 \leq s \leq N_T$ of the poloidal flux and the scaling parameter λ^s, $1 \leq s \leq N_T$, hence $\mathbf{y} \in \mathbb{R}^{(|X_h|+1)N_T}$. Likewise the constraint $\mathbf{b}(\mathbf{y},\mathbf{u}) = 0$ corresponds to $(|X_h|+1)N_T$ coupled non-linear equations as the unknowns for the currents I_{is}, $1 \leq i \leq m$, $1 \leq s \leq N_T$ have been eliminated from the formulation (2.30). The coupling in time appears through the electric circuit equations (2.6) and the induction (see (2.5)) in passive structure $\mathcal{S}$ that involve temple derivatives of ψ. The control variable $\mathbf{u}$ contains a subset of the expansion coefficients V_{ij}, $1 \leq i \leq n$, $1 \leq j \leq N_c$ for the voltages. One could for example prescribe the voltage of a few suppliers and treat only the voltages of the remaining suppliers as unknowns. Another possibility would be to treat only certain coefficients as unknown. E.g. if one works with an expansion in a hierarchical basis, it would be beneficial to prescribe the coefficients for low order terms and keep only coefficients of higher order polynomials. So, in general $\mathbf{u} \in \mathbb{R}^N$ with $1 \leq N \leq N_c n$.

For the *static* case, where the current density $j_{\mathcal{S}}$ in the passive structure $\mathcal{S}$ is given, the state variable $\mathbf{y}$ includes ψ_k $1 \leq k \leq |X_h|$ and λ, the control variable $\mathbf{u}$ is the coils currents $\vec{I}$. Similar to the *evolution* case, one could prescribe the current of a few coils, and treat the currents remaining as the unknowns.

The SQP formulation for the constrained optimization problem (2.31) involves first and second order derivatives of $\mathbf{b}(\mathbf{y},\mathbf{u})$ and $J(\mathbf{y},\mathbf{u})$. But, as we presented in sections 2.4.2 and 2.4.3 explicit expressions for $\mathbf{b}(\mathbf{y},\mathbf{u})$ and $J(\mathbf{y},\mathbf{u})$ that are algebraic in $\mathbf{u}$ and $\mathbf{y}$, we can also provide explicit expressions for the first and second order derivatives. An inspection of (2.30) shows that the constraint $\mathbf{b}(\mathbf{y},\mathbf{u})$ is affine in the control unknown $\mathbf{u}$, hence has vanishing second order derivatives. Moreover, to avoid the expensive assembling of second order derivatives of $\mathbf{b}(\mathbf{y},\mathbf{u})$ we neglect those in the SQP iterations. In the terminology of Newton methods we use rather a *quasi* SQP method, than an

exact SQP method. It is known that such modifications are prone to convergence issues [75], but this doesn't seem to be an issue for our specific application. The Algorithm 1 summarizes the quasi SQP formulation, and should be compared to the exact SQP in Algorithm 4 (see Appendix B), where it is also required to compute the adjoint states during the iterations. The first and second order derivatives are indicated by subscripts, e.g. $J_\mathbf{u}$ for the first order of derivative of J. We want to stress that the size of $\mathbf{Y}$ in Algorithm 4 scales at least linearly (and quadratically if $N_c = O(N_T)$) with the number of time steps N_T, which causes memory to be the limiting factor for computations with a very large number of time steps. Nevertheless, with the current implementation we can go easily beyond 200 and more time steps, which is sufficient for the applications in mind. Moreover, we avoid the introduction of additional parameters due to iterative solver and make use of fast methods for linear systems with multiple RHS.

Algorithm 1 SQP (quasi) with direct solver

1: $\Delta\mathbf{u} \leftarrow 1, \Delta\mathbf{y} \leftarrow 1, \mathbf{y} \leftarrow \mathbf{y}^0, \mathbf{u} \leftarrow \mathbf{u}^0$

2: **while** $\|\Delta\mathbf{u}\|/\|\mathbf{u}\| > tol$, $\|\Delta\mathbf{y}\|/\|\mathbf{y}\| > tol$ **do**

3:     $(\Delta\mathbf{y}, \mathbf{Y}) \leftarrow -\mathbf{b}_\mathbf{y}^{-1}(\mathbf{y}, \mathbf{u})(\mathbf{b}(\mathbf{y}, \mathbf{u}), \mathbf{b}_\mathbf{u}(\mathbf{y}, \mathbf{u}))$

4:     $\mathbf{m}_{01} \leftarrow J_\mathbf{u}^T(\mathbf{y}, \mathbf{u}), \mathbf{m}_{10} \leftarrow \mathbf{Y}^T J_\mathbf{y}^T(\mathbf{y}, \mathbf{u})$

5:     $\mathbf{M}_{02} \leftarrow J_{\mathbf{uu}}(\mathbf{y}, \mathbf{u})$

6:     $\mathbf{m}_{11} \leftarrow J_{\mathbf{uy}}(\mathbf{y}, \mathbf{u})\Delta\mathbf{y}, \mathbf{M}_{11} \leftarrow J_{\mathbf{uy}}(\mathbf{y}, \mathbf{u})\mathbf{Y}$

7:     $\mathbf{m}_{20} \leftarrow \mathbf{Y}^T J_{\mathbf{yy}}(\mathbf{y}, \mathbf{u})\Delta\mathbf{y}, \mathbf{M}_{20} \leftarrow \mathbf{Y}^T J_{\mathbf{yy}}(\mathbf{y}, \mathbf{u})\mathbf{Y}$

8:     $\mathbf{m} \leftarrow \mathbf{m}_{01} + \mathbf{m}_{10} + \mathbf{m}_{11} + \mathbf{m}_{20}$

9:     $\mathbf{M} \leftarrow \mathbf{M}_{02} + \mathbf{M}_{11} + \mathbf{M}_{11}^T + \mathbf{M}_{20}$

10:     $\Delta\mathbf{u} \leftarrow -\mathbf{M}^{-1}\mathbf{m}$

11:     $\mathbf{y} \leftarrow \mathbf{y} + \Delta\mathbf{y} + \mathbf{Y}\Delta\mathbf{u}$

12:     $\mathbf{u} \leftarrow \mathbf{u} + \Delta\mathbf{u}$

13: **end while**

2.5   Numerical validation tests

We present different numerical tests, that verify that the implementations of derivatives of the non-linear constraints (2.28) and (2.30) in FEEQS.M are correct. These derivatives are the cornerstone of the proposed optimal control approach and appear

through $\mathbf{b_y}(\mathbf{y}, \mathbf{u})$ in SQP (see Algorithm 1).

The following calculations are based on a ITER-like geometry and an equlibrium plasma (see figure 2.3) that corresponds to the currents in the table of figure 2.3. The total plasma current is $I_P = 15MA$, and parameters for the plasma current density in equation (2.10) are: $R_0 = 6.2m$, $\alpha = 2.0$, $\beta = 0.5978$ and $\gamma = 1.395$.
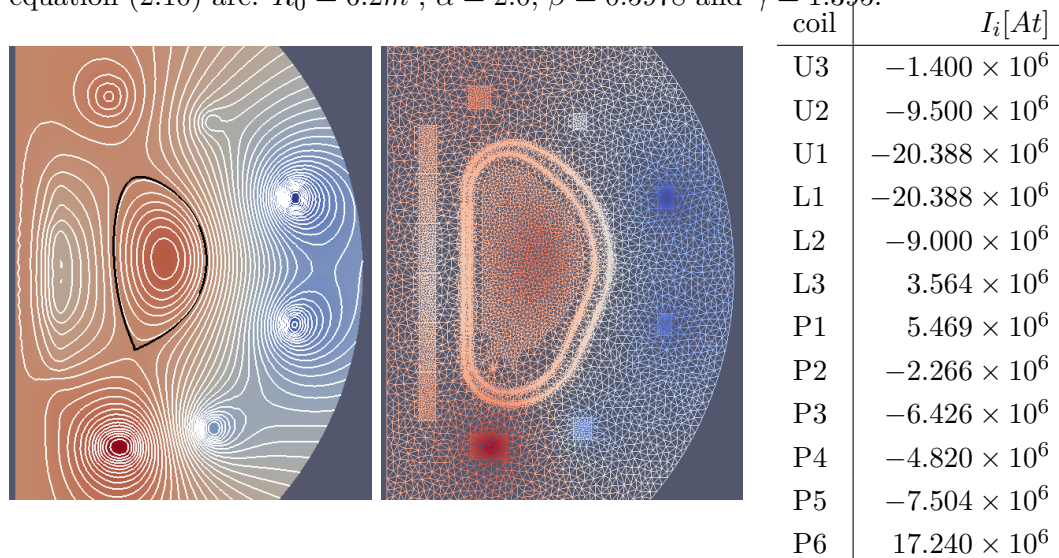

coil	$I_i[At]$
U3	-1.400×10^6
U2	-9.500×10^6
U1	-20.388×10^6
L1	-20.388×10^6
L2	-9.000×10^6
L3	3.564×10^6
P1	5.469×10^6
P2	-2.266×10^6
P3	-6.426×10^6
P4	-4.820×10^6
P5	-7.504×10^6
P6	17.240×10^6

Figure 2.3: Left: The plasma (flux lines and flux intensity) that correspond to the currents in the table. Center: The triangulation of the ITER-geometry. Right: Data for coils. U1-U3 and L1-L3 are upper and lower CS coils. Coils P1-P6 are the PF coils.

2.5.1 Derivatives due to the free-boundary

Let $D\mathsf{J}_h(\psi_h) \in \mathbb{R}^{|X_h| \times |X_h|}$ denote the derivative of the discretization $\mathsf{J}_h(\psi_h, b_m)$ (via quadrature from section 2.4.3) of the non-linear mapping

$$\mathsf{J}(\psi_h, b_m) = \int_{\mathcal{P}(\psi_h)} \left(rS_{p'}(\overline{\psi}_h) + \frac{1}{r\mu_0} S_{ff'}(\overline{\psi}_h, t_s) \right) b_m \, dr dz \quad 1 \leq m \leq |X_h|. \quad (2.32)$$

This mapping involves the non-linearity due to the free plasma boundary. The linearization is non-standard [68]. In this first test it is verified that for given $\psi_h(r, z) = \sum_{k=1}^{|X_h|} \psi_k b_k(r, z)$ and perturbation $\delta_h(r, z) = \sum_{k=1}^{|X_h|} \delta_k b_k(r, z)$ the implementation of $D\mathsf{J}_h(\psi_h)$ yields:

$$E_{\mathrm{FD}}(\varepsilon) := \frac{\left\| \varepsilon^{-1} \left(\mathsf{J}_h(\psi_h + \varepsilon\delta_h, \cdot) - \mathsf{J}_h(\psi_h, \cdot) \right) - D\mathsf{J}_h(\psi_h) \cdot \delta \right\|}{\| D\mathsf{J}_h(\psi_h) \cdot \delta \|} = O(\varepsilon). \quad (2.33)$$

2. FREE-BOUNDARY EQUILIBRIUM PROBLEMS AND THE FEEQS.M CODE

The perturbation increment δ is randomly chosen. In table 2.1 we monitor this relative error and observe, as expected, first order convergence.

2.5.2 Convergence of the sensitivities

Another way to validate the implementation of the derivatives appearing in $\mathbf{b_y}(\mathbf{y}, \mathbf{u})$ would consist in solving the non-linear constraint $\mathbf{b}(\mathbf{y}, \mathbf{u})$ for $\mathbf{y}$ and monitor the convergence. For an accurate implementation of the derivatives the convergence will be quadratic. On the other hand, since in many cases also with inaccurate derivatives one will observe super-linear convergence, this test could fail as indicator for accurate derivatives. The following test is more appropriate: We consider a control $\mathbf{u}_\varepsilon$ that is parametrized by $\varepsilon \in \mathbb{R}$ and suppose we know $\mathbf{y}_0$ that verifies $\mathbf{b}(\mathbf{y}_0, \mathbf{u}_0)$. Then it holds

$$\mathbf{y}_\varepsilon^1 - \mathbf{y}_\varepsilon = O(\varepsilon^2)\,, \tag{2.34}$$

where $\mathbf{y}_\varepsilon^1$ is the first Newton iteration for the problem $\mathbf{b}(\mathbf{y}_\varepsilon, \mathbf{u}_\varepsilon) = 0$ with initial guess $\mathbf{y}_0$:

$$\mathbf{b_y}(\mathbf{y}_0, \mathbf{u}_\varepsilon) \cdot (\mathbf{y}_\varepsilon^1 - \mathbf{y}_0) = -\mathbf{b}(\mathbf{y}_0, \mathbf{u}_\varepsilon) \tag{2.35}$$

The result (2.34) follows from $\mathbf{y}_\varepsilon = \mathbf{y}_0 + \mathbf{y}_0'\varepsilon + O(\varepsilon^2)$ and $0 = \mathbf{b}(\mathbf{y}_0, \mathbf{u}_\varepsilon) + \varepsilon \mathbf{b_y}(\mathbf{y}_0, \mathbf{u}_\varepsilon)\mathbf{y}_0' + O(\varepsilon^2)$. When the exact derivative $\mathbf{b_y}(\mathbf{y}_0, \mathbf{u}_\varepsilon)$ in (2.35) is replaced by some approximation $\overline{\mathbf{A}}$:

$$\overline{\mathbf{A}} \cdot (\overline{\mathbf{y}}_\varepsilon^1 - \mathbf{y}_0) = \mathbf{f}(\mathbf{u}_\varepsilon) - \mathbf{a}(\mathbf{y}_0)\,.$$

then $\overline{\mathbf{y}}_\varepsilon^1$ will be at most first order approximation of $\mathbf{y}_\varepsilon$.

The first test of this kind is for the variational formulation (2.28) of the static inverse FBE problem. The unperturbed control data $\mathbf{u}_0$ is the data given in the table in figure 2.3 and perturbation is a random incremental current for each coil scaled with $\varepsilon = 0.5^0, \ldots 0.5^{14}$. In table 2.1 (4th column) the error $E_{\mathrm{DN}}(\varepsilon) = \|\mathbf{y}_\varepsilon - \mathbf{y}_\varepsilon^1\|$ is monitored. We observe second order convergence, which shows that we use accurate derivatives. In contrast, the result $E_{\mathrm{CN}}(\varepsilon) = \|\mathbf{y}_\varepsilon - \overline{\mathbf{y}}_\varepsilon^1\|$ for a Newton-type iteration method (see 6th column in table 2.1) that follows from the discretization of derivatives of the continuous problem [51, 71] yields only first order convergence.

Repeating the same test for the implementation for weak Galerkin formulation (2.30), based on the discretization and linarization described in sections 2.4.3 and 2.4.4 we observe the expected second order convergence (see table 2.1, 8th and 9th column). This reassures that the implementation in FEEQS.M is correct.

$\varepsilon_i = \frac{1}{2}^i$	J in (2.32)		Static FBE (2.28)				Evolution FBE (2.30)	
i	$E_{\text{FD}}(\varepsilon_i)$	rate	$E_{\text{DN}}(\varepsilon_i)$	rate	$E_{\text{CN}}(\varepsilon_i)$	rate	$E_{\text{DN}}(\varepsilon_i)$	rate
0	0.0198034		11647.2		2928.07		645.401	
1	0.0113253	0.81	5485.42	1.09	1125.83	1.38	450.549	0.52
2	0.0061465	0.88	3362.31	0.70	1182.56	-0.07	31.6012	3.83
3	0.0032184	0.93	1936.28	0.80	846.373	0.50	36.9223	-0.22
4	0.0016494	0.96	694.294	1.48	149.343	2.50	10.7593	1.78
5	0.0008353	0.98	4.26942	7.35	268.207	-0.84	2.66903	2.01
6	0.0004204	0.99	9.65561	-1.18	145.894	0.88	0.66434	2.01
7	0.0002109	1.00	2.39544	2.01	70.5145	1.05	0.16571	2.00
8	0.0001056	1.00	0.60127	1.99	34.6608	1.02	0.04138	2.00
9	0.0000528	1.00	0.15064	2.00	17.1804	1.01	0.01034	2.00
10	0.0000264	1.00	0.03770	2.00	8.55259	1.01	0.00258	2.00
11	0.0000132	1.00	0.00943	2.00	4.26687	1.00	0.00064	2.00
12	0.0000066	1.00	0.00236	2.00	2.13108	1.00	0.00016	2.00
13	0.0000033	1.00	0.00059	2.00	1.06495	1.00	0.00004	2.00
14	0.0000016	1.00	0.00015	2.00	0.53233	1.00	0.00001	2.00

Table 2.1: Convergence of the errors $E_{...}$ and the convergence rate ($\frac{log(E_{...}(\varepsilon_{i+1})) - log(E_{...}(\varepsilon_i))}{log(\varepsilon_{i+1}) - log(\varepsilon_i)}$): 1.) the finite difference error E_{FD} (2.33); 2.) the error E_{DN} using the derivatives outlined in section 2.4.2 for the FBE problem (2.28); 3.) the error E_{CN} using derivatives in [51, 71] for the FBE problem (2.28); 4.) the error E_{DN} using the derivatives outlined in sections 2.4.1 and 2.4.4 for the *inverse evolution* FBE problem (2.30).

Coil	Maximum Voltage (V)	Minimum Voltage (V)
A	1400	-1400
Bh	1400	-1400
Dh	2500	-2500
Eh	2500	-2500
Fh	2500	-2500
Fb	2500	-2500
Eb	2500	-2500
Db	2500	-2500
Bb	1400	-1400
X_h	300	-300
X_b	300	-300

Table 2.2: Maximum and minimum voltages on the poloidal coils of WEST.

2.6 First applications of the inverse evolution solver

The *direct static/evolution* as well as *inverse static* modes have been operational and applied for a long time, whether in FEEQS.M or in other codes. In contrast, the *inverse evolution* mode has been implemented only recently in FEEQS.M and is a unique feature of the code, as far as we know. Therefore, it is useful to present some of the tests we did for this new mode in order to show that the code works "as it should" and to familiarize ourselves with it. This is the object of the present section, which describes applications of the *inverse evolution* mode of FEEQS.M to example problems in the WEST and HL-2M tokamaks. In **Chapter 4** we will present a more "real-life" application: the design of reference waveforms for WEST scenarios and their validation on both the WEST magnetic control simulator and on the real machine.

2.6.1 WEST scenario with different objective functions

In this section, we apply the *inverse evolution* mode of FEEQS.M to the problem of the transition from limiter to divertor configuration in the WEST tokamak [35]. We will test different cost functions and regularization terms in order to find a smooth transition while respecting the maximum and minimum voltages that can be provided by the power supplies to the coils.

Figure 2.4 shows the geometry and mesh of WEST. All the results are based on a mesh with 52210 triangles and 27763 vertices. We use $N_T = 10$ time steps with equidistant time step length of $5\,ms$, the voltage in the A coil (i.e. the central solenoid) is fixed to its minimum value of $-1400\,V$ in all the following cases to provide flux swing to drive the plasma current. The degree of the polynomial representation of the voltages is 8. The evolution of the total plasma current $I_P(t)$ and the parameters $\alpha(t)$, $\beta(t)$ and $\gamma(t)$ for the current density profiles is inspired from Tore Supra (the predecessor of WEST) experimental data and is shown in figure 2.5.
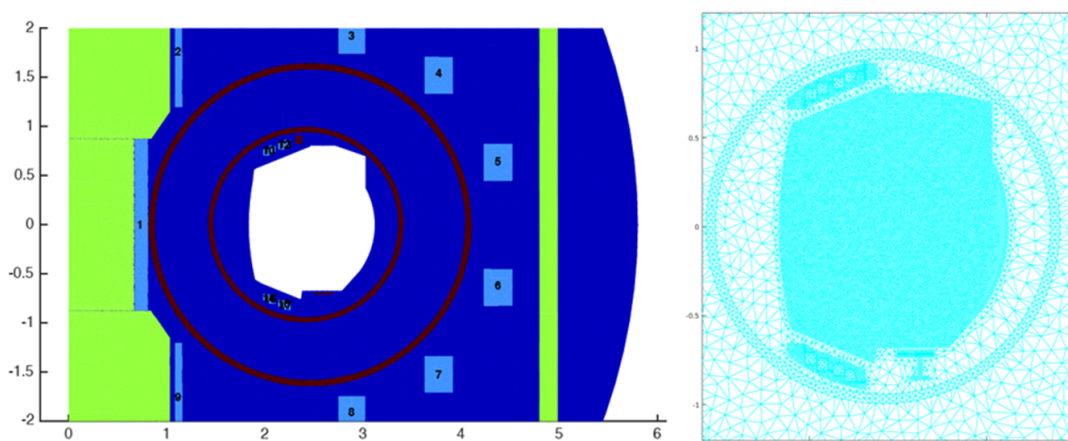
Figure 2.4: Left: cross-section of WEST showing the iron core $\mathcal{F}$ (green), the passive structure $\mathbb{S}$s (red) and the PF coils $\mathcal{C}_i$ (light blue). Right: the computation mesh. - The coils numbers 1-9 represent A, Bh, Dh, Eh, Fh, Eh, Dh, Bh, 10-13 represent Xh and 14-17 represent Xb.

2.6.1.1 Prescribed level sets at all time steps

As a first approach to the problem, we solve the discretized inverse evolution problem (2.31) with $J(\mathbf{y}, \mathbf{u}) := C(\mathbf{y}) + R_1(\mathbf{u})$, in which:

$$
\begin{aligned}
C(\mathbf{y}) &:= \frac{1}{2} \sum_{s=1}^{N_T} \sum_{i=1}^{N_{\text{desi}}} w_s \left(\psi_h^s(r_i, z_i) - \psi_h^s(r_0, z_0) \right)^2, \\
R_1(\mathbf{u}) &:= \frac{1}{2} w_{R_1} \sum_{i=1}^{N} \sum_{s=1}^{N_T} V_i(t_s)^2.
\end{aligned}
\tag{2.36}
$$
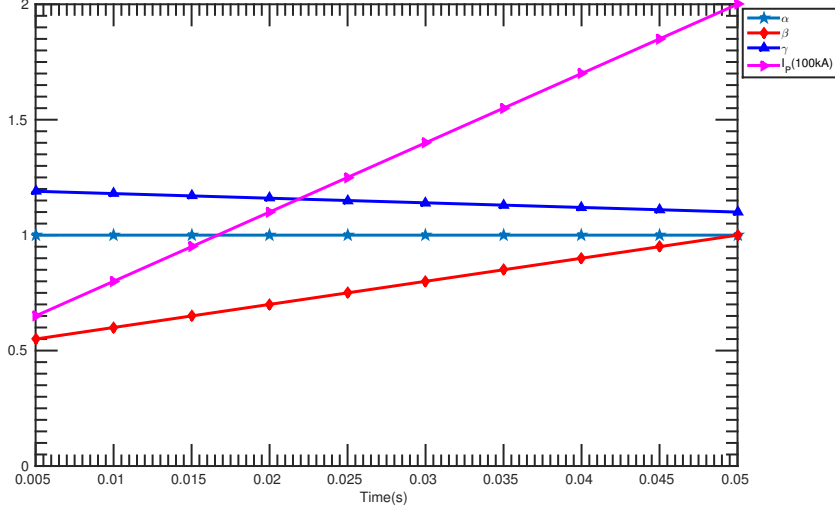
Figure 2.5: The prescribed I_P, and the plasma profile parameters α, β and γ for the WEST simulation. -

Here, $C(\mathbf{y})$ is the discretization of the cost function (2.19) introduced in Section 2.3, and aims to prescribe a desired level set for every time step, and the weights are $w_i = 1$ for $1 < i < N_T$ and $w_1 = w_{N_T} = 0.5$. The weight of the regularization term $R_1(\mathbf{u})$ is fixed to $w_{R_1} = 1 \times 10^{-11}$.

The results (see figure 2.6) show that the prescribed level sets coincide fairly well with level sets of the numerical solution at all times, with a tiny discrepancy when the plasma evolves from limiter to divertor configuration. The evolution of the voltages can be seen in figure 2.7. As we are not imposing any constraints on the voltages, it is not very surprising that the voltages limits (the dashed lines) are violated at certain time steps.

2.6.1.2 Prescribed level sets at all times and constraint penalization term

Secondly, we add two regularization terms to the objective function to penalize the violation of the voltage limits. That is to say, we solve now the constrained optimization
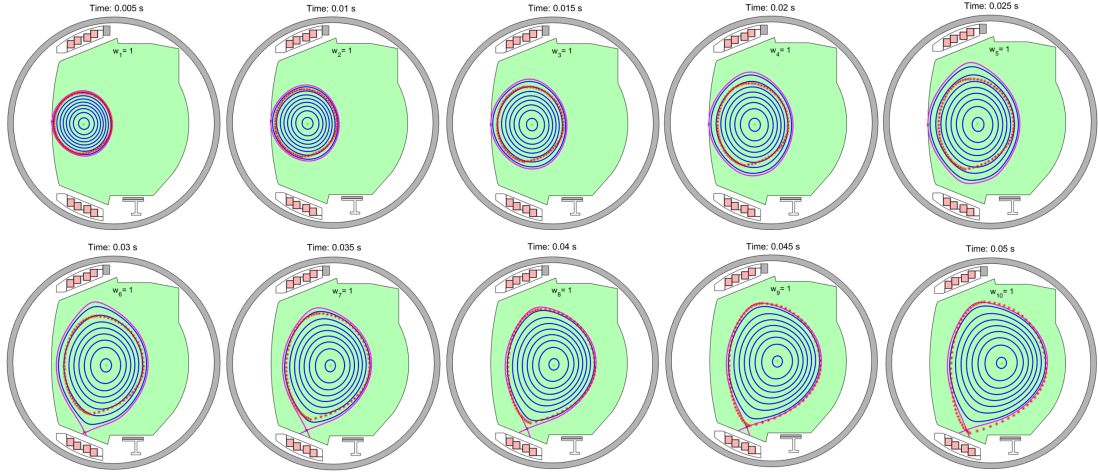
Figure 2.6: Plasma evolution obtained with prescribed level sets at all time steps (see 2.6.1.1). The magenta contour is the plasma boundary and the blue lines are ψ level sets inside the plasma, the red points indicate the desired boundary.
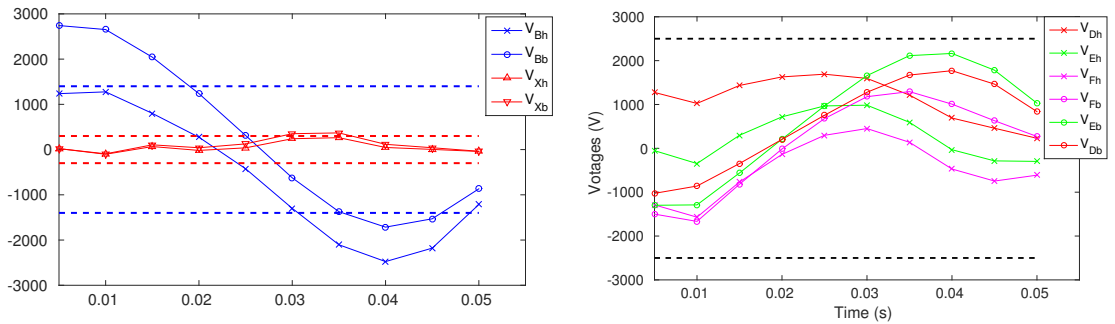

Figure 2.7: Voltages obtained with prescribed level sets at all time steps (see 2.6.1.1). Dashed lines indicate the limits of the power supplies.
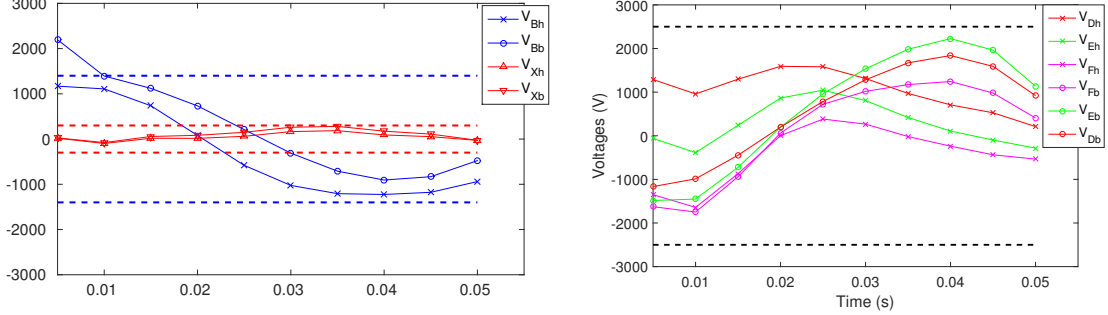
Figure 2.8: Voltages obtained with prescribed level sets at all time steps (see 2.6.1.2). Dashed lines indicate the limits of the power supplies.

problem (2.31) for $J(\mathbf{y}, \mathbf{u}) := C(\mathbf{y}) + R_1(\mathbf{u}) + R_2(\mathbf{u}) + R_3(\mathbf{u})$ with

$$
\begin{aligned}
R_2(\mathbf{u}) &:= \frac{1}{2} \sum_{i=1}^{L} w_{R_2,i} \sum_{s=1}^{N_T} max(V_i(t_s) - V_{i,max}, 0)^3\,, \\
R_3(\mathbf{u}) &:= \frac{1}{2} \sum_{i=1}^{L} w_{R_3,i} \sum_{s=1}^{N_T} max(V_{i,min} - V_i(t_s), 0)^3\,,
\end{aligned}
\tag{2.37}
$$

where the weights are $w_{R_2,i} = w_{R_3,i} = \frac{1}{2} \times 10^{-16}$.

The level sets of the flux inside and near the plasma are found to be almost the same as in the previous case (shown in figure 2.6), but the evolution of the voltages, shown in figure 2.8, is slightly different and all voltages, except for V_{Bb} at t= 0.005s, remain now within their limits. By introducing regularization terms with non-uniform weights it would probably be possible to improve this result.

2.6.1.3 Prescribed level sets at start and end

Assuming that level sets are prescribed at every time step is not very relevant in practical applications, where one aims to solve problems that require a few hundred or thousands of time steps. Providing level sets a each time step is a humongous amount of work that moreover confines the plasma evolution fairly strictly and could prevent from finding the best scenarios. A more relevant task is to find reasonable trajectories for prescribed level sets at the beginning and end only. Therefore, we use in this third case the prescribed boundaries only on some of the time steps, meaning we set in the objective function $C(\mathbf{y})$ in (2.36) the weights w_1, w_2, w_3 and w_{10} to one but the
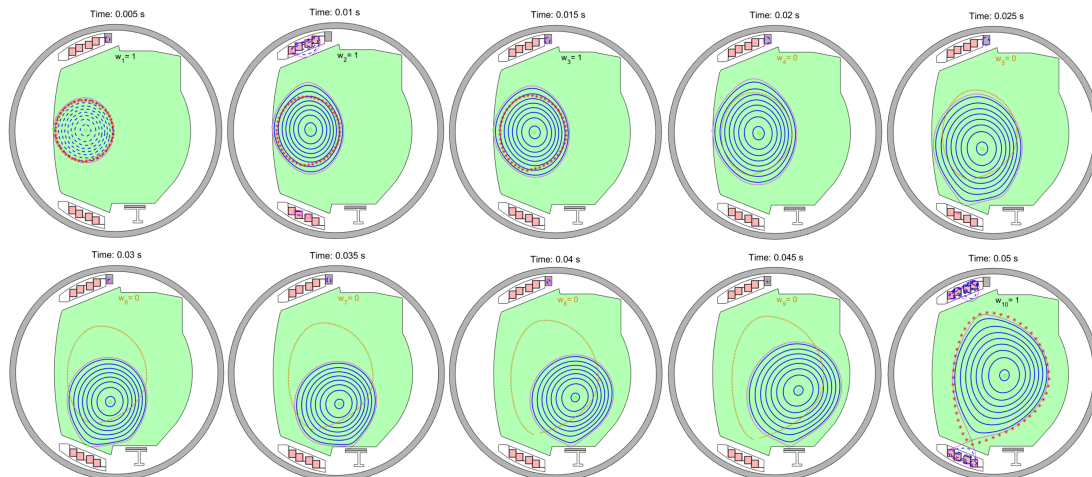
Figure 2.9: Plasma evolution obtained with prescribed level sets at start and end (see 2.6.1.3). The magenta contour is the plasma boundary and the blue lines are ψ level sets inside the plasma, the red points indicate the desired boundary.

remaining weights $w_4, w_5, ... w_9$ to zero. Introducing

$$C_0(\mathbf{y}) := \frac{1}{2} \sum_{s=\{1,2,3,10\}} \sum_{i=1}^{N_{\text{desi}}} \left(\psi_h^s(r_i, z_i) - \psi_h^s(r_0, z_0) \right)^2$$

for brevity, we solve hence here the optimization problem (2.31) with $J(\mathbf{y}, \mathbf{u}) := C_0(\mathbf{y}) + R_1(\mathbf{u}) + R_2(\mathbf{u}) + R_3(\mathbf{u})$, where the weights in the regularization terms $R_1(\mathbf{u})$, $R_2(\mathbf{u})$ and $R_3(\mathbf{u})$ are as in the previous case.

The plasma trajectory of the numerical solution is shown in figure 2.9. It can be seen that the plasma boundary matches the prescribed level sets at the beginning and at the end. However, in between, when there is no prescribed level set, the plasma makes a large downward excursion. The evolution of the voltages is shown in figure 2.10. Limits are respected, except for the divertor coils during the last two time steps. Clearly, the vertical excursion of the plasma obtained in this simulation is not desirable from an operational point of view. In order to suppress such excursions without having to prescribe level sets in intermediate time steps, a possible idea is to penalize the induced currents in the passive structures. Indeed, fast plasma motions are associated to large induced currents. Penalizing these currents should make the code priviledge smooth plasma trajectories. This strategy is tested in the next section.
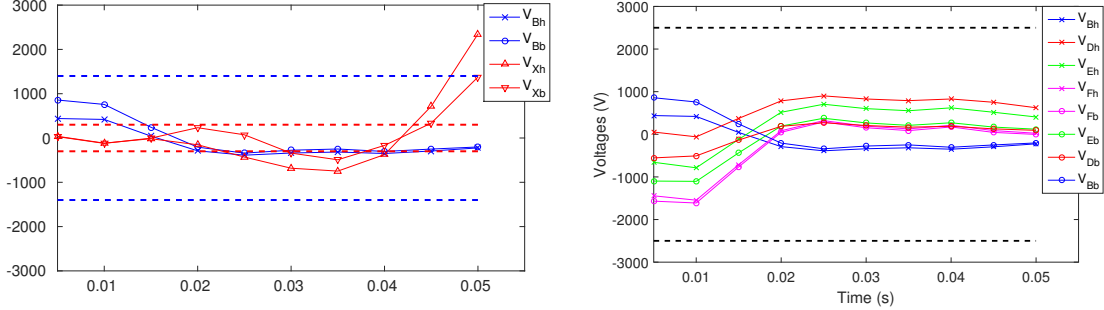
Figure 2.10: Voltages obtained with prescribed level sets at start and end (see 2.6.1.3). Dashed lines indicate the limits of the power supplies.

2.6.1.4 Prescribed level sets at start and end with penalization term on induced currents

In order to avoid the fast changes obtained in the previous simulation we add to the objective a new term that penalizes the induced currents

$$I_{ps,s} := \int_{\mathcal{S}} \frac{\sigma}{r} \frac{\psi_h^{s+1}(r,z) - \psi_h^s(r,z)}{t_{s+1} - t_s} dr\, dz \quad 1 \le s \le N_T$$

in passive structures $\mathcal{S}$ with conductivity σ. We solve the optimization problem (2.31) with $J(\mathbf{y}, \mathbf{u}) := C_0(\mathbf{y}) + C_1(\mathbf{y}) + R_1(\mathbf{u}) + R_2(\mathbf{u}) + R_3(\mathbf{u})$ and

$$C_1(\mathbf{y}) = \frac{1}{2} w_{C_1} \sum_{s=1}^{N_T} I_{ps,s}^2 \tag{2.38}$$

where $w_{C_1} = 1 \times 10^{-6}$.

The results, shown in figure 2.11, are quite satisfying: the plasma stays near the equatorial plane even during the time steps when the level set is not prescribed, and evolves in a smooth fashion to its final shape. This shows that the penalization term on induced currents allows finding slowly moving solutions even if we prescribed level sets only in the beginning and end. The evolution of the voltages is shown in figure 2.12 and we highlight that all the voltages remain within the limits.

These tests show that with well tuned cost functions and regularization terms, we can get a smooth plasma limiter to divertor transition within only 50 ms, which is a very short duration, while respecting the voltage limits. Achieving such a fast transition on the real machine may be interesting from the operational point of view in order to avoid plasma contamination by impurities. This however requires FEEQS.M
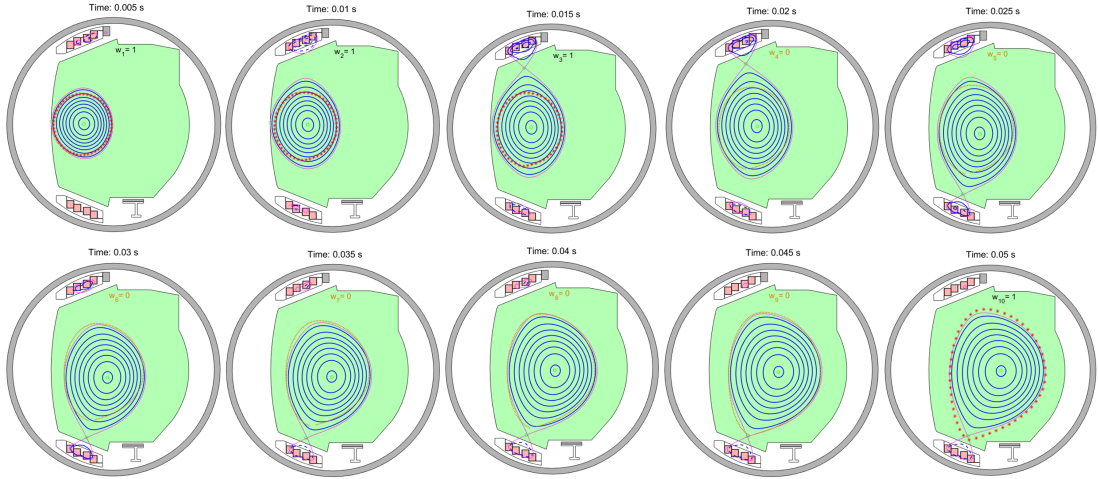
Figure 2.11: Plasma evolution obtained with prescribed level sets at start and end with penalization term on induced currents (see 2.6.1.4). The magenta contour is the plasma boundary and the blue lines are ψ level sets inside the plasma, the red snowflake points indicate the desired boundaries.
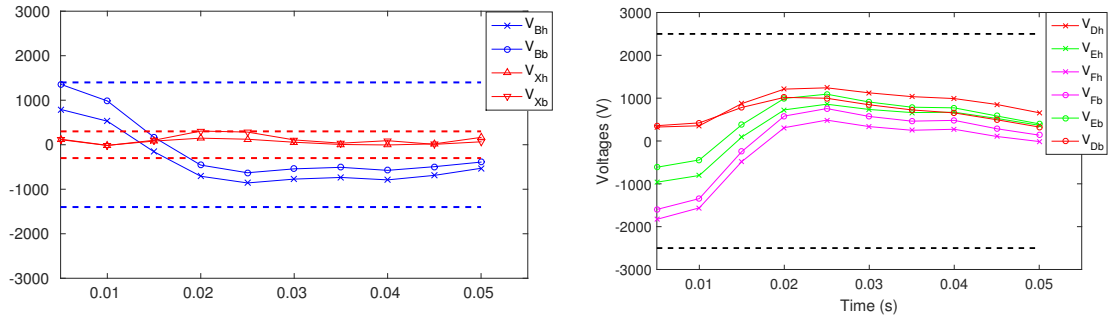

Figure 2.12: Voltages obtained with prescribed level sets at start and end with penalization term on induced currents (see 2.6.1.4). Dashed lines indicate the limits of the power supplies.

simulations which are in closer relation to the actual experiments. This will be the topic of **Chapter 4**.

2.6.2 Full scenario computation for HL-2M tokamak

In the previous section, we have focused on a short slice of a tokamak scenario. In contrast, in this section, we present an *inverse evolution* calculation of FEEQS.M for a full scenario, which includes the plasma current ramp up, flat top and ramp down phases, for the new tokamak HL-2M [76] (see figure 2.13 for the cross-section) in China. A major objective of this machine is the exploration of ITER related physical issues.
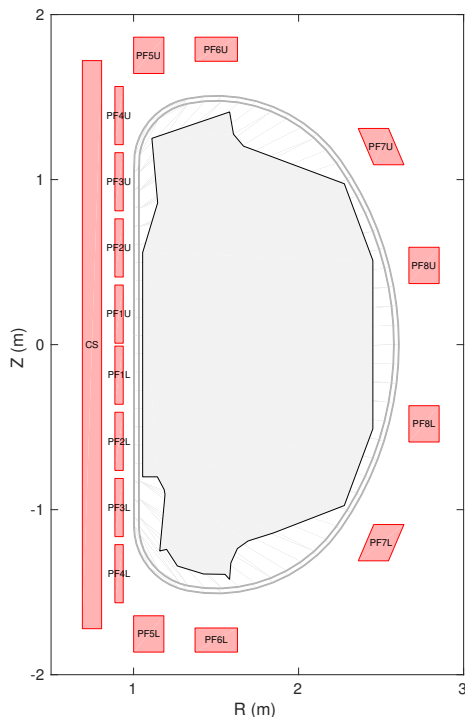

Figure 2.13: Cross-section of the HL-2M tokamak. Red quadrangles are the poloidal field coils $\mathcal{C}_i$, the grey lines are the two layers of the vacuum vessel, and the black line is the limiter $\mathcal{L}$. -

The settings for the computations are the following: the parameters I_P, α, β and γ are prescribed as shown in figure 2.14. The length of time steps in the ramp up phase (from $0.1s$ to $2s$) and ramp down phase (from $8.1s$ to $10s$) is $0.1s$, while in the flat

top phase (from $2.3s$ to $8s$) it is $0.3s$. In total we have 60 time steps. The objective function is $J(\mathbf{y}, \mathbf{u}) = C(\mathbf{y}) + R(\mathbf{u})$, with $C(\mathbf{y})$ the discretization of (2.19) and $R(\mathbf{u})$ the discretization of (2.20). Plasma boundaries are prescribed for every time step and the weights w and $\mathbf{D_{ii}}$ are 1 and 1×10^{-10}. The computational mesh is divided into 30583 triangles, and the total number of vertices is 15367. The degree of polynomials for the voltage waveforms is 8.
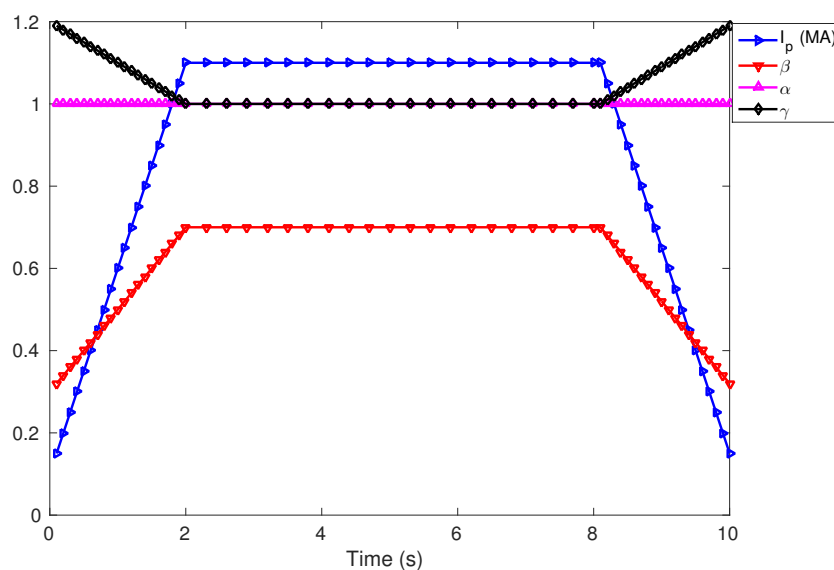

Figure 2.14: The prescribed I_P, and the parameters of the plasma profile for the full scenario simulation of HL-2M. -

Altogether we end up with a constrained optimization problem that has almost one million unknowns, of which approximately a hundred correspond to control unknowns $\mathbf{u}$. We solve this problem in 15 iterations and the computing time is less than $350\,s$ on standard notebook with a $4 \times 2.7\,GHz$ processor and $32\,GB$ memory.

In figure 2.15 we show the plasma boundary at some selected time steps. As can be seen, the plasma follows well the reference boundary in the whole time interval. The voltages are shown in figure 2.16. This example shows that the presented approach can construct a full operation scenario for tokamaks with a reasonable amount of computational power.
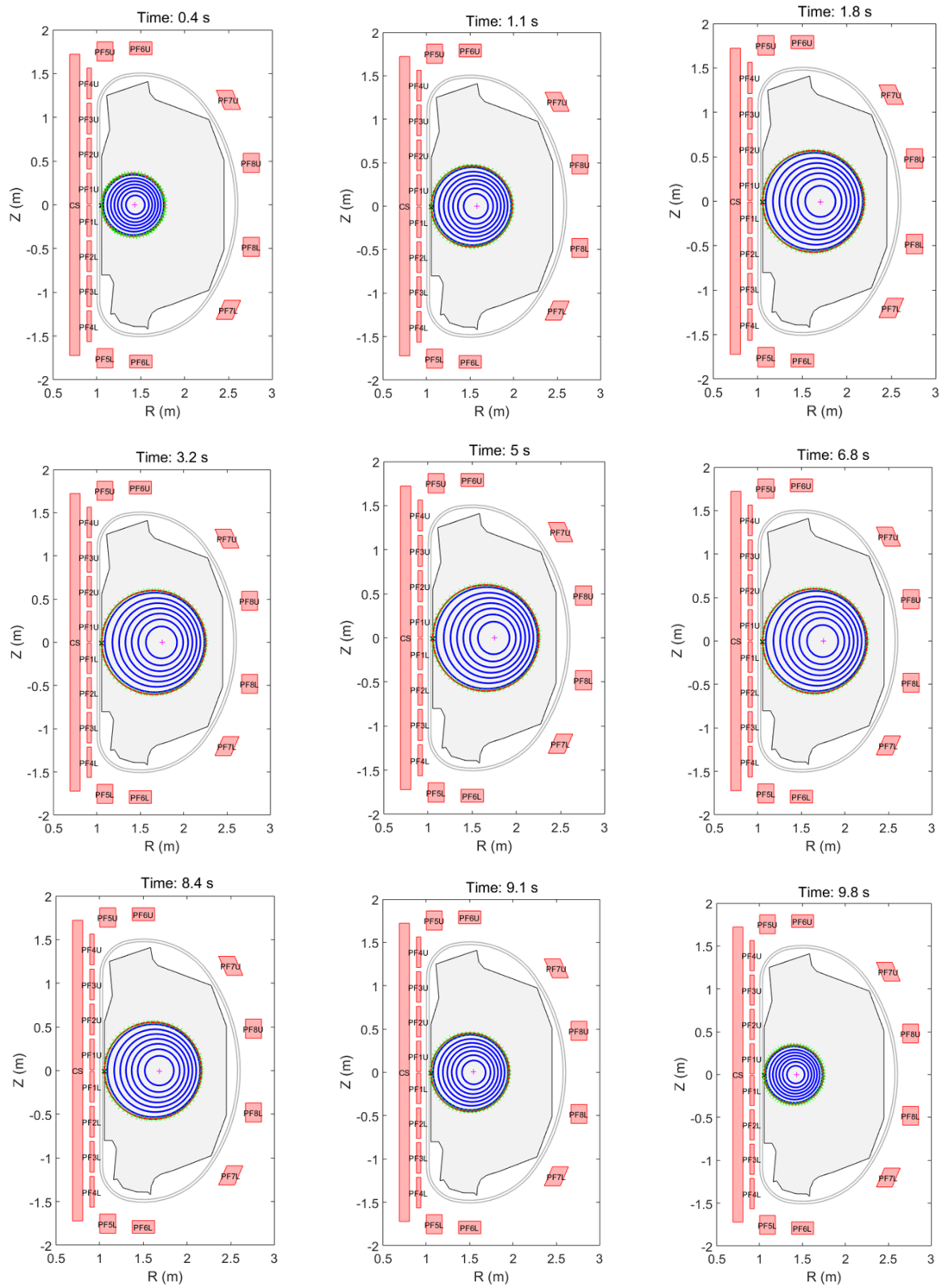
Figure 2.15: Level lines (blue) of the magnetic flux inside the plasma at selected times
for the calculation of a full scenario (ramp up, flat top, ramp down) for HL-2M, based on
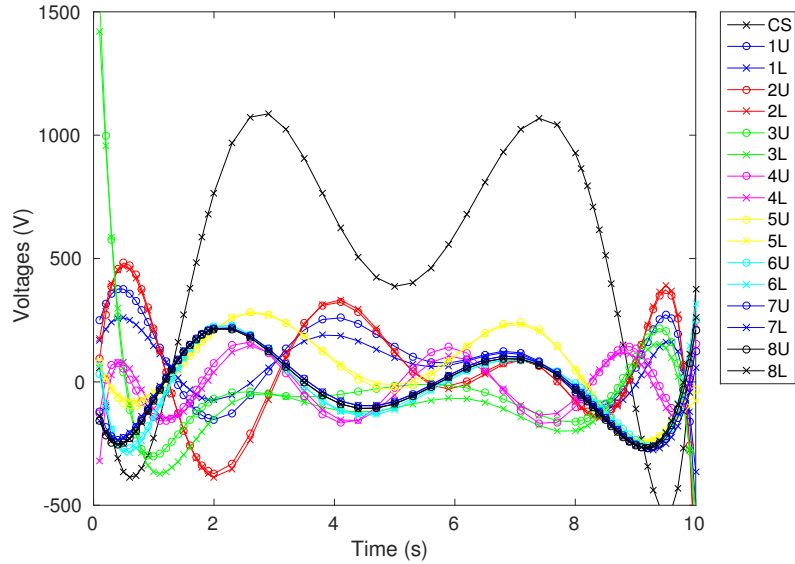60 time steps with prescribed boundaries (green dots) at each time step.

Figure 2.16: The voltages of the inverse evolution calculation for HL-2M. -

2.7   Summary

In this chapter, we firstly introduced the FBE equations. Then four types of FBE problems, i.e., *direct static/evolution* and *inverse static/evolution*, have been described. The recent FEEQS.M code and its variational and discretization formulations applied to solve the FBE problems have been introduced. Verification tests on the calculation of derivatives have been presented. Finally, first tests of the *inverse evolution* mode for example cases in the WEST and HL-2M tokamaks have been shown. In the following chapters, we present "real" applications of FEEQS.M. In **Chapter 3**, we apply the *inverse static* mode to identify the operating space in terms of plasma equilibrium in ITER. In **Chapter 4**, we apply the *inverse evolution* mode to develop a fast limiter to divertor transition in WEST.

Chapter 3

ITER equilibrium operating space identification

In a tokamak, the central solenoid (CS) and poloidal field (PF) coils always have limitations in the current they can carry, the force they can handle and, for superconducting coils such as in ITER, the magnetic field they can tolerate. It is clear that these limitations will translate into restrictions on the accessible domain of plasma equilibria, but it is not easy for a human to determine exactly what these restrictions will be.

We present herein a new method, to identify the equilibrium operating space. This method is applied to the ITER 15 and 17 MA inductive scenarios. Parts of the related work have been published in [77], and we give in this chapter the details.

In this chapter, the updated ITER CS and PF systems, as well as their limits are firstly described in section 3.1. Then, a review of previous works on identifying the ITER operating space is provided in section 3.2. Our new approach, which is based on the inverse static mode of the FEEQS.M code, is introduced in section 3.3, and applied to ITER with different penalization terms in sections 3.4, 3.5 and 3.6. Moreover, results about the effect of different plasma profile parameters (β_p) on the ITER operating space, are presented in section 3.7. Lastly, a short summary and discussion of this chapter are presented in section 3.8.

Table 3.1: Location of the CS and PF conductors, R, Z position and their dimensions (ΔR,ΔZ) as well as number of turns (N). Data are given in the ITER CATIA system of co-ordinates (TGCS).

Coil	R,m	Z,m	ΔR	ΔZ	N
CS3U	1.6870	5.4640	0.7400	2.0930	554
CS2U	1.6870	3.2780	0.7400	2.0930	554
CS1U	1.6870	1.0920	0.7400	2.0930	554
CS1L	1.6870	-1.0720	0.7400	2.0930	554
CS2L	1.6870	-3.2580	0.7400	2.0930	554
CS3L	1.6870	-5.4440	0.7400	2.0930	554
PF1	3.9431	7.5741	0.9590	0.9841	246.8
PF2	8.2851	6.5398	0.5801	0.7146	115.2
PF3	11.9919	3.2752	0.6963	0.9538	185.9
PF4	11.9630	-2.2336	0.6382	0.9538	169.9
PF5	8.3908	-6.7269	0.8125	0.9538	216.8
PF6	4.3340	-7.4665	1.5590	1.1075	459.4

3.1 ITER CS and PF requirements and reference separatrix

The latest (July 2017) ITER CS and PF coils data is defined in [78], which also gives the maximum currents, field and forces on CS and PF coils, as well as the reference plasma separatrix in detail. In this section, we introduce only the limits which are related to the equilibrium operating space.

3.1.1 ITER CS and PF coils

The ITER CS and PF coils position (R, Z co-ordinates of the conductor cross section centre at 4 K), the radial and vertical dimensions of the conductor cross section (ΔR, ΔZ) as well as the total number of turns (N) are given in table 3.1. The layout of CS and PF coils is presented in figure 3.1.

3.1.2 Maximum currents and fields on CS and PF coils

The dependence of the maximum current per turn on the maximum magnetic field on the coil conductor, is obtained by linear interpolation or extrapolation, between or beyond pairs of values given in table 3.2. In this work, only the cases with maximum
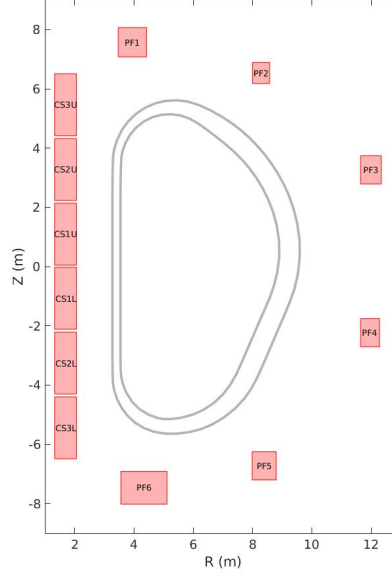
Figure 3.1: ITER CS and PF coils configuration. - (The two gray layers are the vacuum vessels.)

currents are considered for simplicity, e.g., the current and field limits on CS coils are 45 kA/turn and 12.6 T, respectively. It should be noticed that CS1U and CS1L are connected in series, which means the currents in them are always the same.

There also exists a limit on the absolute value of imbalance current in the coils PF2 to PF5, i.e., the current flowing in the vertical stabilization converter, which is calculated as:

$$I_{imb} = I_{PF_2} + I_{PF_3} - I_{PF_4} - I_{PF_5} \qquad (3.1)$$

should be less than 22.5 kA.

3.1.3 Maximum forces on CS and PF coils

The force limits are mainly the vertical forces on PF coils, the vertical separating and net forces on the CS coils system.

The limits on the vertical forces of PF coils are shown in table 3.3.

The vertical separating (see figure 3.2) and net force limits on the CS coils are

Table 3.2: Maximum currents in one turn of the CS and PF coils and maximum values of the magnetic field on the coils.

Coil	$I_{\max}$	$B_{\max}$	Coil	$I_{\max}$	$B_{\max}$
CS3U	45 kA	12.6 T	PF1	48 kA	6.4 T
	40 kA	13.0 T		48 kA	6.4 T
CS2U	45 kA	12.6 T	PF2	55 kA	4.8 T
	40 kA	13.0 T		50 kA	5.0 T
CS1U	45 kA	12.6 T	PF3	55 kA	4.8 T
	40 kA	13.0 T		50 kA	5.0 T
CS1L	45 kA	12.6 T	PF4	55 kA	4.8 T
	40 kA	13.0 T		50 kA	5.0 T
CS2L	45 kA	12.6 T	PF5	52 kA	5.7 T
	40 kA	13.0 T		33 kA	6.0 T
CS3L	45 kA	12.6 T	PF6	48 kA	6.4 T
	40 kA	13.0 T		41 kA	6.5 T
			PF6	52 kA	6.8 T
			0.4K subcooling	41 kA	7.0 T

Table 3.3: Maximum vertical forces on the PF coils.

Coils	Maximum upward force, MN	Maximum downward force, MN
PF1	110	-150
PF2	15	-75
PF3	40	-90
PF4	90	-40
PF5	160	-10
PF6	170	-190
PF3+PF4	10	-60

expressed respectively as:

$$F_Z(Sep) = \frac{|F_Z(Upward)| + |F_Z(Downward)|}{2} \qquad \leq 120 \; MN \; ,$$

(note that $F_Z(Downward)$ has negative sign); (3.2)

$$F_Z(CS) = |\sum_{n=1}^{6} F_Z(CS \; coils \; number \; \text{``}n\text{''})| \qquad \leq 60 \; MN.$$

where the $F_Z(Upward)$ is the force CS3U (possibly pushed up by other CS coils) exerts on the top of the mechanical structure, and defined as the maximum of the following 6 values:

1): $F_Z(up, 1) := F_Z(CS3U)$,

2): $F_Z(up, 2) := F_Z(CS3U) + F_Z(CS2U)$,

3): $F_Z(up, 3) := F_Z(CS3U) + F_Z(CS2U) + F_Z(CS1U)$,

4): $F_Z(up, 4) := F_Z(CS3U) + F_Z(CS2U) + F_Z(CS1U) + F_Z(CS1L)$,

5): $F_Z(up, 5) := F_Z(CS3U) + F_Z(CS2U) + F_Z(CS1U) + F_Z(CS1L) + F_Z(CS2L)$,

6): $F_Z(up, 6) := F_Z(CS3U) + F_Z(CS2U) + F_Z(CS1U) + F_Z(CS1L) + F_Z(CS2L) + F_Z(CS1L)$

and the $F_Z(Downward)$ is the force CS3L (possibly pushed down by other CS coils) exerts on the bottom of the mechanical structure, and defined as the minimum of the following 6 values:

1): $F_Z(dn, 1) := F_Z(CS3L)$,

2): $F_Z(dn, 2) := F_Z(CS3L) + F_Z(CS2L)$,

3): $F_Z(dn, 3) := F_Z(CS3L) + F_Z(CS2L) + F_Z(CS1L)$,

4): $F_Z(dn, 4) := F_Z(CS3L) + F_Z(CS2L) + F_Z(CS1L) + F_Z(CS1U)$,

5): $F_Z(dn, 5) := F_Z(CS3L) + F_Z(CS2L) + F_Z(CS1L) + F_Z(CS1U) + F_Z(CS2U)$,

6): $F_Z(dn, 6) := F_Z(CS3L) + F_Z(CS2L) + F_Z(CS1L) + F_Z(CS1U) + F_Z(CS2U) + F_Z(CS1U)$

where $F_Z(CS3U)$, $F_Z(CS2U)$, ... $F_Z(CS3L)$ are the vertical forces on the CS coils $CS3U$, $CS2U$, ... $CS3L$.

The above definition of the separating force ($F_Z(Sep)$) is impractical to implement in our model. Hence, in this work we use a simplified treatment for the $F_Z(Sep)$, which is described in section 3.3.4.

3.1.4   ITER reference separatrix

The reference plasma boundary for ITER scenario in the flat top phase, as well as the first wall geometry, are shown in figure 3.3.
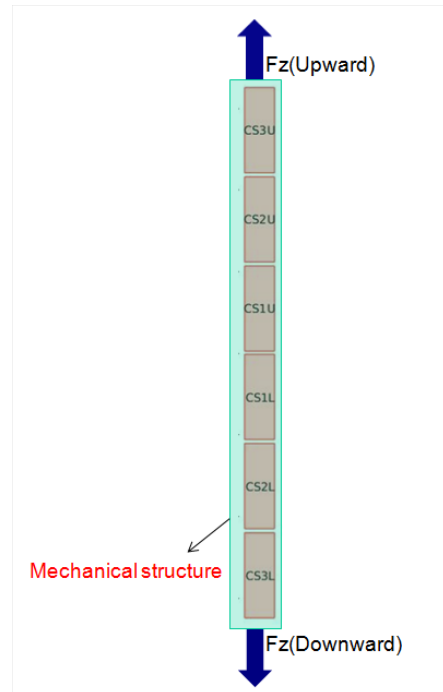
Figure 3.2: A simple sketch illustrating the separating force $F_Z(Sep)$ on CS coils -
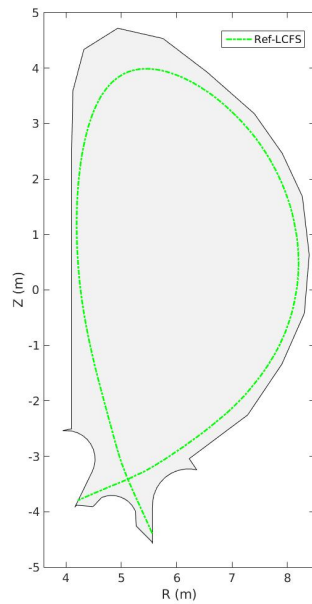
Figure 3.3: ITER first wall geometry and the reference flat top separatrix -

Roughly speaking, the objective is to remain close to the reference separatrix. More precise requirements are given in [78] and comprise among others:

- downward displacement of the inner divertor leg: 50 mm (maximum);

- upward displacement of the inner divertor leg: 150 mm (maximum);

- inward displacement of the outer divertor leg: 50 mm (maximum);

- outward displacement of the outer divertor leg: 150 mm (maximum);

- inward displacement near the inner limiter: 20 mm (maximum).

3.2 Previous results on the identification of the ITER equilibrium operating space

The typical method used in the past to determine the equilibrium operational space, was to run a series of inverse static FBE calculations (see **Chapter 2.3** in detail), in which the objective function was of the type:

$$\text{objective} = \frac{1}{2}\sum_{i=1}^{N_{\text{desi}}} \left(\psi(r_i, z_i) - \psi(r_{\text{desi}}, z_{\text{desi}})\right)^2 + \frac{1}{2}\sum_{i=1}^{N_i} w_i\, I_i^2 \qquad (3.3)$$

where the first part is called *cost function*, which quantifies the distance between the computed and desired plasma shape; and the second one is called *regularization term*, which is typically a weighted sum of the squares of the CS and PF coils currents, enables to deal with an ill-posed problem.

In the inverse static FBE calculations, I_P and plasma boundary are prescribed, while the plasma current profiles $\left(\beta_p \text{ and } l_i(3)\right)$ and value of Ψ_{st} [79] (the poloidal flux from all the contributions of CS and PF coils currents in a specified position inside the plasma area, representing different magnetization states for the CS and PF coils) are varied. This is because in the flat top phase, Ψ_{st} is varied in time due to the inductive flux consumption and plasma current profile, may also change due, e.g., to an L-H transition. The operating space domain is then determined by the limits of the CS and PF coils currents, field and forces. Since these limits are not explicitly implemented in the above objective function (3.3), the weights w_i must be tuned carefully until all the limits are respected. This appears as an impractical and time-consuming method.

3. ITER EQUILIBRIUM OPERATING SPACE IDENTIFICATION

Nevertheless, this method has been applied in the past with four independent equilibrium codes (EQ1 [80], EQ2 [81], EQ3 [82] and EQ4 [83]) to identify the ITER 15 MA operating space, as it was reported in [84]. Figure 3.4 gives the result, which shows that the ITER 15 MA scenario could only be operated in a very small area inside the $l_i(3)$-Ψ_{st} diagram, with original design parameters of the CS and PF currents, field and forces limits as well as the first wall geometry. Meanwhile, these studies found that β_p played a weak role in the operating space.
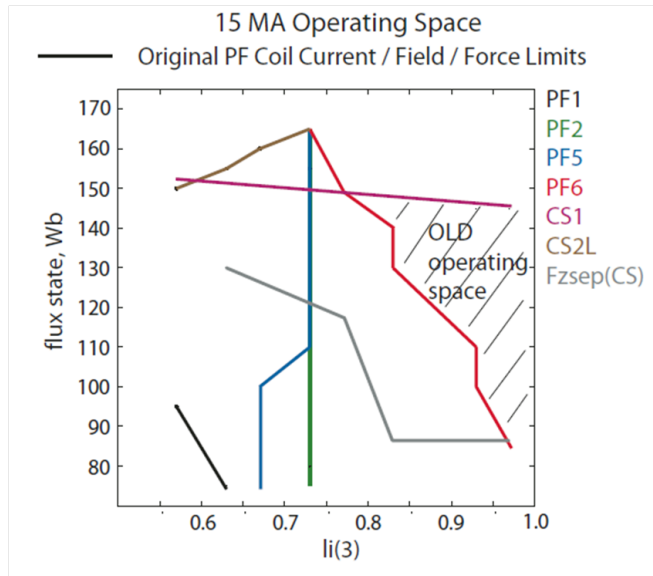

Figure 3.4: ITER 15 MA operating space with original design parameters of poloidal geometry, as well as the limits on CS and PF coils currents, field and forces [84] -

As a result, the ITER divertor dome, CS and PF geometry as well as the maximum currents and fields on PF1-6 were redesigned in 2009 to have a larger domain, as shown in figure 3.5.

The ITER 17 MA operating spaces were also calculated by these four codes, as visible in figure 3.6. Compared to the 15 MA case, the ITER 17 MA case has a smaller domain, as could be expected, since it is more difficult to operate the ITER scenario in a larger I_P. It may be noted in figure 3.6 that EQ1 and EQ4 include a pedestal, but not EQ2 and EQ3, which shows that the pedestal does not change the results dramatically.

Instead of using the simple objective function in equation 3.3, another possibility, as done with the CREATE-NL code in [85], is to linearize the inverse static FBE problem
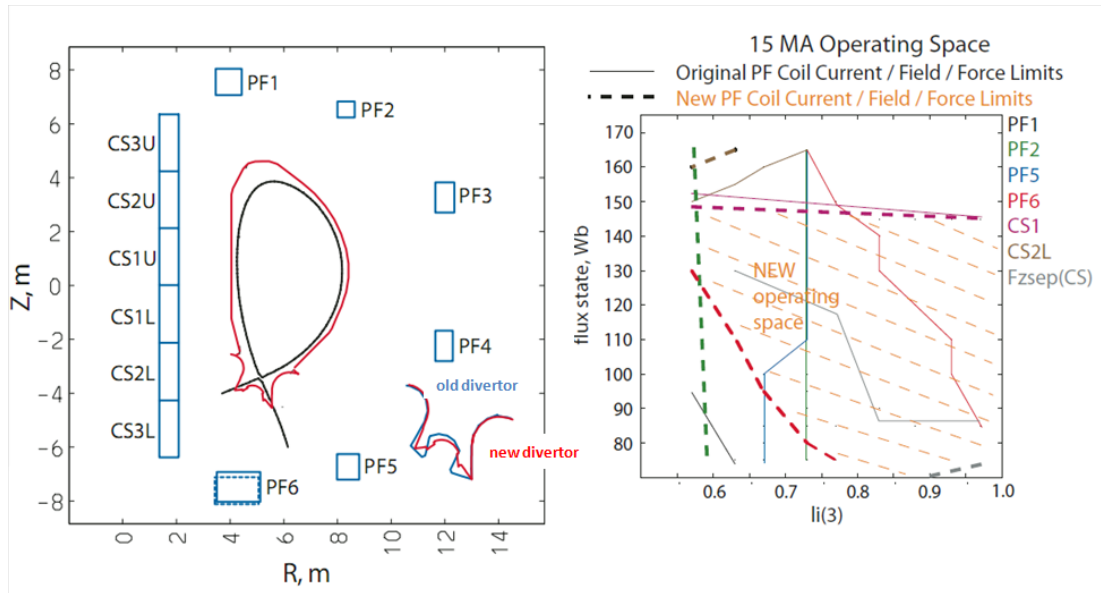
56

Figure 3.5: ITER 15 MA operating space with new (2009) poloidal geometry and the limits on CS and PF coils currents, field and forces [84] - left: the original design and updated divertor geometry, as well as PF6 position; right: the new ITER 15 MA operating space.
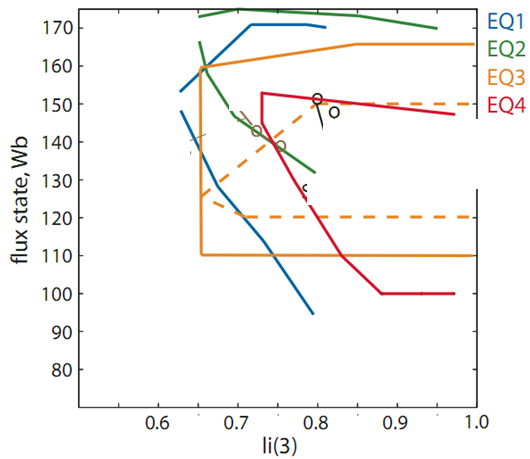

Figure 3.6: ITER 17 MA operating space with the updated (2009) poloidal geometry [84] -

and to express all the limits as inequalities which are function of the coils currents. This method was also applied on the ITER 15 and 17 MA cases, and the results are shown in figure 3.7. It can also be seen that the ITER 15 MA (BCOLMN line) has a larger domain of $l_i(3)$-Ψ_{st} than 17 MA (MQPON line). In the corners of the ITER 15 and 17 MA operating spaces, e.g., in Π, Σ, Φ, the forces limits are near to be violated and the deviations of plasma boundary are large.
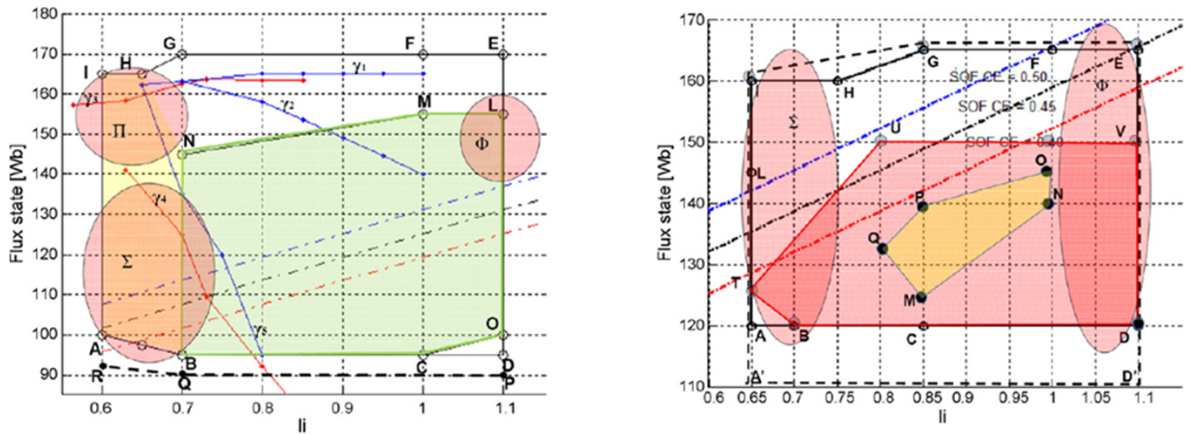

Figure 3.7: ITER operating space with the linear inequalities as the objective function [85] - left: ITER 15 MA operating domain in the Ψ_{st} - l_i domain (green area); right: ITER 17 MA operating domain in the Ψ_{st} - l_i domain (yellow area).

In around 2014, the ITER CS and PF6 coils were changed a little in [86], and the same method, which is based on the objective function in equation 3.3, was used to identify the new ITER 15 MA equilibrium operating space. The results are shown in figure 3.8, where the "old boundary" represents results with the ITER poloidal system description in 2009.

In general, we found that there were no reference ITER 15 and 17 MA equilibrium operating spaces after reviewing all the previous works, since every code had an individual result, and the reason was not yet clear.

3.3 A new approach to identify the ITER equilibrium operating space

In the previous works, the objective function was composed of the *cost function* and *regularization term.* However, the actual limits on the CS and PF coils currents, field
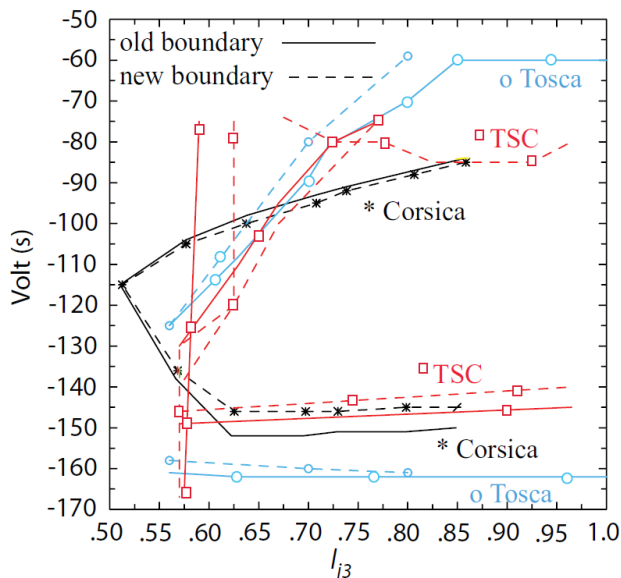
Figure 3.8: ITER 15 MA operating space with modified CS and PF6 coils positions in 2014 [86] -

and forces as well as the limits on the deviations from the reference separatrix were not explicitly considered (except via inequalities based on a linearized model in [85]). Moreover, these studies are not entirely up to date, since there have been some modifications on the location and number of turns for the CS and PF coils in 2017.

In this thesis, we propose another solution, introducing a new **Objective** function, which accounts for the true limits (updated in 2017) with the non-linear constraints in a more explicit way. The **Objective** function includes penalization terms which are activated or increase sharply when the limits are violated.

3.3.1 The new objective function

The new **Objective** function is expressed as:

$$\textbf{Objective} = \textbf{C}_{\textbf{Shape}} + \textbf{C}_{\textbf{Flux}} + \textbf{P}_{\textbf{Current}} + \textbf{P}_{\textbf{Force}} \tag{3.4}$$

where C represents *cost functions* and P represents *penalization terms*.

The first term,

$$\textbf{C}_{\textbf{Shape}}(\psi) = \frac{1}{2} \sum_{i=2}^{N} \left(\psi(r_i, z_i) - \psi(r_1, z_1) \right)^2 \tag{3.5}$$

is identical (or similar) to the *cost function* in the previous works, and it tends to make all the points (r_i, z_i), which describe the target separatrix, belong to the same flux surface. We have to note that $\mathbf{C_{Shape}}$ does not directly quantify the physical distance between the actual and the target separatrices. As a consequence, it is not possible to implement tolerances for this distance in the *cost function*. In present work, we only check these tolerances in post-processing. Being able to directly impose tolerances through the *cost function* would however be of high practical value, and is a direction for future work.

The second term,

$$\mathbf{C_{Flux}}(I_{coils}) = \frac{1}{2} \left(M \cdot I_{coils} - \Psi_{st} \right)^2 \tag{3.6}$$

aims at matching the desired value of the flux state Ψ_{st}. In this work, $(R_0, 0)$, where R_0 is the major radius, is selected as the specified position to calculate all the flux contributions from the CS and PF coils. Here M is the mutual inductance between the CS or PF coils and a toroidal wire at $(R_0, 0)$, which we pre-calculate with FEEQS.M in magnetostatic mode (i.e. direct static without plasma).

The third and fourth terms penalize respectively the violation of limits on the coils currents and forces. Here a penalization term is not used for the limits on the coils magnetic field for simplicity. Post-processing of the results presented below suggests that taking these limits into account would almost not change the operational domain, and the same is the case for the imbalance current I_{imb} in equation (3.1). In this chapter, we have tested two different types of penalization function, which will be described below in section 3.3.2.

We can see that there is no more *regularization term* in the new **Objective** function. Indeed, it appears not necessary any more, since the $\mathbf{C_{Flux}}$ term, which imposes the desired Ψ_{st}, already plays the role of a *regularization term*.

3.3.2 Mathematical functions for the penalization terms

We have tried two kinds of mathematical functions to penalize the violation of coils currents and forces, which are often used in neural networks: *rectifier* [87] and *softplus*

[88]:

$$\text{Rectifier: } = \max(x, 0)$$
$$\text{Softplus: } = \ln(1 + e^x)$$

(3.7)

In FEEQS.M, the quasi-Newton method in [68] is applied to find the solution of the non-linear inverse static FBE problem. The first and second derivatives of the **Objective** are used to find the direction and the step length of the iterations. Thus, in order to be able to differentiate two times the penalization terms, we modify the general *rectifier* and *softplus* to the *quasi-rectifier* and *quasi-softplus*, respectively, as:

$$\text{Quasi-rectifier: } = \big(\max(x, 0)\big)^3 = \max(x^3, 0)$$
$$\text{Quasi-rectifier-modified: } = \max\big((\frac{x + 0.5}{0.5})^3, 0\big)$$
$$\text{Quasi-softplus: } = \big(\ln(1 + e^x)\big)^3$$

(3.8)

where we also define another *quasi-rectifier-modified* function to activate the penalization term before the violation of the real limit.
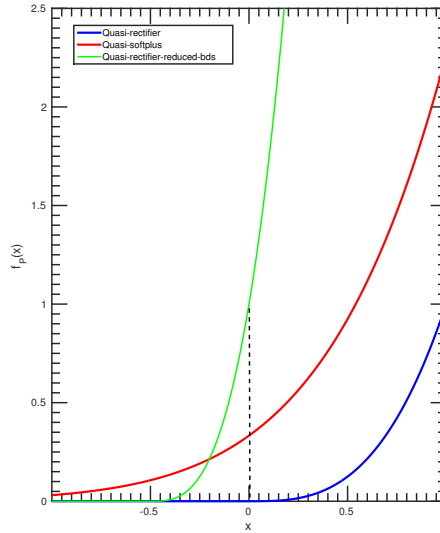

Figure 3.9: Plots for three types of penalization function: *quasi-rectifier* (blue), *quasi-rectifier-modified* (green) and *quasi-softplus* (red) - x=0 represents the limit value for coil current or force, while x= 0.5 for a half limit value.

The *quasi-rectifier*, *quasi-rectifier-modified* and *quasi-softplus* are presented in figure

3.9. With *quasi-rectifier*, the penalization terms are active only when the limit is violated (where x > 0). However, it is intuitive that penalization terms should become active already before the limits are violated, such that the code "knows" about the existence of these limits before hitting them. What is less clear is from which value of the current or force, and how sharply, the penalization terms should increase. For this reason, in the following sections, we will compare the results obtained with *quasi-rectifier-modified*, which activates when the current or force is above half the real limit and grows sharply, and with the *quasi-softplus* which is always active but grows more smoothly.

3.3.3 Penalization terms for the coils currents and forces

The penalization terms related to the CS and PF coils currents are defined as:

$$
\begin{aligned}
\mathbf{P_{Current}}(I_{coils}) = \sum_{i=1}^{N_{coils}} & f_P(\frac{I_i - I_{max,i}}{|I_{max,i}|}) \\
& + f_P(\frac{I_{min,i} - I_i}{|I_{min,i}|})
\end{aligned}
\tag{3.9}
$$

and the penalization term for the net force on the CS coils is given as:

$$
\begin{aligned}
\mathbf{P_{Force-CS}}(I_{coils}, \psi) = & f_P(\frac{\sum_{i=1}^{N_{CS}} F_{Z,i} - F_{max,CS}}{|F_{max,CS}|}) \\
& + f_P(\frac{F_{min,CS} - \sum_{i=1}^{N_{CS}} F_{Z,i}}{|F_{min,CS}|})
\end{aligned}
\tag{3.10}
$$

Here F_{max} (resp. F_{min}) and I_{max} (resp. I_{min}) represent the upper (resp. lower) limits of force and current, respectively, and f_P represents the *quasi-rectifier*, *quasi-rectifier-modified* or *quasi-softplus* in equation (3.8).

The penalization terms for the PF1-6 forces are also not considered here, since almost all the limits are naturally respected, as we have verified by post-processing.

The force penalization term concerns the volume integrated force which, due to axisymmetry, is vertical:

$$
F_{Z,i} = 2\pi \frac{I_i}{S_i} \int \partial_z \psi \, dS \qquad 1 \le i \le N_{coils}
\tag{3.11}
$$

where I_i is the CS or PF coil current, and S_i is the cross-section of the corresponding coil.

3.3.4 Penalization term for the separating force on CS coils

The penalization term for the separating force on CS coils is not as easy to express as the other terms in equations 3.9 and 3.10, due to its involved definition given in section 3.1.3. Moreover, we wish to be able to calculate the second and third order derivatives of this term.

Due to these difficulties, we have implemented the penalization term for the CS separating force, in the following form:

$$\mathbf{P_{Force-Sep}}(I_{coils}, \psi) = \sum_{i=1}^{6} \sum_{j=1}^{6} f_P\left(\frac{\frac{F_{Z0}(up,i)+F_{Z0}(dn,j)}{2} - F_{max,Sep}}{|F_{max,Sep}|} \right) \tag{3.12}$$

where $F_{max,Sep}$ is the limit of the separating force. The definitions of $F_{Z0}(up, i)$ and $F_{Z0}(dn, j)$, as well as the detailed justification of this expression are given in **Appendix C**.

At last, the total force penalization term is:

$$\mathbf{P_{Force}}(I_{coils}, \psi) = \mathbf{P_{Force-CS}}(I_{coils}, \psi) + \mathbf{P_{Force-Sep}}(I_{coils}, \psi) \tag{3.13}$$

It is worth noting that in the new **Objective** function (3.4), we have not found it necessary, at least for the applications presented below, to include weights to be adjusted in any of the terms. But the weights could be easily implemented in our approach.

3.3.5 The method to determine the operating space in the $l_i(3)$ - Ψ_{st} diagram

In order to determine the operating space in an $l_i(3)$ - Ψ_{st} diagram, we scan the plasma current profile parameter $l_i(3)$ (we will show later in section 3.7 that β_p does not change the operating space much), by scanning γ in equation (2.10), and we scan Ψ_{st} in equation 3.6. The other parameters of plasma current profile in equation (2.10), α and β, are fixed to 1 and 0.65, respectively (β_p =0.6 is the nominal value in the flat top phase for ITER inductive cases). Besides, a pedestal is not considered in the plasma current profile just for simplicity, but it would be interesting to explore the influence of the pedestal on the equilibrium operating space in future work.

The total number of inverse static FBE computations is 11 x 14: γ is scanned from 0.2 to 1.2 with a step of 0.1, and Ψ_{st} is scanned from -45 to -175 Wb with a step of

-10 Wb. During the Ψ_{st} and γ scanning loops, Ψ_{st} is varied from -45 to -175 Wb with a fixed γ. The result of the previous calculation is input as the initial guess for the next one, in order to save computation time. The convergence criterion for stopping the Newton iteration is :

$$\frac{\|I_{k+1} - I_k\|^2}{\|I_{k+1}\|^2} + \frac{\|\psi_{k+1} - \psi_k\|^2}{\|\psi_{k+1}\|^2} \leqslant \epsilon_0 \qquad (3.14)$$

where ϵ_0 is set to 1×10^{-11}.

The operating space can then be visualized by plotting the iso-lines of the currents, field and forces in the different coils, as well as of the boundary deviation metric (gaps) in the $l_i(3)$ - Ψ_{st} diagram. In particular, the domain is delimited by iso-lines corresponding to the limit values of these different quantities.
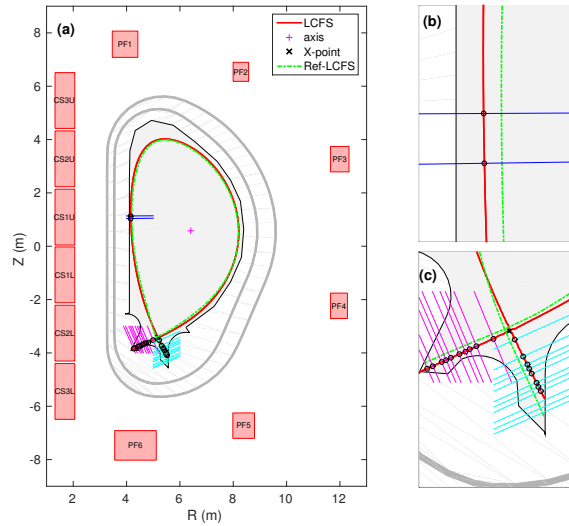

Figure 3.10: The definition of the separatrix deviation - a) overall deviations in the divertor and inner limiter gaps; b) the gap in the inner limiter; c) the distances in the divertor legs between the desired (red) and actual (green dot) boundaries.

The boundary deviation metric used in this work, is shown in figure 3.10. It consists of 20 gaps in the divertor legs and 2 gaps near the inner limiter. Note that by gaps here, we mean distances between the actual and desired separatrix (and not between the separatrix and the limiter). The gaps limits are defined in section 3.1.4.

The computation domain and mesh used in FEEQS.M, are presented in figure 3.11, where it can be seen that different sizes of triangles are used in different areas.
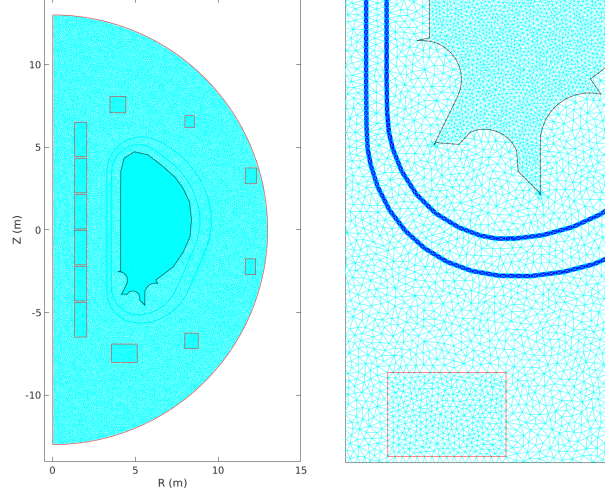
Figure 3.11: The computation domain and mesh used to solve the inverse static FBE problem with FEEQS.M for ITER. - The red rectangles represent coils, the black line is the first wall and the blue lines are the vacuum vessel.

3.4 ITER operating space identification with quasi-rectifier penalization terms

In this section, we present the ITER 15 MA operating space found with the new **Objective** function in 3.4, where all the currents and forces penalization terms are based on the *quasi-rectifier* function in equation 3.8. The total time to run the 11 x 14 inverse static FBE calculations is about 1.5 hours, on a standard HP notebook with a 4 x 2.7 GHz processor and 32 GB memory.

Before presenting the operating space, we show in the left plot of figure 3.12 the position of each of the 11 x 14 inverse static FBE calculations in the $l_i(3)$ - Ψ_{st} space, as well as the β_p in the right plot. It can be seen that the computed $l_i(3)$ are in the range of 0.5 - 1, although the prescribed γ are between 0.2 and 1.2. All the Ψ_{st} follow well the target values (from -45 to -175 Wb). All the calculated β_p are in the range of 0.53 - 0.59, which is close to the ITER nominal value of 0.6.

Figure 3.13 presents the ITER 15 MA equilibrium operating space found with *quasi-rectifier* as the coils currents and forces *penalization terms*. The lines are iso-contours of the coils currents, field and forces, as well as of boundary deviation metrics. The
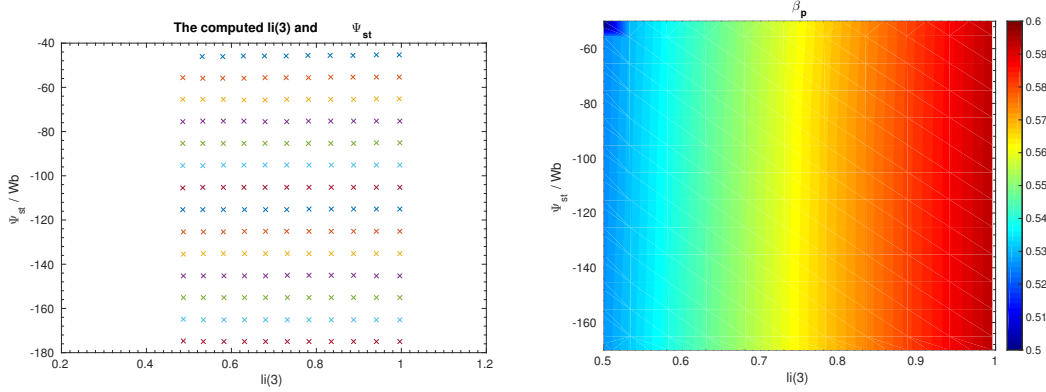
Figure 3.12: The computed $l_i(3)$ and Ψ_{st} (left), as well as the β_p (right) in 11 x 14 inverse static FBE calculations for the ITER 15 MA case, where the penalization terms in the **Objective** function are based on *quasi-rectifier*.

iso-contour corresponding to the limit value for each quantity, is given in dashed (current)/plain (field)/dotted (force)/dash dotted (boundary metric) bold. Plain thin lines are beyond the limits. The operating domain is therefore the zone left in white. The symbol '-' in the legend of figure 3.13 (same for the other operating spaces in the rest of this chapter) represents the lower limit and '+' is the upper limit, e.g., the 'Cur-CS1U&L-' represents the lower current limit of CS1U&L coil (which is -45 kA per turn, see table 3.2).

It can be seen in figure 3.13 that the operating space is small when compared to the previous works in figures 3.5, 3.7 and 3.8, especially for the domains of CS net $\big(F_Z(CS)\big)$ and separating $\big(F_Z(Sep)\big)$ forces. The smallness of these domains can be attributed to the small values of the forces penalization terms, compared to the other terms in the **Objective** (and in particular the $\mathbf{C_{Shape}}$ term), as it is shown in figure 3.14. Small values of the penalization terms in the **Objective** do not "incite" the code to redistribute the coils currents in order to respect the limits. Except the small domains for $F_Z(CS)$ and $F_Z(Sep)$, the operating spaces for the coils currents are similar to previous works, i.e., Cur-CS1U&L- bounds the high $|\Psi_{st}|$ area, and PF6 (both Cur-PF6+ and Field-PF6) bounds the small $l_i(3)$ - $|\Psi_{st}|$ area. Note that figure 3.14 shows that the value of $\mathbf{P_{Current}}$ is also small, so there may be possibilities to enlarge the domain of coils currents. Figure 3.14 also shows that the $\mathbf{C_{Flux}}$ term stays very small for all the inverse static calculations, meaning that all the prescribed Ψ_{st} are matched,
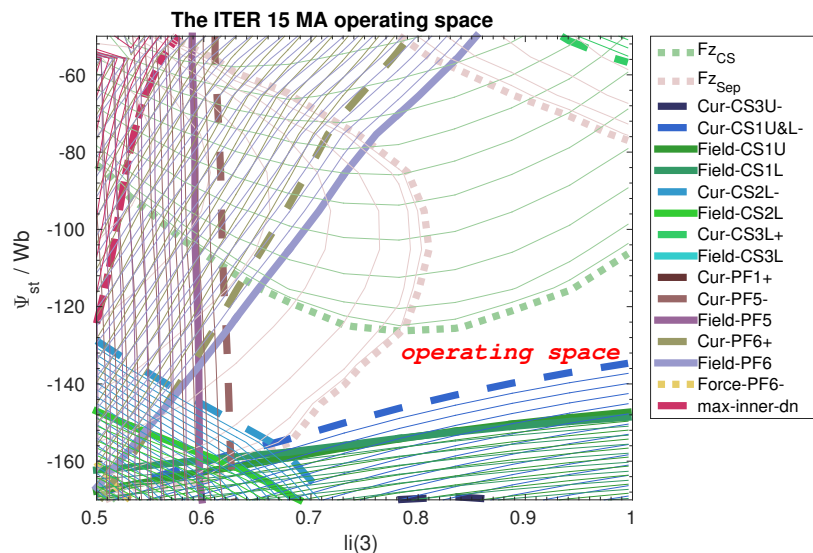
Figure 3.13: ITER inductive 15 MA operating space obtained by FEEQS.M. - where *quasi-rectifier* is selected as the penalization function for all the currents and forces, see the text for a description.

as already observed in figure 3.12 (left).

As it can be also seen in 3.14, $\mathbf{C_{Shape}}$ is the dominant term in the **Objective**. Therefore, the code puts the "priority" on optimizing the boundary deviations. As a result, only the maximum inner divertor leg *max-inner-dn* in the low $l_i(3)$-$|\Psi_{st}|$ corner of the domain, is above the tolerance (see figure 3.13), all the other boundary deviations are respected.

3.5 ITER operating space identification with quasi-rectifier-modified

The ITER 15 MA equilibrium operating space obtained in last section is small due to small values of the penalization terms $\mathbf{P_{Force-Sep}}$ and $\mathbf{P_{Force-CS}}$ when the limits are not strongly violated.

One possible way to solve this problem, as anticipated in section 3.3.2, is to activate the $\mathbf{P_{Force-Sep}}$ and $\mathbf{P_{Force-CS}}$ before the limits are violated, and/or to increase them more sharply when the limits are violated. Using the *quasi-rectifier-modified* function (defined in equation (3.8)) for the *penalization terms* does both of these (see figure 3.9).
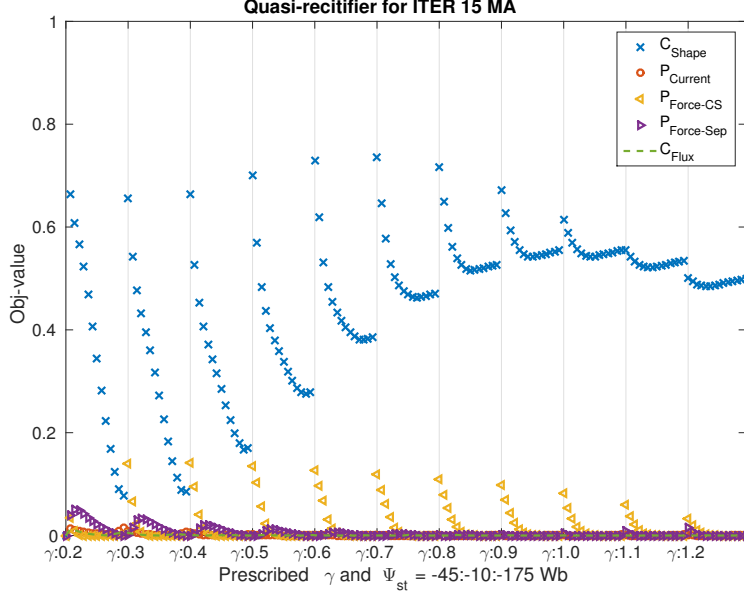
Figure 3.14: Values of all the C and P with *quasi-rectifier* terms. - Between 2 vertical lines, γ is fixed and Ψ_{st} is decreased from -45 to -175 with a step of -10 Wb.

Therefore, in this section, we modify the penalization term for coils currents as:

$$\mathbf{P_{Current}}(I_{coils}) = \sum_{i=1}^{N_{coils}} f_P(\frac{I_i - 0.5I_{max,i}}{0.5|I_{max,i}|})$$
$$+ f_P(\frac{0.5I_{min,i} - I_i}{0.5|I_{min,i}|}) \tag{3.15}$$

the penalization term for the net CS force $F_Z(CS)$ as:

$$\mathbf{P_{Force-CS}}(I_{coils}, \psi) = f_P(\frac{\sum_{i=1}^{N_{CS}} F_{Z,i} - 0.5F_{max,CS}}{0.5|F_{max,CS}|})$$
$$+ f_P(\frac{0.5F_{min,CS} - \sum_{i=1}^{N_{CS}} F_{Z,i}}{0.5|F_{min,CS}|}) \tag{3.16}$$

and the penalization term of CS separating force $F_Z(Sep)$ as:

$$\mathbf{P_{Force-Sep}}(I_{coils}, \psi) = \sum_{i=1}^{6} \sum_{j=1}^{6} f_P\Big(\frac{\frac{F_{Z0}(up,i)+F_{Z0}(dn,j)}{2} - 0.5F_{max,Sep}}{0.5|F_{max,Sep}|}\Big) \tag{3.17}$$

Note that here we choose a factor of 0.5, but the value may be varied (independently for each limit) if needed.
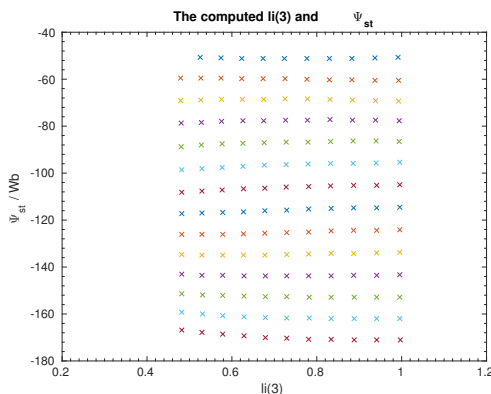
Figure 3.15: The computed $l_i(3)$ and Ψ_{st} in the 11 x 14 inverse static FBE calculations for the ITER 15 MA case, - in which all the current and force penalization terms are based on *quasi-rectifier-modified* function.

Figure 3.16 shows the ITER 15 MA operating space with the *quasi-rectifier-modified* penalization terms. It is substantially enlarged compared to the result in figure 3.13. The limits on $F_Z(CS)$ and $F_Z(Sep)$ are not violated anymore anywhere in the diagram. This is connected to the fact that all the values of $\mathbf{P_{Force-CS}}$ and $\mathbf{P_{Force-Sep}}$ are increased largely with this *quasi-rectifier-modified* penalization terms, as we can see in figure 3.17. At the same time, the domains for the coils currents and field are also enlarged a bit with the increased values of $\mathbf{P_{Current}}$. The new ITER 15 MA operating space is bounded by the Cur-CS1U&L- in the high $|\Psi_{st}|$ area, which seems logical since the main flux source is the CS. In the low $l_i(3)$ - $|\Psi_{st}|$ area, Field-PF6 bounds the operating space. Moreover, in the high $l_i(3)$ - low $|\Psi_{st}|$ area, the boundary deviation *max-inner-limiter* is the main constraint. The values of $\mathbf{C_{Flux}}$ are not 0 in all the inverse static calculations, especially in the areas of large prescribed Ψ_{st}. This means that the desired Ψ_{st} are not exactly obtained, which changes the way the $l_i(3)$ - Ψ_{st} space is mapped by the 11 x 14 calculations. However, figure 3.15 shows that this is a small effect. Furthermore, this effect is taken into account in figure 3.16, in which the y coordinate corresponds to the obtained Ψ_{st} and not the desired Ψ_{st}.

Although $\mathbf{C_{shape}}$ is still dominant in figure 3.17, the code now takes the coil current and force limits more into account. As a result, the domains for the boundary deviations are smaller in figure 3.16 than in figure 3.13, because the code needs to find a compromise between matching the desired plasma shape and matching the coils limits.

Figure 3.16: ITER inductive 15 MA operating space obtained by FEEQS.M - where *quasi-rectifier-modified* is selected as the penalization function for all the currents and forces, in which all the limits in the currents and forces are decreased by timing a factor of 0.5, see the text for a description.
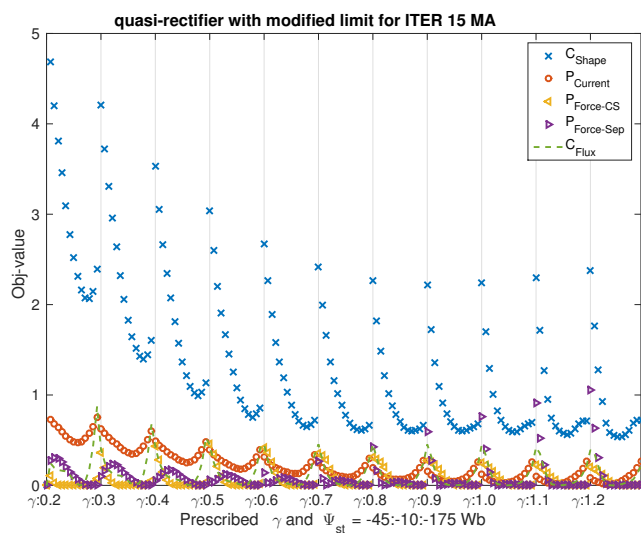
Figure 3.17: Values of all the C and P with *quasi-rectifier-modified* terms, in which all the limits of currents, CS separating and net forces are multiplied by a factor of 0.5. - Between 2 vertical lines, γ is fixed and Ψ_{st} is decreased from -45 to -175 with a step of -10 Wb.

Generally speaking, the ITER 15 MA operating space identified with the penalization terms based on *quasi-rectifier-modified* is quantitatively rather similar to what had been found in previous works (figures 3.5 and 3.8).

3.6 ITER operating space identification with quasi-softplus penalization terms

Section 3.4 and 3.5 have shown the importance of using *penalization terms* which become active before the limits are violated. In this section, we will investigate the effect of the shape of the penalization function. Instead of using the *quasi-rectifier-modified*, which activates close to the limit and increases very sharply, we will use the *quasi-softplus*, which is always active but grows more smoothly.

3.6.1 ITER 15 MA equilibrium operating space with quasi-softplus

We do similar inverse static FBE calculations in FEEQS.M again here, but with *quasi-softplus* as *penalization terms* in the **Objective** function. The total computation time is increased to about 3.5 hours, which is due to the fact that the code needs more Newton iterations to converge. The latter is probably related to interplay between the many *penalization terms.*

The ITER 15 MA operating space found using the *quasi-softplus* is presented in figure 3.18. We can see that it is similar to the operating space found with the *quasi-rectifier-modified* presented in the previous section (figure 3.16), although it is globally smaller. To be more specific, the domain is enlarged a bit in the low $l_i(3)$ - high $|\Psi_{st}|$ corner, but it is substantially reduced in the high $l_i(3)$ - low $|\Psi_{st}|$ corner. As a side remark, we can note that this corner is bounded by the *max-inner-limiter* limit in both cases, which suggests that adding a penalization term for this limit (and, more generally, for boundary deviations) is a useful direction for future work. The values of the different terms of the **Objective** are given in figure 3.19. We can see that all the C (except $\mathbf{C_{Flux}}$) and P terms are of the same order of magnitude, which means that with the *quasi-softplus*, the code tries to find a more "global" compromise than with the *quasi-rectifier-modified*, as could be expected.
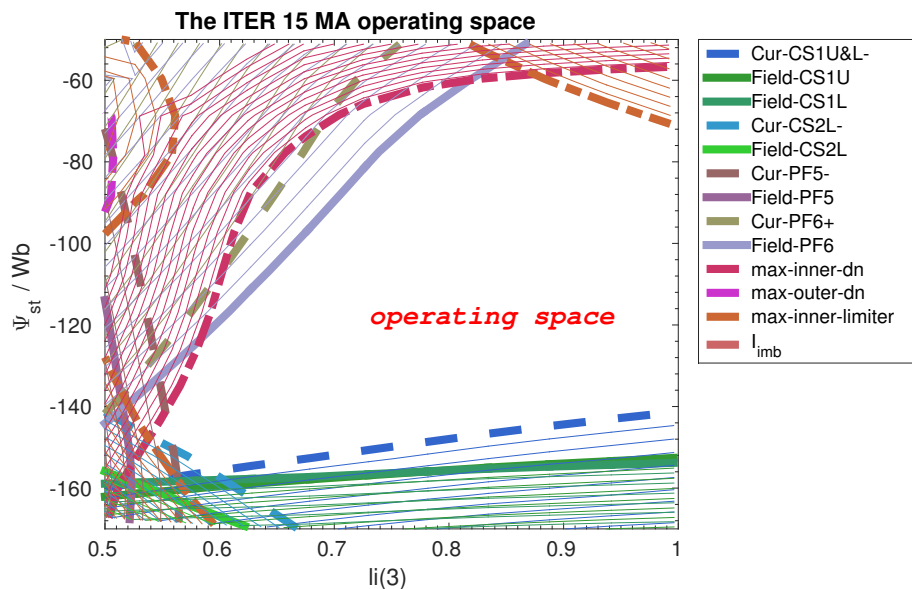
Figure 3.18: ITER inductive 15 MA operating space obtained by FEEQS.M - where *quasi-softplus* function is selected as the penalization function for all the currents and forces, see the text for a description.
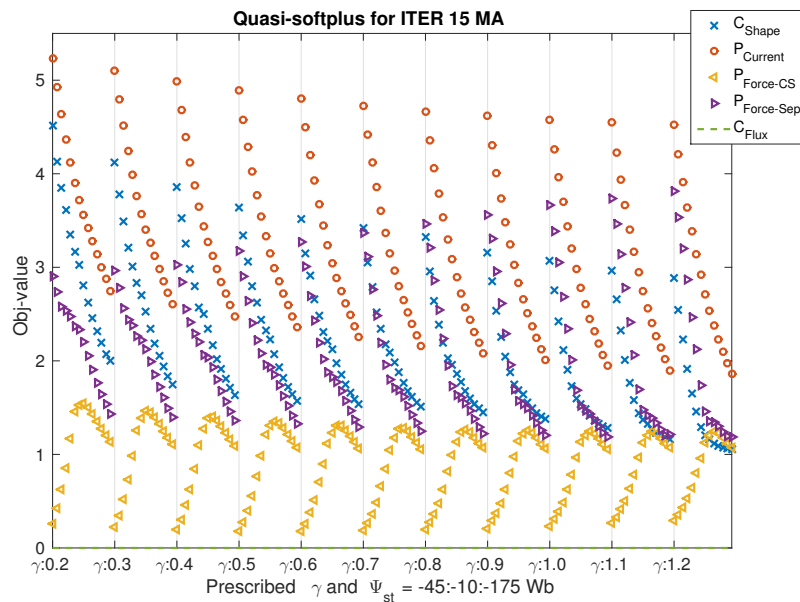
Figure 3.19: Values of all the C and P with *quasi-softplus* terms. - Between 2 vertical lines, γ is fixed and Ψ_{st} is decreased from -45 to -175 with a step of -10 Wb.

3.6.2 ITER 17 MA equilibrium operating space with quasi-softplus

We also applied the same inverse static FBE calculations with the *quasi-softplus* based *penalization terms* for the ITER 17 MA case, and figure 3.20 shows the resulting operational domain.
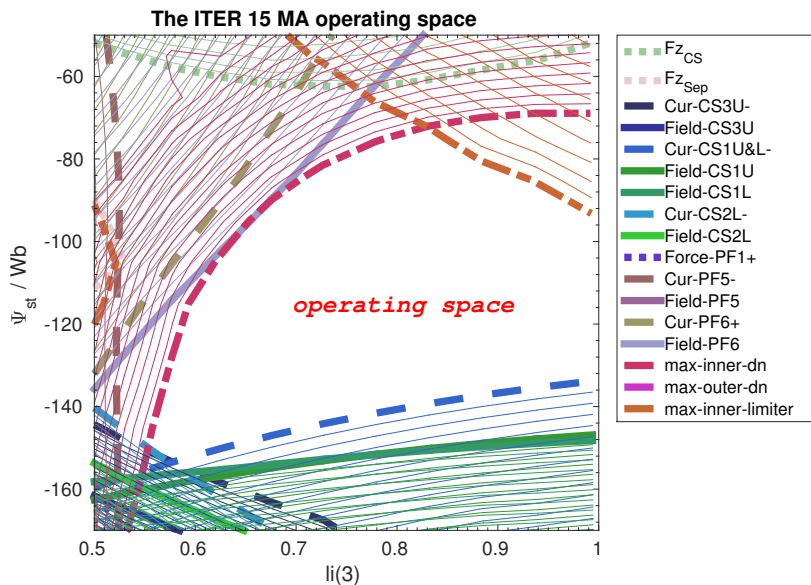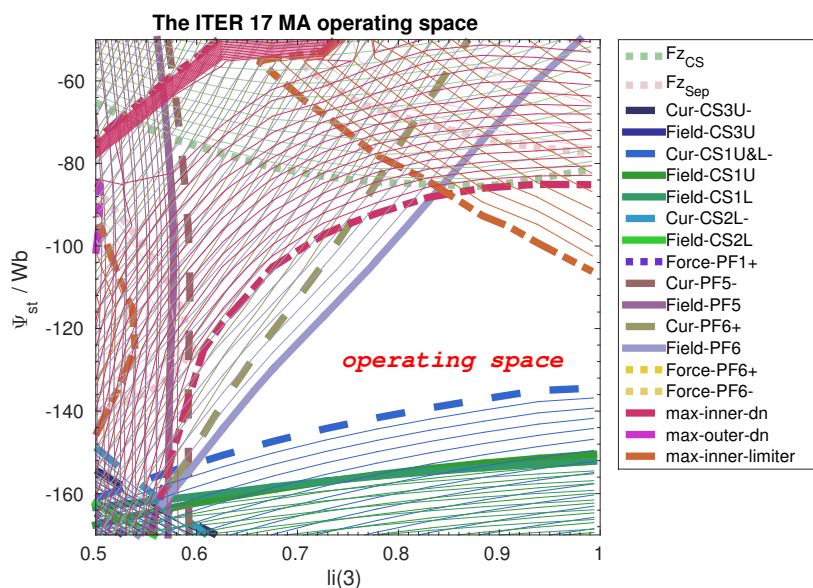

Figure 3.20: ITER inductive 17 MA operating space obtained by FEEQS.M - where *quasi-softplus* function is selected as the penalization function for all the currents and forces, see the text for a description.

It has a similar Cur-CS1U&L limitation in the high $|\Psi_{st}|$ area to the 15 MA case. However, the 17 MA domain is considerably reduced by limitations on the PF6 current and field, especially in the low $l_i(3)$ - $|\Psi_{st}|$ corner, since more PF6 current is required when I_P is increased. The boundary deviation *max-inner-limiter* also reduces the domain in the high $l_i(3)$ - small $|\Psi_{st}|$ corner.

Generally speaking, the ITER 17 MA operating space found with the *quasi-softplus* based *penalization terms* is similar to the previous results shown in figure 3.6.

3.7 Sensitivity on β_p of the operating space

It was mentioned in [84] that the parameter β_p plays a minor role in the ITER equilibrium operating space, but no evidence was given to support this statement. With
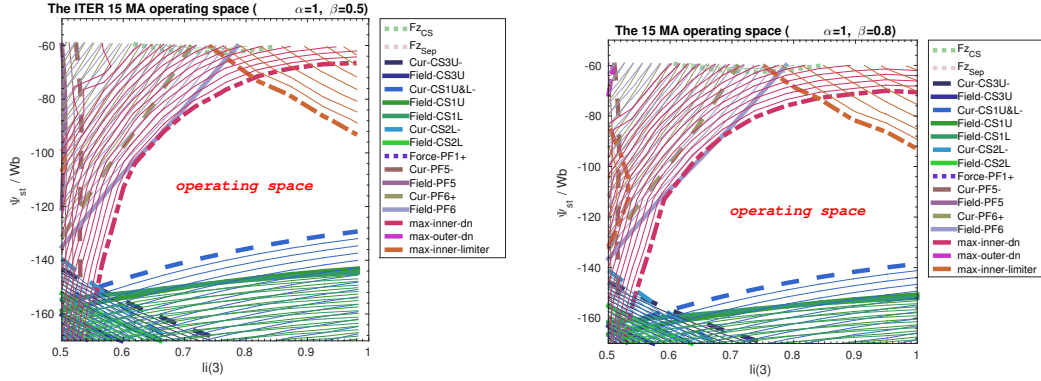
β=0.5 (β_p=0.4-0.45) β=0.8 (β_p=0.66-0.73)

Figure 3.21: The ITER 15 MA operating spaces with different prescribed β and β_p in plasma profile, the *penalization terms* are based on the *quasi-softplus* function.

our approach, it is straightforward to test the effect of β_p. This can indeed be done by changing the prescribed β in the plasma profile equation (2.10).

Figure 3.21 presents the ITER 15 MA equilibrium operating spaces obtained with β=0.5 (which results in β_p=0.4-0.45) and β=0.8 (β_p=0.66-0.73), using the *quasi-softplus* for the *penalization terms*. We can see that they are similar to each other, and also similar to the case in figure 3.18, where β=0.65 (β_p=0.53-0.59), confirming the moderate effect of β_p on the operating space.

3.8   Summary and discussion

In this chapter, after describing the ITER PF system (including limitations on the coils currents, field and forces) as well as the reference plasma boundary and tolerances on deviations from it, we reviewed previous works on the identification of the ITER 15 and 17 MA operating spaces. The latter use a series of inverse static FBE calculations in which the coils or boundary deviation limits are not explicitly taken into account (except via inequalities on the coils currents based on a linearization around a certain equilibrium). Then, we introduced a new **Objective** function that includes terms which penalize the violation of the coils currents and forces limits.

These penalization terms, which have been implemented in FEEQS.M, allow for an

automatic identification of the ITER operating space with no need for a human to tune parameters. This approach is therefore both more rigorous and faster.

Then, we analyzed the ITER 15 MA operating space found by FEEQS.M and we compared the results with different types of penalization functions: *quasi-rectifier*, *quasi-rectifier-modified* and *quasi-softplus*.

A very limited operating space was found with the *quasi-rectifier*, which we attribute to the fact that this penalization function becomes active only above the limit, and grows rather slowly. In contrast, the *quasi-rectifier-modified* and *quasi-softplus* based *penalization terms* are active already significantly before the limit is violated and grow much faster as the limit is approached and overcome. As a result, the operating space found with these functions is much larger. Meanwhile, the difference between the latter 2 operating spaces are quite small, meaning that the operating space is not very sensitive to the exact shape of the penalization function. However, the operating space is slightly larger with the *quasi-rectifier-modified* which is likely due to the fact that *quasi-softplus* activates further away from the limit, resulting in unnecessary constraints on the coils currents distribution. Broadly speaking, the ITER 15 MA operating space identified with FEEQS.M is similar to the one identified in previous works.

It is likely that there exists "better" penalization functions than the ones we have used here, providing larger operating spaces. It would be interesting to try to find them. However, the rather weak difference found between the *quasi-rectifier-modified* and *quasi-softplus* functions suggests that there is probably not a lot to gain.

Instead, from a practical point of view, the highest priority may be to implement constraints on the plasma shape in an explicit way. This may allow, e.g., to enlarge the domain in the high $l_i(3)$ - low $|\Psi_{st}|$ corner.

Exploiting the rapidity of our new tool, we have repeated the identification of the operating space for 17 MA (with similar results as in previous works) and also for different β_p at 15 MA (confirming the small influence of β_p on the operating space).

Chapter 4

Development of a fast limiter to divertor transition in WEST

As mentioned in **Chapter 1.2.2**, the WEST tokamak aims at testing ITER-like tungsten (W) plasma facing components in steady state operation. However, interactions between plasma and the W first wall can lead to accumulation of W in the plasma, especially when the plasma stays during a long time in limiter configuration at the beginning of the pulse, such as experienced in the JET [89, 90, 91] and ASDEX-U [92, 93, 94] tokamaks. It is therefore important to develop scenarios that minimize the time spent in limiter configuration and switch as soon as possible into divertor configuration.

A typical way to design scenarios in terms of plasma shape evolution is to find adequate PF coils currents at selected times (e.g. using inverse static FBE calculations), and construct temporal waveforms from these snapshots taking into account the voltage capabilities of the PF power supplies and the estimated flux consumption from the plasma, as done, e.g., in [95]. On WEST, the snapshots sequence has been developed by a combination of inverse static FBE calculations (which has the drawback of neglecting the induced currents in the passive structures, in particular when the plasma current is ramped up and down) and trial and error on the machine, and has not been optimized to minimize the time spent in limiter configuration.

In this chapter, we present a more sophisticated method of scenario development based on the *inverse evolution* mode of FEEQS.M, which we apply in order to speed up the limiter-divertor transition at the beginning of a WEST pulse. More precisely, we use

the coils currents waveforms calculated by FEEQS.M as feedforward (FF) trajectories
for the plasma control system. Note that on the other hand, we do not use the voltages
calculated by FEEQS.M, since the WEST magnetic control strategy (described below)
is based on using coils currents to control the plasma position and shape, while another
control loop provides adequate voltages to match the desired currents (this approach
is applied in many tokamaks and not specific to WEST).

The outline of this chapter is as follows. Section 4.1 introduces the WEST magnetic
control architecture, which is necessary to understand what comes after. Section 4.2
describes the typical WEST scenario in what concerns the plasma shape evolution at
the beginning of a pulse. Section 4.3 presents the method used to design a faster
limiter to divertor transition with the *inverse evolution* mode of FEEQS.M. Section 4.5
discusses the validation of this fast transition in simulation, making use of the WEST
magnetic control simulator. Section 4.6 presents the first experimental tests of the
fast transition on WEST. Section 4.7 presents a summary and discussion of possible
directions for future work.

4.1 The magnetic control on WEST

The WEST control system [96], which is based on the Discharge Control System (DCS)
of ASDEX-U [97], has allowed obtaining successfully the first plasma in December 2016
[98]. It can now operate routinely the WEST plasma scenarios in limiter and divertor
configurations, in a stable and reliable way [99]. Magnetic control, i.e. the control of
plasma current, position and shape using the poloidal field system, is a key part of
the WEST control system. In this section, we introduce the WEST magnetic control
architecture.

4.1.1 General magnetic control strategy

A basic introduction to magnetic control in WEST has been given in **Chapter 1**.**4.1**,
and we present here the control strategy in more detail.

The magnetic control scheme which is embedded in the more general WEST control
system is shown in figure 4.1. Its output is a set of voltages (V_{supply} in figure 4.1) to
be applied by the power supplies of the poloidal (field) system. The magnetic control
scheme is functionally divided into 2 parts: plasma control and poloidal (field) control.
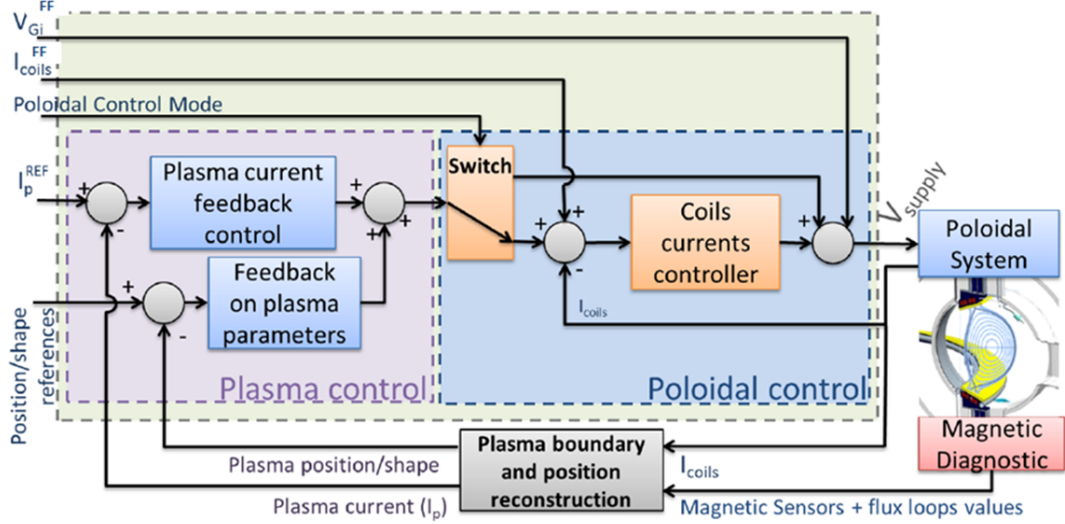
Figure 4.1: The block diagram of the WEST magnetic control loop. - Reproduced from [100].

The plasma control part provides the poloidal control part with coils currents or voltages requests, depending on the position of the **Switch** in figure 4.1. Note that in the present case, the former applies in what concerns the position and shape control, i.e. currents requests are used. These requests are adjusted to feedback (FB) control the plasma current, position and shape. In the present case, we focus on the beginning of the pulse, when only the (R,Z) position of the plasma center is FB controlled. The poloidal control part then turns these inputs into voltages requests for the power supplies, after adding FF contributions. The plasma current, position and shape, are provided by the real time (RT) equilibrium reconstruction code VATCH [101], whose input are magnetic measurements by pick-up coils and flux loops [102].

Figure 4.2 presents the layout of the WEST PF coils. The A coil, also called CS, is used to control I_P. The Eh, Eb, Fh and Fb coils are the actuators to FB control the plasma radial position, while the Xh, Xb and Dh as well as Db coils are used to FB control the plasma vertical position. Figure 4.3 shows the WEST poloidal electrical circuits. It can be seen that the in-vessel Xh and Xb coils are each made of 4 sub-coils connected in series and separated from the rest, while the 9 ex-vessel coils are part of a common circuit.
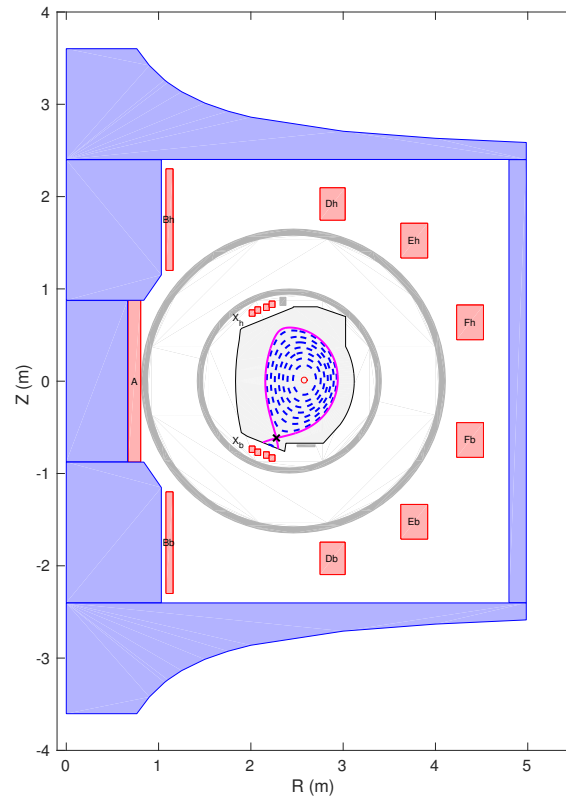
Figure 4.2: The poloidal geometry of WEST, and a typical diverted plasma shape, where red 'o' is the magnetic axis and black 'x' is the X-point. - The red areas are the coils, the purple ones are iron, and the gray areas are the vacuum vessels and passive plates.
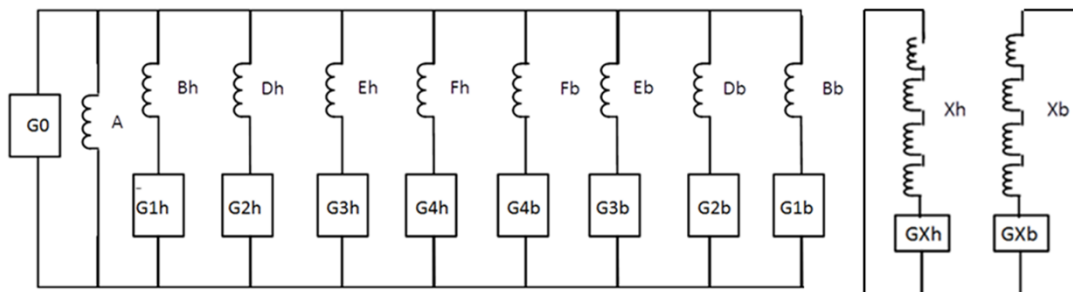

Figure 4.3: The WEST coils electrical circuits. - G stands for "generator", i.e. power supply.

4.1.2 Feedback control laws

In practice, I_P on WEST is controlled by the voltage of the G0 power supply (see figure 4.3) with a proportional (P) and integral (I) Single-Input/Single-Output (SISO) control law [103]:

$$V_{G0} = K_P(I_P - I_P^{Ref}) + K_I \int (I_P - I_P^{Ref}) \, dt \tag{4.1}$$

where K_P and K_I are the proportional and integral controller gains, I_P and I_P^{Ref} are the reconstructed and reference plasma currents, respectively.

The FB control on the plasma position and shape uses the coils currents with a PI Multi-Input/Multi-Output (MIMO) control law [104]:

$$I_{coils}^{FB} = A(y - y^{Ref}) + B \int (y - y^{Ref}) \, dt \tag{4.2}$$

where only the Dh/b, Fh/b and Xh/b (see figure 4.2) coils currents are included in I_{coils}^{FB}. y and y^{Ref} are the reconstructed and reference plasma position and shape parameters, respectively. A and B are proportional and integral gain matrices, respectively. The detailed method used to set up these gains is presented in [100].

The reference coils currents are then obtained by combining the FB term with a FF term:

$$I_{coils}^{Ref} = I_{coils}^{FB} + I_{coils}^{FF} \tag{4.3}$$

The FF coils currents are an essential part of the plasma position and shape control. Indeed, they should in principle determine the "nominal" trajectory of the plasma position and shape, while the FB part is supposed to make only small "corrections" to ensure that the position and shape are as close as possible to the desired ones. Our work described below consists in developing FF coils currents waveforms in order to speed up the formation of a divertor configuration. In fact, as already mentioned above, we focus on the beginning of the pulse, when only the position is directly FB controlled. However, it is essential to understand that the shape is somehow also controlled in this phase, via the FF coils currents.

Each coil current (except for the A coil) is FB controlled by the corresponding coil voltage with a SISO PI controller:

$$V_{coils}^{FB} = A'(I_{coils} - I_{coils}^{Ref}) + B' \int (I_{coils} - I_{coils}^{Ref}) \, dt \tag{4.4}$$

where A' and B' are proportional and integral gains, respectively.

This FB term is combined with a FF coil voltage:

$$V_{coils}^{Ref} = V_{coils}^{FB} + V_{coils}^{FF} \tag{4.5}$$

which is defined by:

$$V_{coils}^{FF} = R_{coils} I_{coils}^{Ref} \tag{4.6}$$

The vector of reference coils voltages V_{coils}^{Ref} is then converted into a vector of power supplies voltages V_{supply} taking into account the circuits shown in figure 4.3, and V_{supply} is finally sent to the power supplies through a RT network.

4.2 WEST scenario sequence

The reference WEST shot which we will use in this chapter is 53259. Figure 4.4 shows an overview of this shot. The plasma current (in blue) starts up at $t_0 \approx 32\,s$, then it ramps up for the first $3\,s$ of the pulse, followed by a flat top phase for about $6\,s$, and finally a ramp down over $2\,s$. The loop voltage used to sustain the plasma current is mainly induced by the swing of the A (CS) coil current (in red).

Figure 4.4 also presents the evolution of the plasma shape. The plasma starts in a limiter configuration after the breakdown, then it is progressively elongated in the vertical direction by increasing the Xb (and Xh) coil current (in purple) starting at $t_0 + 0.4\,s$. Finally, when the Xb (and Xh) currents are large enough (with respect to the plasma current), i.e. around $t_0 + 1.6\,s$, a lower single null (LSN) divertor configuration is formed.

4.3 Development of feedforward coils currents for a fast limiter-divertor transition

In this section, we describe in detail our work to construct waveforms of feedforward coils currents (I_{coils}^{FF}) in order to obtain a faster X-point formation than in shot 53259. For this purpose, we have used the *inverse evolution* mode of the FEEQS.M code (see **Chapter 2**.**4**.**2**).
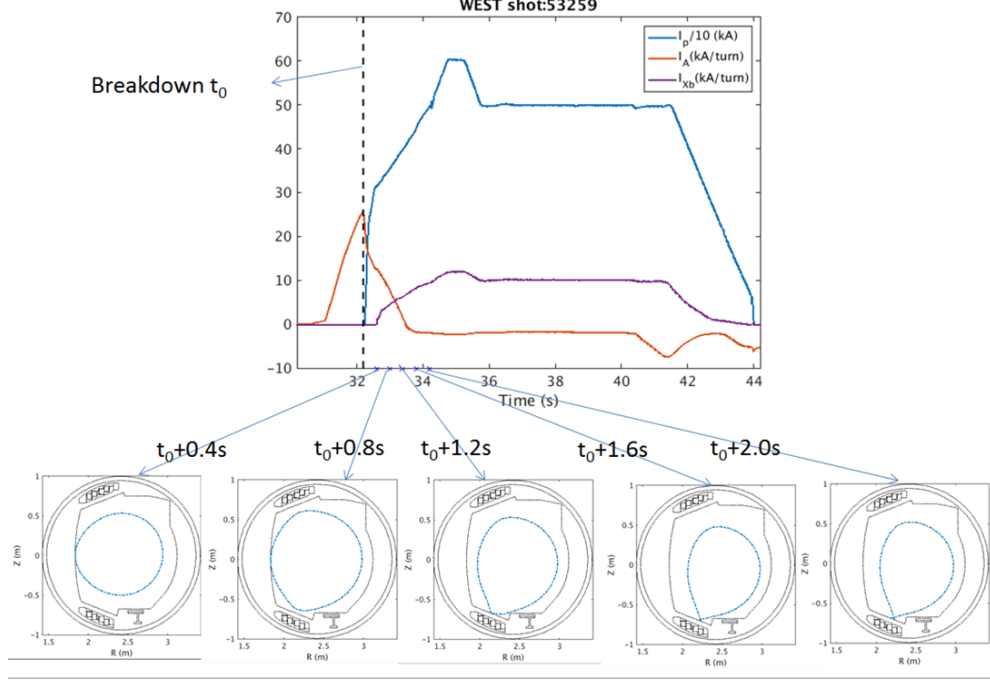
Figure 4.4: The WEST discharge scenario sequence of shot 53259. - The evolution of I_P, I_A and I_{Xb} as well as the shape trajectory after the breakdown.

More precisely, our objective was to modify the I_{coils}^{FF} waveforms after $t_0 + 0.4\,s$ (which corresponds to the moment when the X coils are activated in shot 53259), so as to form the X-point as fast as possible.

The inverse evolution mode of FEEQS.M needs as input an initial flux map ψ_0, waveforms for I_P and for the plasma profile parameters α, β and γ as well as the desired plasma shape and boundary flux ψ_{bd} (the latter is used to account for the flux consumption). We will now describe how these input parameters are set up.

4.3.1 Initial flux map

The initial ψ_0 map is obtained by running the *inverse static* mode of FEEQS.M (see **Chapter 2**.**4.2**), in which the **objective** is:

$$\textbf{objective} = \frac{1}{2}\sum_{i=2}^{N}(\psi(r_{i,start}, z_{i,start}) - \psi(r_{1,start}, z_{1,start}))^2 + \frac{1}{2}w\sum_{i=1}^{N} I_{coils,start}^2 \quad (4.7)$$

where $(r_{i,start}, z_{i,start})$ are the boundary points provided by the magnetic reconstruction code VACTH for shot 53259 at $T_{start} = t_0 + 0.4\,s = 32.5812\,s$. Only the currents in the
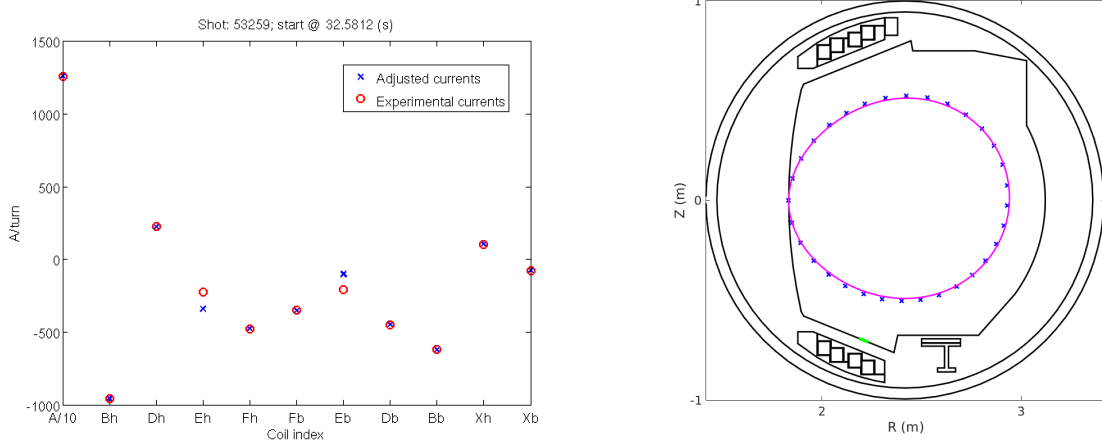
Figure 4.5: Left: coils currents, adjusted by FEEQS.M to match the VACTH plasma boundary (blue 'x') and experiment (red 'o'); right: initial boundary, as calculated by FEEQS.M (magenta '-') and reconstructed by VACTH (blue 'x').

Eh and Eb coils are free to be varied, all other currents are set to their experimental values. The weight $w = 1 \times 10^{-10}$. The plasma current is set to its experimental value, $I_{P,start} = 314.14$ kA. The plasma profile parameters α, β and γ are set in the same way as described in the following section 4.3.2.

The inverse static calculation results are shown in figure 4.5. It can be seen that the VACTH plasma boundary is well matched, but that the Eh and Eb coils currents are a little different to their experimental values. The cause of this deviation, which is typically observed when performing this type of exercise for any WEST pulse, has not been identified yet.

4.3.2 Evolution of plasma parameters

The plasma current evolution $I_P(t)$ used in the inverse evolution calculation is the experimental one. It should be noted that the transition to divertor shape is performed at the same time as I_P is being ramped up. The associated flux consumption will be imposed via the objective function (see below).

The α parameter is set to 1 at all times. The evolution of the other plasma profile parameters β and γ, is obtained from running inverse static FEEQS.M calculations

at each time step, and scanning these parameters in order to best match the value of $\beta_p + l_i(3)/2$ estimated by VACTH as well as the experimental value of $I_{Eh} + I_{Eb}$. The values of β and γ in the time interval of interest are close to 0.5 and 0.8.

4.4 Objective function

The objective function used for the inverse evolution calculation, is the following:

$$
\begin{aligned}
\textbf{Objective} = \ & \frac{1}{2} \int_{T_{start}}^{T_{end}} \sum_{i=1}^{N_{\text{desi}}} \Big(\psi\big(r_i(t), z_i(t), t\big) - \psi\big(r_{desi}(t), z_{desi}(t), t\big) \Big)^2 \, dt \\
& + \frac{1}{2} \int_{T_{start}}^{T_{end}} (\psi_{bd} - \psi_{bd}^0)^2 \, dt \\
& + \frac{1}{2} \int_{T_{start}}^{T_{end}} \sum_{i=1}^{N} \mathbf{D}_i \, V_i(t)^2 \, dt
\end{aligned}
\tag{4.8}
$$

The first term is related to the desired shape evolution. We define one desired boundary per time step, using the following method. The final desired boundary is taken from the VACTH reconstruction of shot 53259 during the flat top phase. Then the intermediate desired boundaries are obtained by linear interpolation between the initial and the final ones, using a parameterization introduced in [105]. The evolution of the desired plasma boundary is shown in figure 4.6.

The second term is related to the flux consumption. The desired flux at the plasma boundary, ψ_{bd}^0, is obtained from integrating the experimental loop voltage measurement. It is shown in figure 4.8 (blue).

The third term is a regularization term, where $\mathbf{D}_i = 1 \times 10^{-9}$ are the weights for voltages. The degree of polynomials used as a basis for the voltage waveforms is 5.

4.4.1 Result of the inverse evolution calculation

We have run several inverse evolution calculations with different values of the final time T_{end}, in order to assess how fast the divertor configuration could be obtained. The result shown below is for $T_{end} = T_{start} + 200 \ ms$, which we found to be a good compromise between speed and limits of the coils currents and voltages (control variables). The time step of this inverse evolution simulation is $5 \ ms$.

The evolution of the desired (blue) and obtained (red) plasma boundary is shown in figure 4.7. It can be seen that the desired boundary is well matched at the beginning
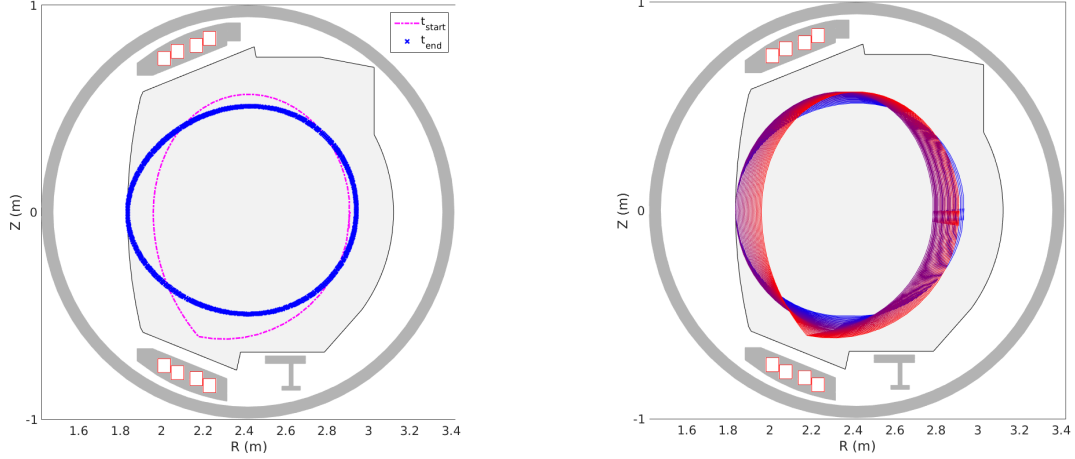
Figure 4.6: Left: the plasma boundary at T_{start} (blue) and the desired boundary at T_{end} (magenta); right: the linear interpolated desired boundaries between T_{start} and T_{end}.

of the time interval $[T_{start}, T_{end}]$. At the end, small deviations are visible, but the final obtained boundary is almost diverted.

The evolution of the plasma boundary flux (red) is compared to the desired values (blue) in figure 4.8. A very good match can be seen.

The trajectory of coils currents is shown in figure 4.9. It can be seen that all coils remain within their limits (and this is also the case for the voltages, which are not shown here), although the Eh and Eb coils approach their maximal positive currents. The A, Bh and Bb coils currents are ramped down to provide the main flux variation. As could be expected, the Xh and Xb coils currents are ramped up in order to elongate and divert the plasma, and Xb is ramped up faster than Xh in order to produce a LSN configuration. The Dh and Db currents are almost opposite to each other, meaning that the code uses these coils to produce an essentially radial magnetic field to control the vertical position of the plasma. On the other hand, the currents in the E and F coils are approximately up-down symmetric, meaning that the code uses these coils to produce an essentially vertical field to control the radial position of the plasma.
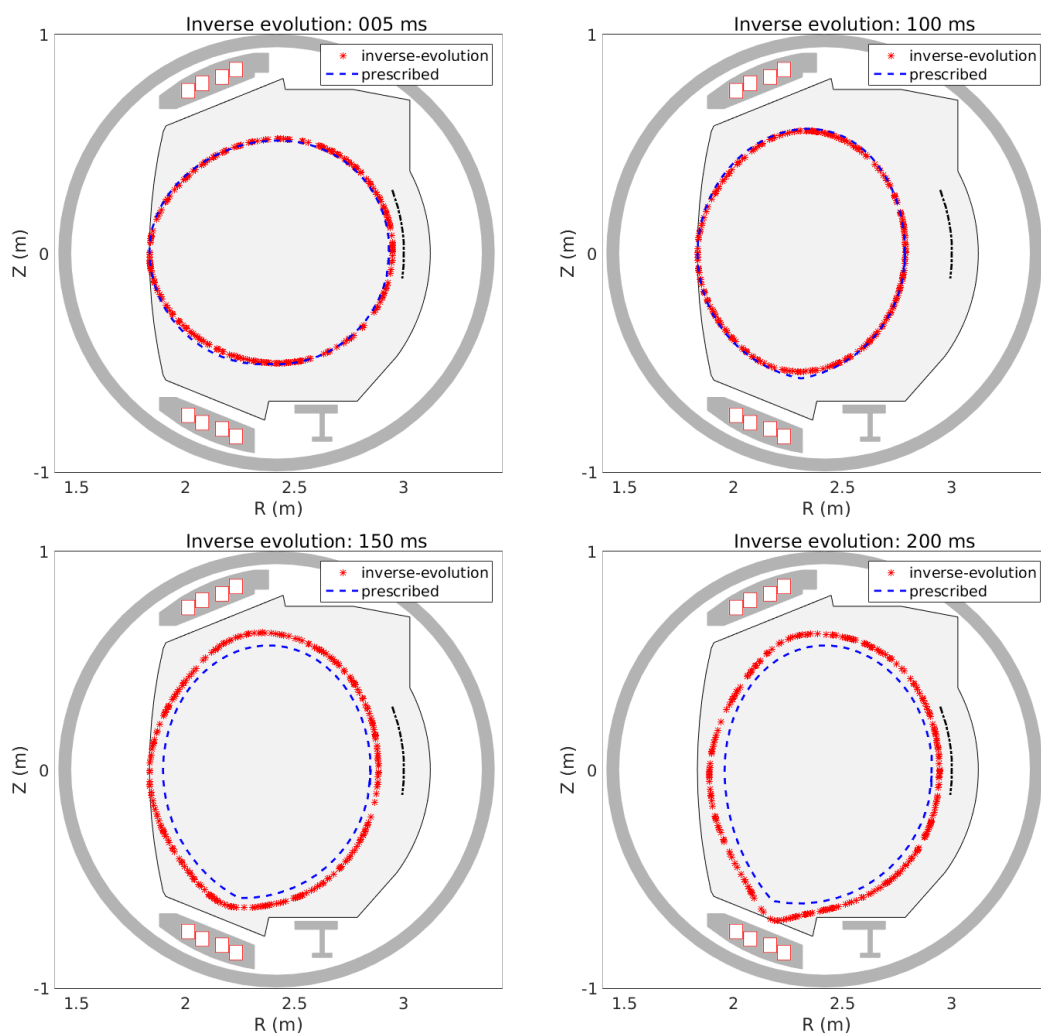
Figure 4.7: Evolution of the plasma boundary from the result of the *inverse evolution* calculation with FEEQS.M (red '*') compared to the desired boundary (blue '-'). The black dots at the LFS are the movable limiter.
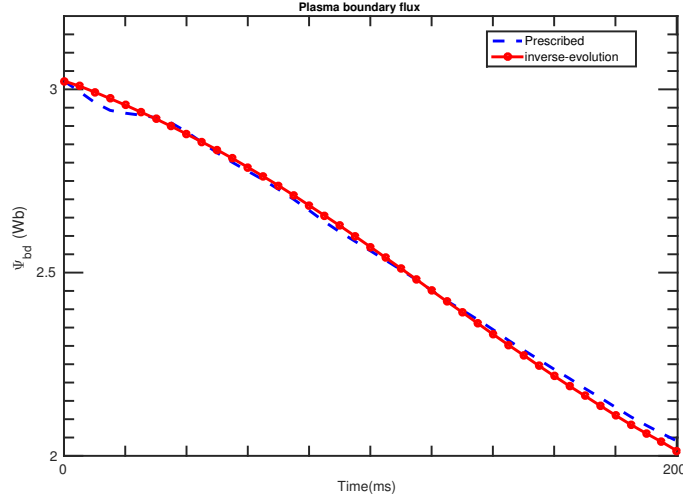
Figure 4.8: **The trajectory of plasma boundary flux** ψ_{bd} **from the result of the** *inverse evolution* **calculation with FEEQS.M (red '-•') compared to its desired value (blue '-').** -

4.5 Testing the fast limiter-divertor transition in simulation

Before applying the I_{coils}^{FF} computed with the inverse evolution mode of FEEQS.M on a real WEST experiment, it is useful to test them in simulation. In this section, we first introduce the WEST magnetic control simulator [99] which we use for this purpose, before presenting the result of our test.

4.5.1 WEST magnetic control simulator

The WEST magnetic control simulator is identical to the real WEST in what concerns the control scheme (the C++ real-time control algorithms are actually compiled from the Matlab Simulink control programs implemented in the simulator). In order to calculate the plasma evolution, the simulator uses FEEQS.M in the *direct evolution* mode (see **Chapter 2.2**). A simple schematic diagram of the WEST magnetic control simulator is shown in figure 4.10.

In order to initialize the simulator, we need an initial equilibrium ψ_0 map. For this

Figure 4.9: The trajectory of coils currents from the result of the inverse evolution calculation with FEEQS.M. - Red '-' lines indicate the limits.
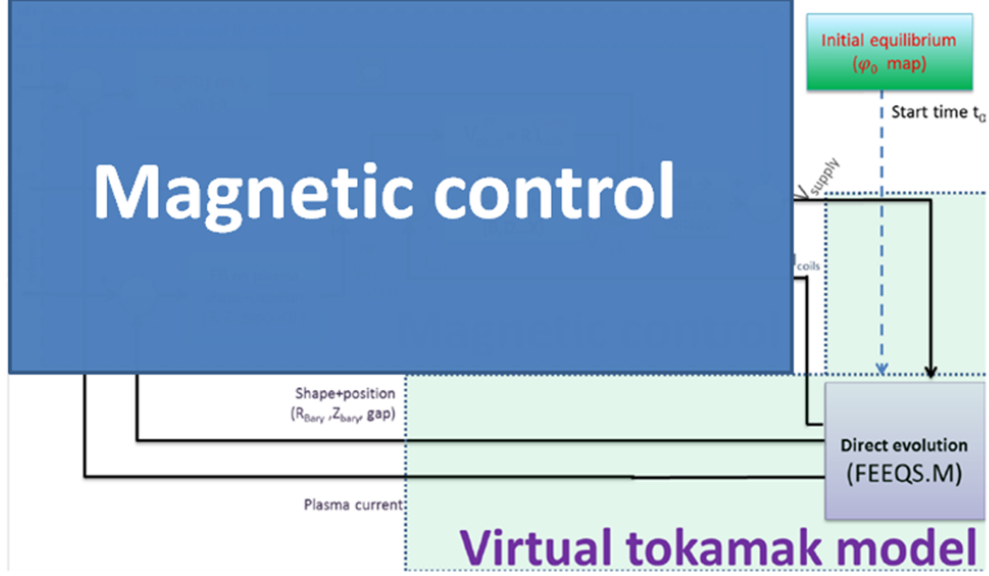
Figure 4.10: The block diagram of WEST virtual magnetic control loop. - The
magnetic control module is the same as the one shown in figure 4.1.

purpose, the same method as described in section 4.3.1 is applied.

The evolution of the plasma current in the simulator is calculated according to the
following simple model [104]:

$$\begin{pmatrix} L_P & M_{P,A} \\ M_{P,A} & L_A \end{pmatrix} \begin{pmatrix} \partial_t I_P \\ \partial_t I_A \end{pmatrix} = \begin{pmatrix} -R_P & 0 \\ 0 & -R_A \end{pmatrix} \begin{pmatrix} I_P \\ I_A \end{pmatrix} + \begin{pmatrix} R_P & 0 \\ 0 & 1 \end{pmatrix} \begin{pmatrix} I_{P,ni} \\ V_{G0} \end{pmatrix} \qquad (4.9)$$

where L_P and L_A (respectively R_P and R_A) are the plasma and A coil self-inductances
(resp. resistances), $M_{P,A}$ is the mutual inductance between the plasma and the A coil,
$I_{P,ni}$ is the non-inductive plasma current, and V_{G0} is the voltage applied to the A coil.
The trajectory of R_P and L_P is fitted from experimental data with following equations:

$$V_{loop} = (I_P - I_{P,ni}) \cdot R_P + L_P \cdot \partial_t I_P$$
$$L_P = \mu_0 R_0 \left(\ln(8\frac{R_0}{a} \sqrt{\frac{2}{1+\kappa^2}}) - 2 + \frac{l_i(3)}{2} \right) \qquad (4.10)$$

where V_{loop}, I_P, a, κ (elongation), R_0 and $l_i(3)$ are taken from experimental data, and
the $I_{P,ni}$ is 0, since we consider an Ohmic discharge.

The evolution of the α, β and γ parameters is set up in the same way as described in section 4.3.2.

4.5.2   Replay of WEST shot 53259 with the simulator

Before testing our new FF coils currents waveforms, we first use the simulator to simply "replay" shot 53259, i.e. we perform a simulation in which the nominal control objects (I_{coils}^{FF}, I_P, plasma position and shape, ...), are read from the WEST pulse scheduling system.

The trajectory of the controlled parameters, i.e. I_P and the R and Z coordinates of the plasma center, as well as the loop voltage are presented in figure 4.12 for the simulation (blue) and experiment (red). It can be seen that I_P is very well matched and so is the loop voltage. The evolution of the plasma shape in the simulation is compared to the experimental one during the limiter to divertor transition in figure 4.11. The evolution is qualitatively similar but some differences are visible. In particular, a mismatch exists at the very beginning of the simulation, which is probably related to a difficulty with the initialization of the integral terms in the control algorithms. Later on, it can be seen that the external major radius of the plasma at the midplane is smaller in the simulation than in the experiment. This is likely caused by the fact that the plasma position which is used for the feedback control is taken directly from FEEQS.M in the simulator, whereas it is obtained from the VACTH reconstruction in the experiment. Finally, a clear mismatch in the vertical position of the plasma can be seen around $34.0\,s$, which is also visible in figure 4.12. This is related to the fact that the plasma makes a downward vertical excursion during this period. This excursion is caused by an incompatibility of the FF coils currents used in the experiment with the request to maintain the plasma vertically centered (FF waveforms have since then been improved to reduce this excursion). The controller therefore has to find a compromise between FF coils currents and the vertical plasma position. Clearly, the simulator does not react in the same way as the real machine, for reasons which are not entirely clear. Later in time, the match between the simulated and experimental boundaries is much better. This is already visible in the last plot of figure 4.11 and can also be guessed from the good match in the plasma R and Z after about $34.5\,s$ in figure 4.12.

The experimental and simulated evolution of coils voltages (left) and currents (right) is shown in figure 4.13. Both voltages and currents are well matched, especially the
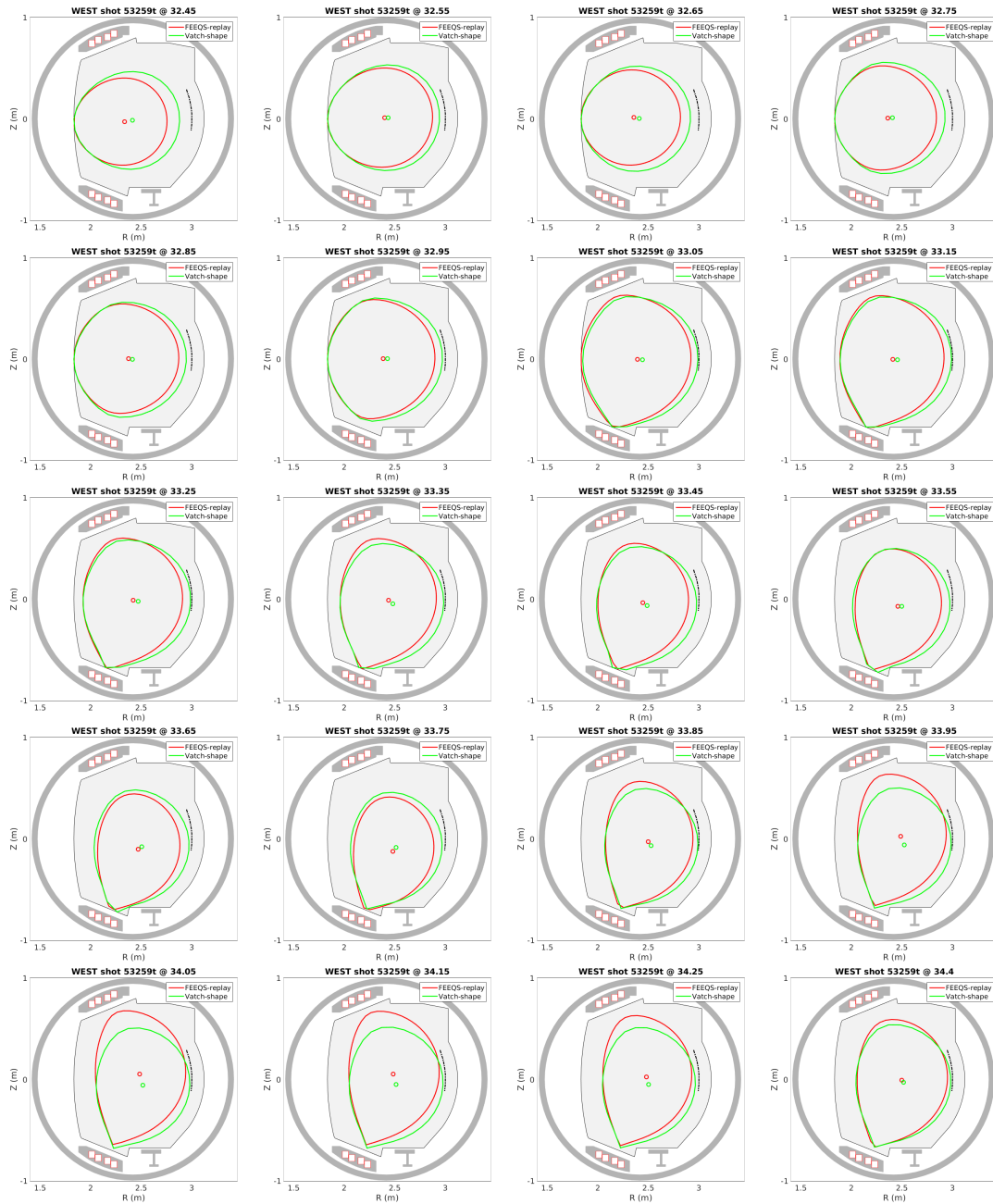
Figure 4.11: Plasma shape evolution: simulation (red) and real data (green) for the WEST shot 53259.
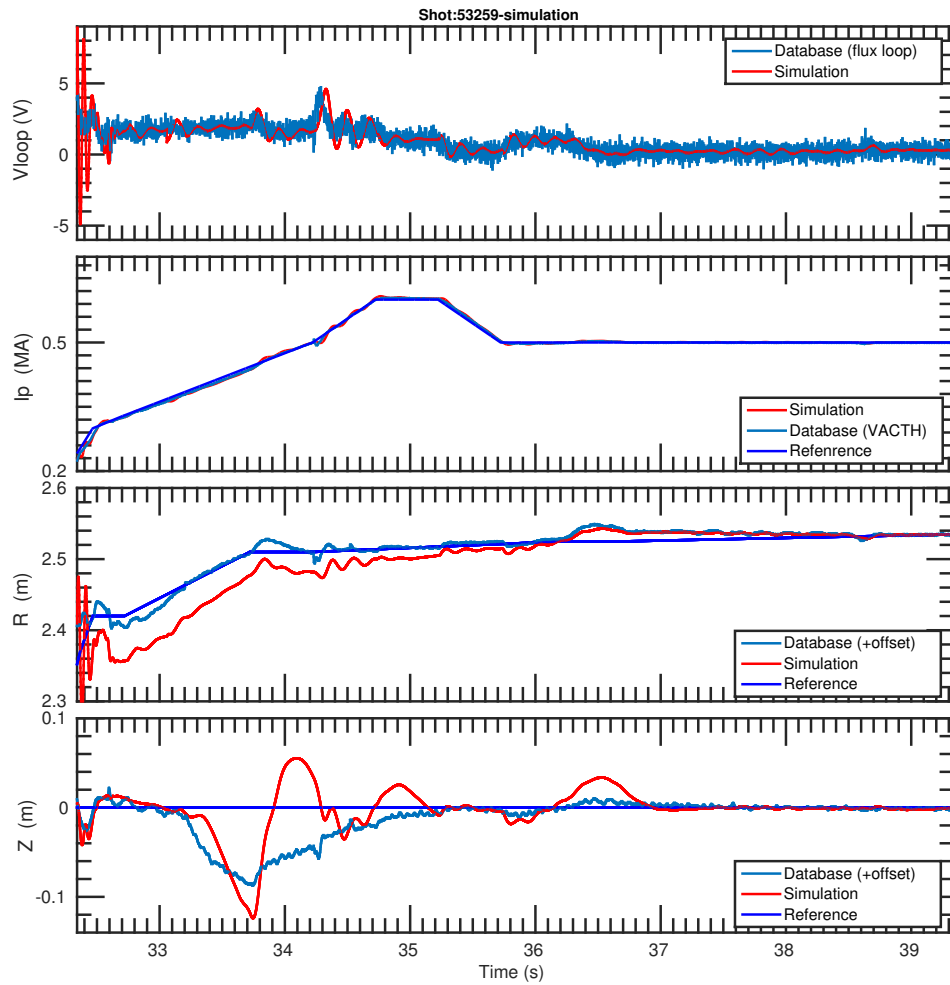
Figure 4.12: Trajectory of loop voltage, I_P, R and Z (plasma center) between experimental data (blue) and simulation (red). -
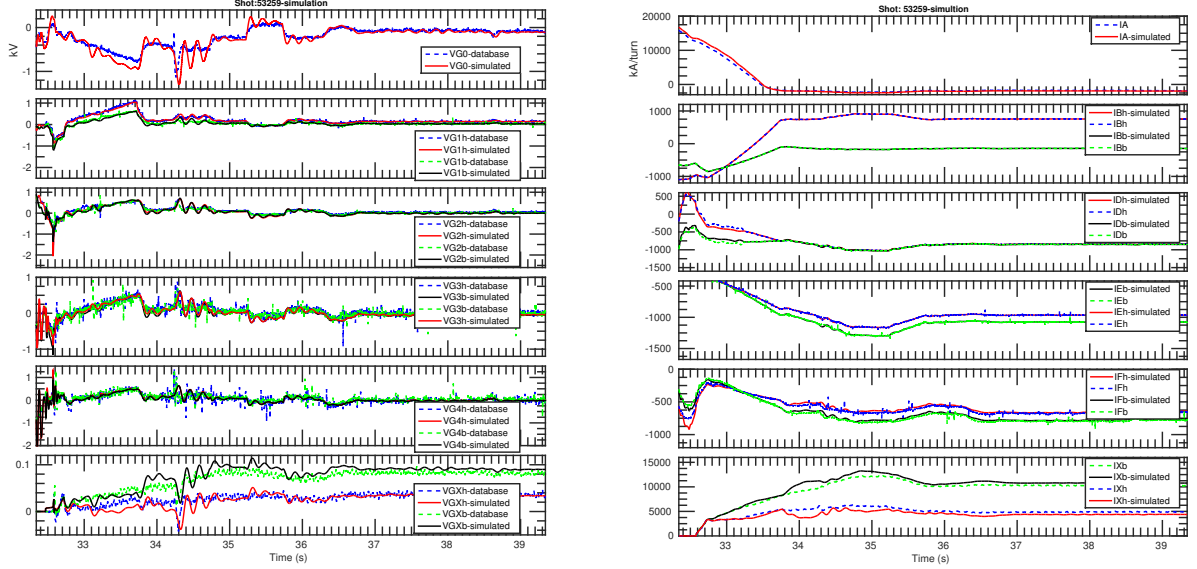
Figure 4.13: Trajectory of experimental (plain) and simulated (dash) voltages (left) and currents (right).

currents, except for mild deviations in X coils around 34 s when the plasma makes the vertical excursion mentioned above.

We conclude from this "replay" exercise that the WEST magnetic control simulator is rather consistent with experimental data, although it does not behave exactly in the same way as the real machine. Still, we consider that it is a valuable test bed for our FF coils currents waveforms.

4.5.3   Results of the test

We now replace in the simulator the I_{coils}^{FF} waveforms from pulse 53259 by the ones from our inverse evolution calculation (except for the A coil) from T_{start} to T_{end}. After T_{end}, we set I_{coils}^{FF} as equal to their values at T_{end}, which we scale in proportion to I_P, in order to maintain the plasma shape. Note that we keep the same reference of R and Z as in shot 53259. Another option is to use the R and Z from the inverse evolution calculation, but this does not change the result dramatically.

The plasma boundary obtained with the simulator (red) is compared to the desired

boundary used in the inverse evolution calculation (blue between T_{start} and T_{end}, green after - the green line is the desired boundary at T_{end}) in figure 4.14. It can be seen that the plasma shape evolves in a similar way to the desired one. In particular, the shape at t=T_{end}=32.78 s is well matched, showing that the I^{FF}_{coils} from the inverse evolution calculation allow obtaining a diverted configuration much earlier than in pulse 53259 ($\approx$ 0.6 s vs. 1.1 s after the plasma breakdown). A significant vertical excursion is observed right after T_{end}. This is due to the fact that the actuators for the vertical position control change from the D coils to the X coils at this time (this change is activated when the current in the X coils overcomes 6 kA/turn, which fortuitously happens right after T_{end}). However, the FB control system brings back the plasma to the desired position within 50 ms. The plasma shape is then well maintained for the rest of the simulation.

The trajectory of controlled plasma parameters, i.e. I_P, R and Z, is shown in figure 4.15. They match the desired values reasonably well. The most obvious discrepancies are the one related to the above mentioned vertical excursion right after T_{end} as well as a steady mismatch in R and Z by several centimeters at the end of the simulation. We however stress that the simulation time here is only of 1 s. These discrepancies will be taken care of by the integral terms of the FB control laws (as in the simulation shown in figure 4.12).

Figure 4.16 shows the FF (from the inverse evolution calculation) and simulated coils currents (except I_A). A moderate mismatch is visible in the first 100 ms, but the FF coils currents are rather well tracked after that.

We conclude from this test that the I^{FF}_{coils} from the inverse evolution simulation are reasonable and worth being tested experimentally.

4.6 Experimental test of the fast limiter-divertor transition on WEST

In the previous section, we have tested in simulation the possibility of reaching a divertor configuration only 600 ms after the breakdown thanks to the I^{FF}_{coils} provided by our inverse evolution calculation (combined with the WEST FB control scheme). We will now test this experimentally.

Figure 4.14: Evolution of plasma boundary from the virtual simulation loop (red) and the inverse evolution calculation (blue between T_{start} and T_{end}, green after).

Figure 4.15: Reference (red '-') and simulated (blue plain) trajectory of I_P, R and Z (plasma center). -

Figure 4.16: Reference (dashed) and simulated (plain) trajectories of coils currents (except A). -

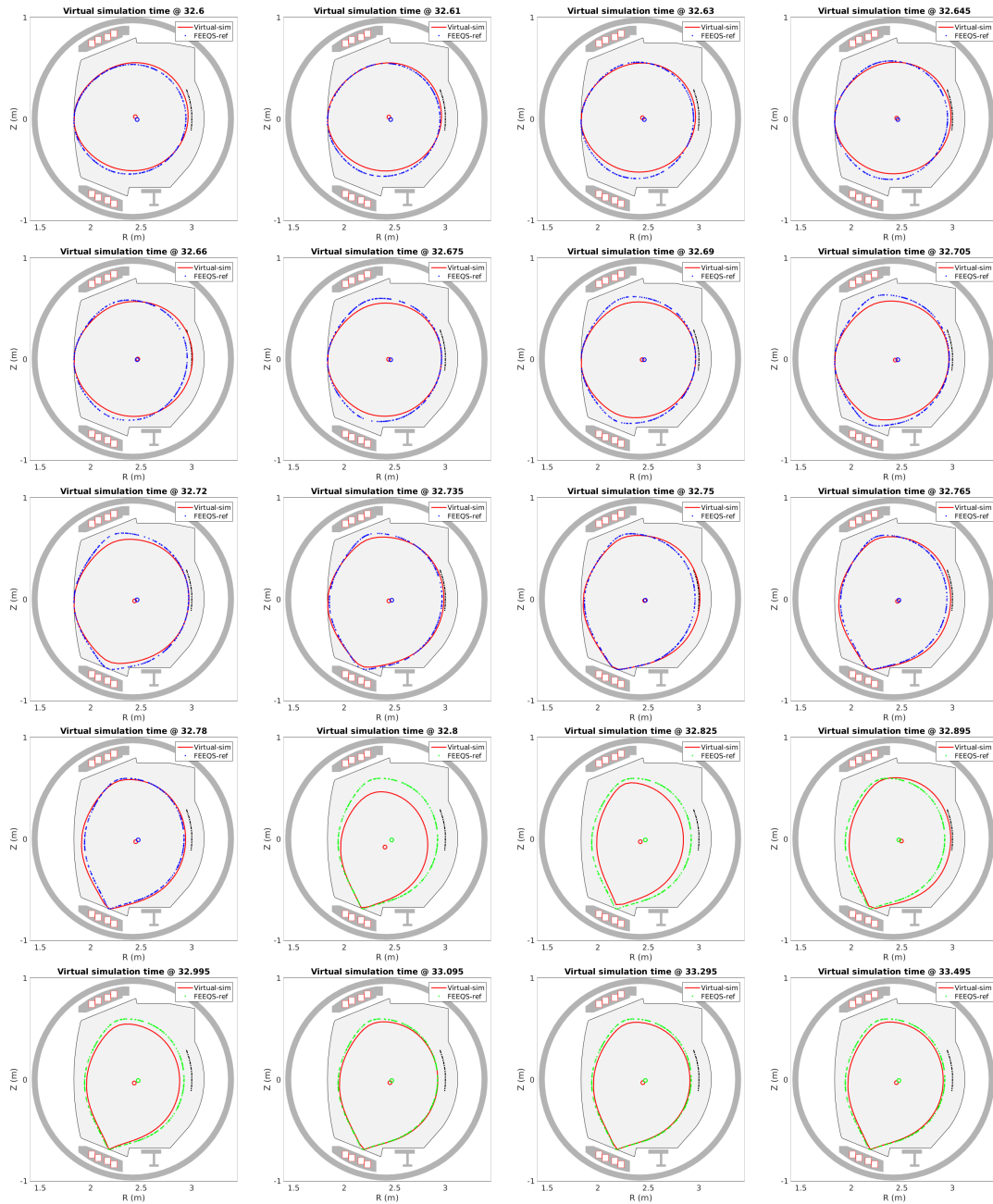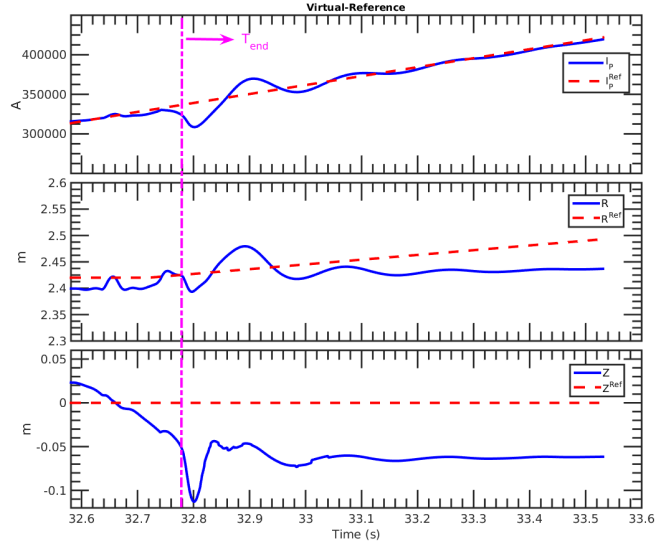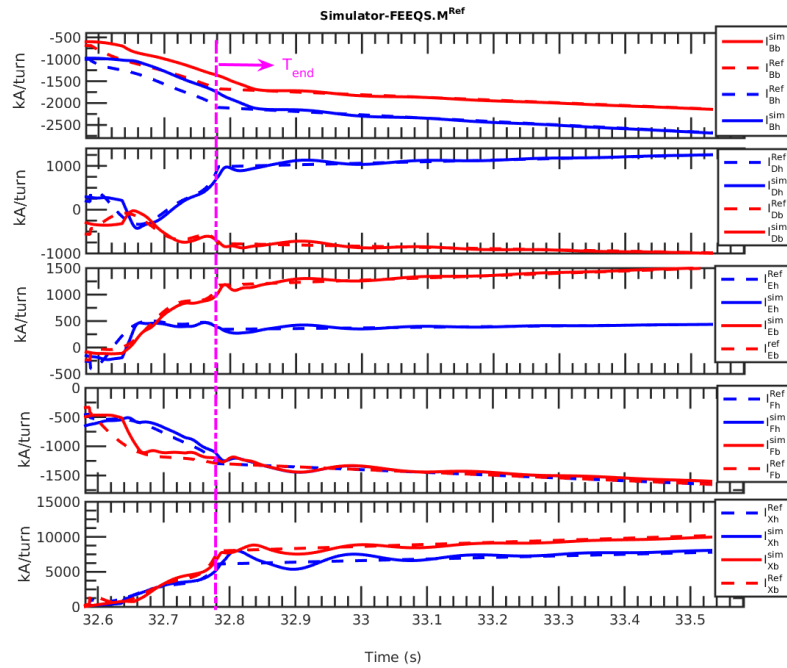## 4. DEVELOPMENT OF A FAST LIMITER TO DIVERTOR TRANSITION IN WEST

For this purpose, I_{coils}^{FF} waveforms from an inverse evolution calculation (slightly different from the one used above) have been implemented in the pulse schedule of WEST shots between $T_{start} = t_0 + 0.4\,s$ and $T_{end} = T_{start} + 0.2\,s$, where t_0 is the plasma breakdown time (the so-called "ignitron" time more precisely).

The first attempt was in shot 53423. Unfortunately, the result was a loss of vertical control around T_{end} leading to a downward vertical displacement event (VDE). This behavior, which had not been observed with the simulator, may be interpreted as a sign that the real machine is more sensitive than the simulator in terms of vertical control. That said, the simulator results shown in figures 4.12 and 4.15 already pointed to vertical control issues. It should be noted that this phase of the pulse is particularly sensitive regarding vertical control. Indeed, this is a very dynamic phase: I_P is ramping up and the plasma shape and position are changing rapidly. Furthermore, the actuators for the vertical FB control during this phase are the rather inefficient D coils, since the X coils take over only when their currents overcome 6 kA/turn. Of course, the vertical control issue becomes more severe as we try to speed up the transition to divertor configuration.

Based on this result, the pragmatic decision was made to keep the same I_{coils}^{FF} waveforms but adjust the vertical position reference (Z^{Ref}) waveform: instead of using $Z^{Ref} = 0$, a Z^{Ref} ramp up by $10cm$ between T_{start} and T_{end} was introduced. This allowed avoiding the VDE in shot 53439, which we describe below.

Figure 4.17 shows the evolution of the plasma boundary from the VATCH reconstruction of WEST shot 53439 (red), compared to the desired boundary used in the inverse evolution calculation (blue between T_{start} and T_{end} and cyan after). The first 3 rows show the period $[T_{start},T_{end}]$, while the following rows are after T_{end} (the cyan dashed line indicates the desired boundary at T_{end} for reference). Figure 4.18 shows the reference (red) and experimental (blue) trajectories of I_P, R and Z (plasma center). Finally, figure 4.19 shows the FF (dashed) and experimental (plain) trajectories of the coils currents (except A).

It can be seen in figure 4.17 that the desired boundary is rather well matched during the first half of the $[T_{start},T_{end}]$ period. After this, the plasma moves upward and therefore does not well match the desired boundary anymore. This vertical movement, which can be seen in the third and forth panels of figure 4.18, is essentially due to the Z^{Ref} ramp up which we have introduced to avoid the VDE, as discussed above. The
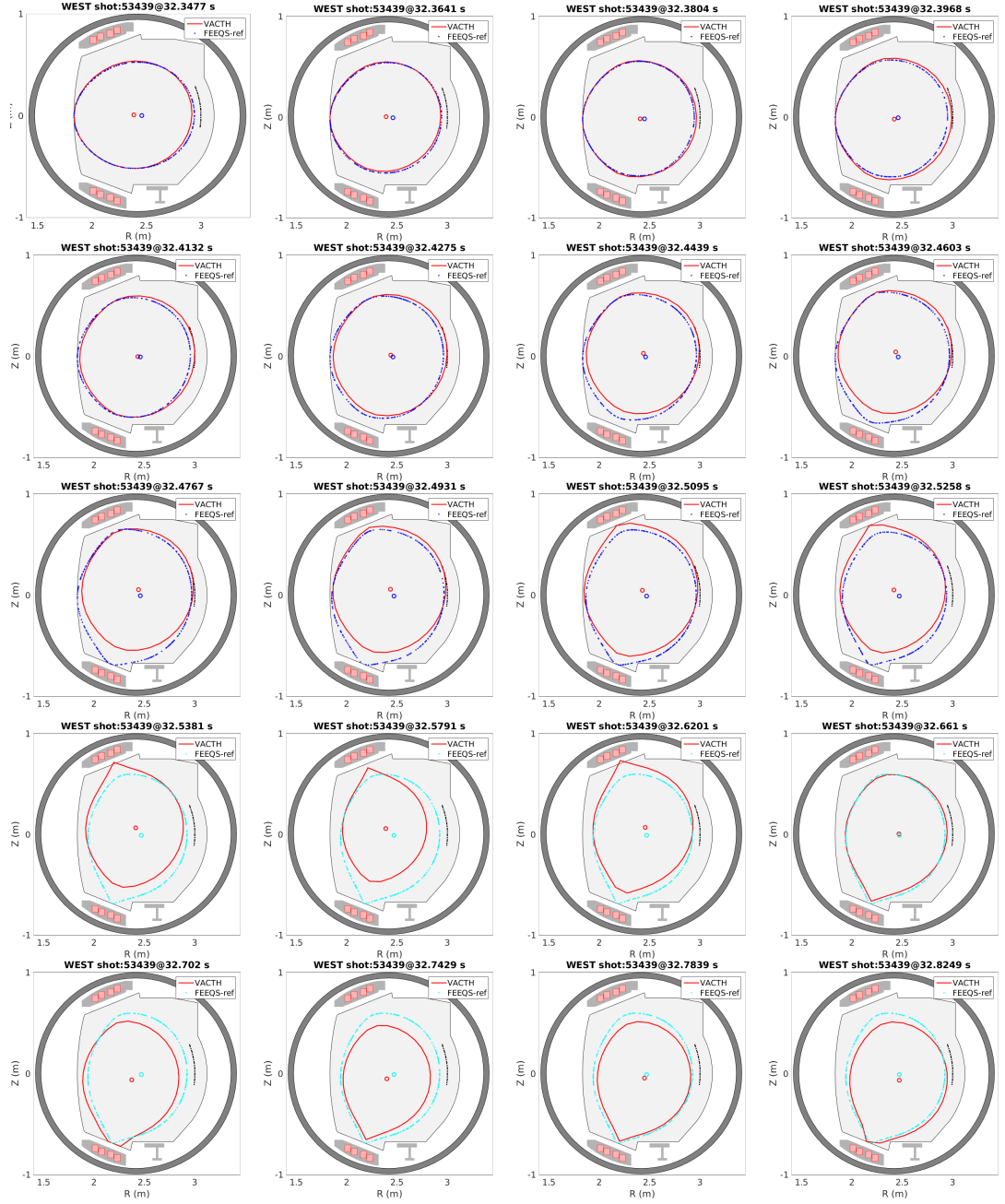
Figure 4.17: Evolution of plasma boundary from the VACTH reconstruction (red) of WEST shot 53439 compared to the desired boundary used in the *inverse evolution* calculation of FEEQS.M (blue between T_{start} and T_{end} and cyan after).

vertical FB control system "struggles" to maintain the plasma in place, but eventually succeeds. This struggle is visible in the somewhat erratic behavior of I_P, R and Z, as well as in coils currents deviations from the FF waveforms. Altogether, the transition to the divertor configuration is therefore not smooth, in particular with the plasma making contact at times with the antennae protection limiter on the LFS as well as with the upper divertor plate. However, the divertor configuration is obtained several hundreds of ms earlier than in shot 53259, which is an encouraging result.
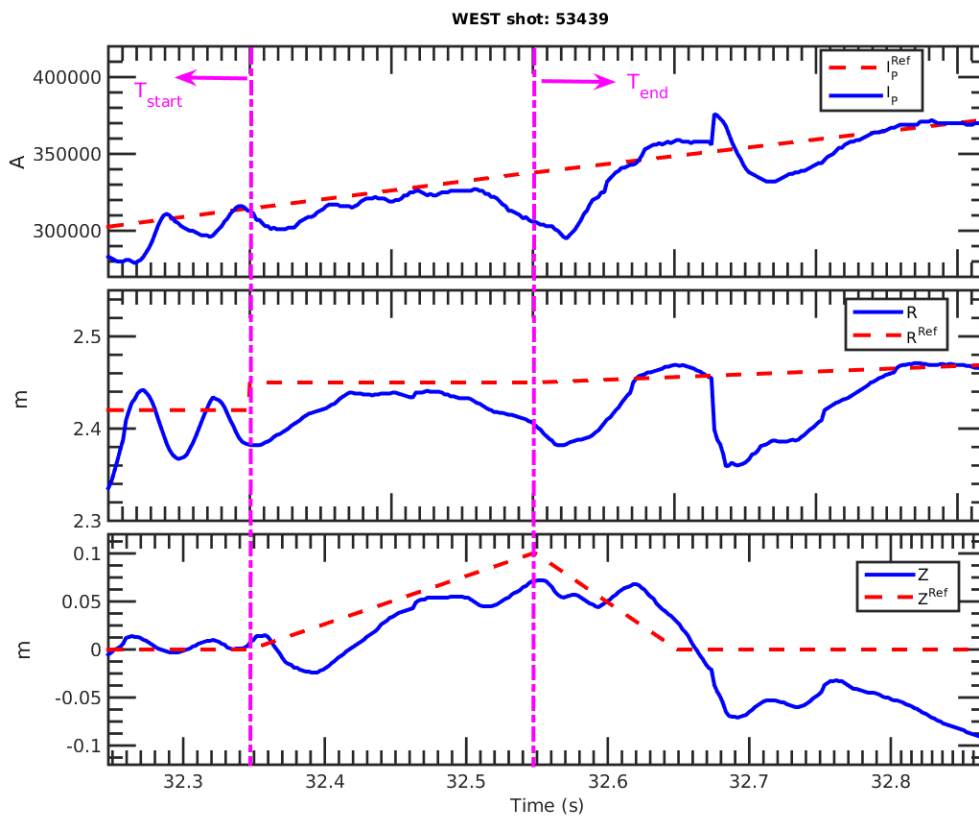
Figure 4.18: Reference (red '-') and experimental (blue plain) trajectories of I_P, R and Z (plasma center) in WEST shot 53439. -
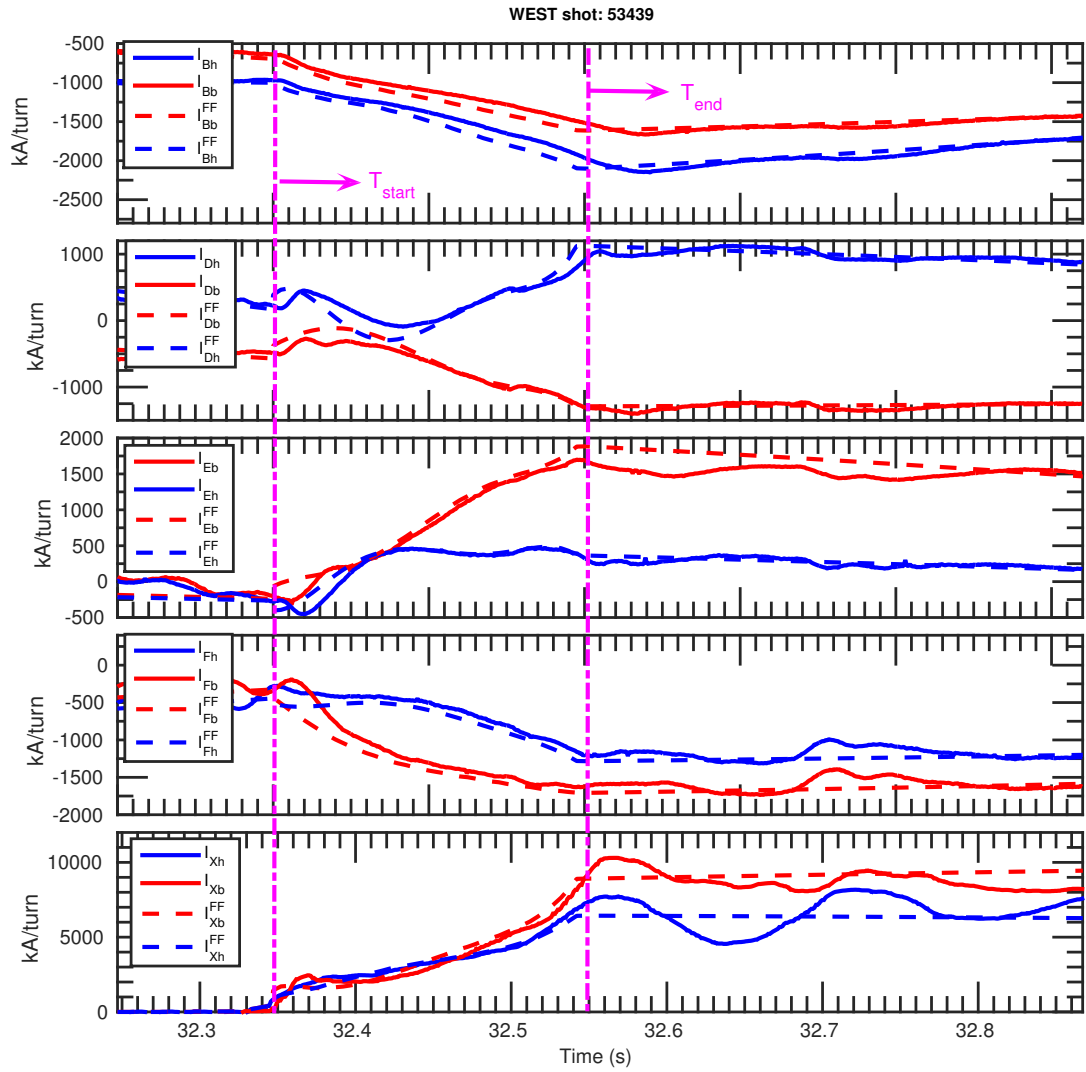
Figure 4.19: Feedforward (dashed) and experimental (plain) trajectories of the coils currents (except A) in WEST shot 53439. -

4.7 Summary and discussion

In this chapter, we have tested for the first time FF coils currents waveforms from an inverse evolution calculation with FEEQS.M in a real tokamak. We have chosen to address the problem of accelerating the formation of a divertor configuration at the beginning of a pulse in WEST, which may be beneficial to reduce plasma contamination by impurities. Before applying the I_{coils}^{FF} on the real machine, we have tested them in a simulator. The tests, both in the simulator and in the real machine, are partly successful in the sense that a divertor configuration is indeed obtained several hundreds of ms faster than "usual". However, the transition is not very smooth, and would need to be improved before being used routinely. It should be said that very limited experimental time (4 shots in total) has been devoted to this study.

Several directions may be suggested to make the transition smoother. A simple pragmatic approach could be to try to adjust experimentally the Z^{Ref} waveform without changing the I_{coils}^{FF}. Another option could be to change the **objective** function in the inverse evolution calculation so as to improve the vertical stability. Of course, the exploration of the various options would benefit from a more accurate WEST simulator.

Chapter 5

Summary and outlook

The results presented in this manuscript show the potential of optimal control methods, and their implementation in the FEEQS.M code, to support tokamak operation.

In particular, after describing the numerical methods and some tests in Chapter 2, we have seen in Chapter 3 that realistic limits of the PF system can be taken into account by means of penalization terms in the cost function of the inverse static mode of FEEQS.M. In this way, the operating space (in terms of plasma equilibrium) can be identified and optimized in an easier and faster way than with previous approaches. We have chosen ITER as a first application case, which allowed us to compare our results with existing ones. We believe that this tool may prove useful in design studies for future tokamaks such as CFETR or in preparation of the operation of new tokamaks like JT60-SA.

In Chapter 4, we have shown that the inverse evolution mode of FEEQS.M can provide optimized FF PF coils currents waveforms which allow obtaining a desired evolution of the plasma shape and position. This inverse evolution mode is a unique feature of FEEQS.M, as far as we know. It may replace the standard method used presently to design such FF waveforms, which typically consists in connecting "by hand" discrete points developed somewhat independently from each other (by means of inverse static calculations for example). As a proof of principle, we have applied the inverse evolution mode to the problem of accelerating the transition to a diverted configuration at the beginning of a WEST pulse. A faster transition has indeed been obtained, although these early results are "polluted" by vertical control issues.

5. SUMMARY AND OUTLOOK

Two main directions can be suggested for near-term future work. The first one is to develop the code and its documentation (and possibly provide trainings) such that tokamak scientists can design and implement by themselves terms for the objective function. Indeed, with the optimal control method, the core of the work lies in choosing and implementing an objective function which accurately translates the constraints or desires of the user.

A second objective could be to evolve from a "proof of principle approach" to a routine application of the inverse evolution mode of FEEQS.M, for example on WEST. The inverse static mode is already applied routinely by WEST Session Leaders (SLs) to develop new plasma shapes in relation with experimental needs. The inverse evolution mode is however more complicated to handle and presently not being used by SLs. To help with this, it would be useful to develop user-friendly procedures and tools (possibly involving a GUI) to run inverse evolution simulations, (optionally) test the FF waveforms in simulation and finally implement them in the experimental pulse schedule.

Appendix A

Circuit Equations

A.1 Circuit Equations

The external circuit of poloidal field coils and suppliers is represented by a directed graph with nodes and directed edges between nodes. We assign to each directed edge $\mathbf{s} = (i, j)$ between two nodes with index i and j a (directed) voltage $V_\mathbf{s}$ and current $I_\mathbf{s}$. For an edge $\mathbf{s}$ representing a coil $\mathcal{C}$ we have

$$I_\mathbf{s} = \mathbf{Z_{ss}} V_\mathbf{s} + (\vec{F}_C(\frac{d}{dt}\psi))_\mathbf{s} := \frac{n_\mathbf{s}}{R_\mathbf{s}} V_\mathbf{s} - 2\pi \frac{n_\mathbf{s}^2}{R_\mathbf{s}} \frac{1}{\mathcal{C}} \int_\mathcal{C} \frac{d}{dt}\psi dr dz \,, \tag{A.1}$$

where $R_\mathbf{s}$ and $n_\mathbf{s}$ are the total resistance and the wire turns of the coil.

Then we introduce the incidence matrix $\mathbf{G}$ that has entry $\mathbf{G}_{\mathbf{s},i} = 0$ when the node with index i is not contained in the edge with index $\mathbf{s} = (i, j)$, or entry $\mathbf{G}_{\mathbf{s},i} = 1(-1)$ when the node with index i is contained in the edge with index $\mathbf{s} = (i, j)$ and induced orientation coincides (coincides not) with the orientation of the edge. Likewise we can introduce oriented polygons, whose boundaries are the edges of the graph and an incidence matrix $\mathbf{C}$ for edges and polygons. Then we have $\mathbf{CG} = 0$ and the Kirchhoff current and voltage laws are:

$$\mathbf{G}^T \vec{I} = 0 \quad \text{and} \quad \mathbf{C}\vec{V} = 0 \,,$$

where the components of $\vec{V}$ and $\vec{I}$ are the voltages and currents associated to the edges.

In the following we assume that the edges of the circuit correspond either to a coil or to an external voltage supplier/source. We introduce the subscripts $_S$ and $_C$ to distinguish between edges corresponding to supplies and edges corresponding to coils,

A. CIRCUIT EQUATIONS

e.g. $\mathbf{G}^T \vec{I} = \mathbf{G}_S^T \vec{I}_S + \mathbf{G}_C^T \vec{I}_C = 0$. Moreover we introduce a (node) potential $\vec{U}$ with $\vec{V} = \mathbf{G}\vec{U}$ and hence $\vec{V}_S = \mathbf{G}_S\vec{U}$ and $\vec{V}_C = \mathbf{G}_C\vec{U}$. In summary we arrive at:

$$\begin{pmatrix} -\mathbf{Z}^{-1} & 0 & \mathbf{G}_C \\ 0 & 0 & \mathbf{G}_S \\ \mathbf{G}_C^T & \mathbf{G}_S^T & 0 \end{pmatrix} \begin{pmatrix} \vec{I}_C \\ \vec{I}_S \\ \vec{U} \end{pmatrix} = \begin{pmatrix} -\mathbf{Z}^{-1}\vec{F}_C(\frac{d}{dt}\psi) \\ \vec{V}_S \\ 0 \end{pmatrix}. \tag{A.2}$$

or, to be close with the notation from CEDRES++,

$$\begin{pmatrix} -\mathbf{Z}^{-1} & 0 \\ 0 & 0 \\ \mathbf{G}_C^T & \mathbf{G}_S^T \end{pmatrix} \begin{pmatrix} \vec{I}_C \\ \vec{I}_S \end{pmatrix} + \begin{pmatrix} \mathbf{G}_C \\ \mathbf{G}_S \\ 0 \end{pmatrix} \begin{pmatrix} \vec{U} \end{pmatrix} = \begin{pmatrix} 0 \\ \vec{V}_S \\ 0 \end{pmatrix} - \begin{pmatrix} \mathbf{Z}^{-1}\vec{F}_C(\frac{d}{dt}\psi) \\ 0 \\ 0 \end{pmatrix}. \tag{A.3}$$

Well-posedness requires to fix $\vec{U}$ at one node and to remove the Kirchoff current equation for the same node. We choose an arbitrary node and fix $\vec{U}$ to zero at this point. This is equivalent to cancel a column (row) in $\mathbf{G}$ ($\mathbf{G}^T$), hence in the subsequent lines $\mathbf{G}$. ($\mathbf{G}^T$) always refers to the reduced matrices.

After some tedious calculations we find

$$\begin{pmatrix} \vec{I}_C \\ \vec{I}_S \\ \vec{U} \end{pmatrix} = \begin{pmatrix} \mathbf{R} & \mathbf{S} & * \\ * & * & * \\ \mathbf{Q} & \mathbf{T} & * \end{pmatrix} \begin{pmatrix} \vec{F}_C(\frac{d}{dt}\psi) \\ \vec{V}_S \\ 0 \end{pmatrix}, \tag{A.4}$$

with

$$\mathbf{R} = \mathbf{I} + \mathbf{Z}\mathbf{G}_C\mathbf{K}\mathbf{G}_C^T + \mathbf{Z}\mathbf{G}_C\mathbf{K}\mathbf{G}_S^T\mathbf{M}\mathbf{G}_S\mathbf{K}\mathbf{G}_C^T$$

$$\mathbf{Q} = \mathbf{G}_C\mathbf{K}\mathbf{G}_C^T + \mathbf{G}_C\mathbf{K}\mathbf{G}_S^T\mathbf{M}\mathbf{G}_S\mathbf{K}\mathbf{G}_C^T$$

and

$$\mathbf{S} = -\mathbf{Z}\mathbf{G}_C\mathbf{K}\mathbf{G}_S^T\mathbf{M}, \qquad \mathbf{T} = -\mathbf{G}_C\mathbf{K}\mathbf{G}_S^T\mathbf{M},$$

where $\mathbf{K}^{-1} = -\mathbf{G}_C^T\mathbf{Z}\mathbf{G}_C$, and $\mathbf{M}^{-1} = -\mathbf{G}_S\mathbf{K}\mathbf{G}_S^T$.

Appendix B

Fast algorithm for optimal control problems

The following section is a short summary on algorithms for general optimal control problems, where we focus on *finite dimensional optimal control problems*. This simplifies considerably the presentation, and is also more relevant for this work as we always work with discretized versions of Problem 4 in **Chapter 2.3**. While most of the subsequent methods are well-known and can be found in excellent text books such as [66, 67, 75], we prefer to include this discussion to keep the presentation self-consistent.

We consider the following generic version of an optimal control problem

$$\min_{\mathbf{u},\mathbf{y}} J(\mathbf{y},\mathbf{u}) \quad \text{s.t.} \quad \mathbf{b}(\mathbf{y},\mathbf{u}) = \mathbf{0}\,, \tag{B.1}$$

where $\mathbf{y} \in \mathbb{R}^n$ and $\mathbf{u} \in \mathbb{R}^m$ are the so-called state and control variables. The constraint $\mathbf{b}(\mathbf{y},\mathbf{u}) = \mathbf{0}$ with $\mathbf{b}(\mathbf{y},\mathbf{u}) \in \mathbb{R}^n$ is the discretization (in space and time) of (2.2), (2.5) and (2.6).

The optimization problem (B.1) is a constrained optimization problem that can be recast as an unconstrained optimization problem. For this we introduce the *reduced* objective function $\widehat{J}(\mathbf{u}) := J(\mathbf{y}(\mathbf{u}),\mathbf{u})$, with $\mathbf{y}(\mathbf{u})$ such that $\mathbf{b}(\mathbf{y}(\mathbf{u}),\mathbf{u}) = \mathbf{0}$. The gradient of $\widehat{J}(\mathbf{u})$ is

$$\widehat{J}_{\mathbf{u}}(\mathbf{u}) = J_{\mathbf{u}}(\mathbf{y}(\mathbf{u}),\mathbf{u}) + J_{\mathbf{y}}(\mathbf{y}(\mathbf{u}),\mathbf{u})\mathbf{y}_{\mathbf{u}}(\mathbf{u})\,.$$

where the subscripts $_{\mathbf{u}}$ and $_{\mathbf{y}}$ indicate the derivatives with respect to $\mathbf{u}$ and $\mathbf{y}$. Some control $\mathbf{u}^*$ is called the stationary point of the reduced objective function if and only if

B. FAST ALGORITHM FOR OPTIMAL CONTROL PROBLEMS

$$\widehat{J}_{\mathbf{u}}(\mathbf{u}^*) = \mathbf{0} \, . \tag{B.2}$$

An iterative approach to the solution of (B.2) faces two major challenges. First, in each iteration we have to solve the full non-linear problem $\mathbf{b}(\mathbf{y}(\mathbf{u}), \mathbf{u}) = \mathbf{0}$ for $\mathbf{y}(\mathbf{u})$ and second, we also need to compute the sensitivities $\mathbf{y}_{\mathbf{u}}(\mathbf{u})$. The second challenge is addressed by the definition of the adjoint state $\mathbf{p}(\mathbf{u}) \in \mathbb{R}^n$ via

$$\mathbf{p}(\mathbf{u}) = -\mathbf{b}_{\mathbf{y}}^{-T}(\mathbf{y}(\mathbf{u})) J_{\mathbf{y}}^{T}(\mathbf{y}(\mathbf{u}), \mathbf{u}) \, . \tag{B.3}$$

We see

$$
\begin{aligned}
0 =& \mathbf{p}^{T}(\mathbf{u}) \left(\mathbf{b}_{\mathbf{u}}(\mathbf{y}(\mathbf{u}), \mathbf{u}) + \mathbf{b}_{\mathbf{y}}(\mathbf{y}(\mathbf{u}), \mathbf{u}) \mathbf{y}_{\mathbf{u}}(\mathbf{u}) \right) \\
=& \mathbf{p}^{T}(\mathbf{u}) \mathbf{b}_{\mathbf{u}}(\mathbf{y}(\mathbf{u}), \mathbf{u}) - J_{\mathbf{y}}(\mathbf{y}(\mathbf{u}), \mathbf{u}) \mathbf{y}_{\mathbf{u}}(\mathbf{u}) \, ,
\end{aligned}
$$

so the gradient of $\widehat{J}(\mathbf{u})$ can also be expressed as

$$\widehat{J}_{\mathbf{u}}(\mathbf{u}) = J_{\mathbf{u}}(\mathbf{y}(\mathbf{u}), \mathbf{u}) + \mathbf{p}^{T}(\mathbf{u}) \mathbf{b}_{\mathbf{u}}(\mathbf{y}(\mathbf{u}), \mathbf{u}) \, . \tag{B.4}$$

The Algorithm 2 sketches the gradient descent. Still, this algorithm requires in each

---

Algorithm 2 Gradient descent

1: $\Delta \mathbf{u} \leftarrow \mathbf{0}$, $\mathbf{y} \leftarrow \mathbf{y}^0$, $\mathbf{u} \leftarrow \mathbf{u}^0$
2: **while** $\|\Delta \mathbf{u}\| / \|\mathbf{u}\| > tol$ **do**
3:     $\Delta \mathbf{y} \leftarrow \mathbf{1}$
4:     **while** $\|\Delta \mathbf{y}\| / \|\mathbf{y}\| > tol$ **do**
5:         $\Delta \mathbf{y} \leftarrow -\mathbf{b}_{\mathbf{y}}^{-1}(\mathbf{y}, \mathbf{u}) \mathbf{b}(\mathbf{y}, \mathbf{u})$
6:         $\mathbf{y} \leftarrow \mathbf{y} + \Delta \mathbf{y}$
7:     **end while**
8:     $\mathbf{p} \leftarrow -\mathbf{b}_{\mathbf{y}}^{-T}(\mathbf{y}, \mathbf{u}) J_{\mathbf{y}}^{T}(\mathbf{y}, \mathbf{u})$
9:     $\Delta \mathbf{u} \leftarrow J_{\mathbf{u}}^{T}(\mathbf{y}, \mathbf{u}) + \mathbf{b}_{\mathbf{u}}^{T}(\mathbf{y}, \mathbf{u}) \mathbf{p}$
10:    $\mathbf{u} \leftarrow \mathbf{u} - \Delta \mathbf{u}$
11: **end while**

---

iteration the solution of the non-linear constraint problem $\mathbf{b}(\mathbf{y}(\mathbf{u}), \mathbf{u}) = \mathbf{0}$ and the solution of the linear adjoint problem (B.3) for the evaluation of the reduced gradient $\widehat{J}(\mathbf{u})$. Moreover, the speed of convergence of the gradient descent algorithm is very slow. Fast convergence could be achieved in including second order terms, e.g. the

Hessian $\widehat{J}_{\mathbf{uu}}(\mathbf{u})$ of the reduced objective function:

$$
\begin{aligned}
\widehat{J}_{\mathbf{uu}}(\mathbf{u}) =& \mathbf{Z}^T(\mathbf{u}) \begin{pmatrix} J_{\mathbf{yy}}(\mathbf{y}(\mathbf{u}),\mathbf{u}) & J_{\mathbf{yu}}(\mathbf{y}(\mathbf{u}),\mathbf{u}) \\ J_{\mathbf{uy}}(\mathbf{y}(\mathbf{u}),\mathbf{u}) & J_{\mathbf{uu}}(\mathbf{y}(\mathbf{u}),\mathbf{u}) \end{pmatrix} \mathbf{Z}(\mathbf{u}) \\
&+ \mathbf{Z}^T(\mathbf{u}) \begin{pmatrix} \mathbf{b}_{\mathbf{yy}}^T(\mathbf{y}(\mathbf{u}),\mathbf{u})\mathbf{p}(\mathbf{u}) & \mathbf{b}_{\mathbf{yu}}^T(\mathbf{y}(\mathbf{u}),\mathbf{u})\mathbf{p}(\mathbf{u}) \\ \mathbf{b}_{\mathbf{uy}}^T(\mathbf{y}(\mathbf{u}),\mathbf{u})\mathbf{p}(\mathbf{u}) & \mathbf{b}_{\mathbf{uu}}^T(\mathbf{y}(\mathbf{u}),\mathbf{u})\mathbf{p}(\mathbf{u}) \end{pmatrix} \mathbf{Z}(\mathbf{u})
\end{aligned}
\tag{B.5}
$$

with

$$
\mathbf{Z}(\mathbf{u}) = \begin{pmatrix} -\mathbf{b}_{\mathbf{y}}^{-1}(\mathbf{y}(\mathbf{u}),\mathbf{u})\mathbf{b}_{\mathbf{u}}(\mathbf{y}(\mathbf{u}),\mathbf{u}) \\ \mathbf{1} \end{pmatrix} ,
$$

but the requirement of solving repetitively the non-linear constraints $\mathbf{b}(\mathbf{y}(\mathbf{u}),\mathbf{u}) = \mathbf{0}$ remains a big drawback.

Sequential Quadratic Programming (SQP) is an entirely different approach that avoids this drawback and incorporates at the same time second order information. SQP is one of the most effective methods for non-linear constrained optimization with significant non-linearities in the constraints [66, Chapter 18]. To motivate SQP we recall that the previous discussion shows that the control $\mathbf{u}^*$ is a stationary point of the reduced objective function if and only if there exist states $\mathbf{y}^*$ and adjoint states $\mathbf{p}^*$ such that

$$
\begin{aligned}
J_{\mathbf{y}}^T(\mathbf{y}^*,\mathbf{u}^*) + \mathbf{b}_{\mathbf{y}}^T(\mathbf{y}^*,\mathbf{u}^*)\mathbf{p}^* &= \mathbf{0}, \\
J_{\mathbf{u}}^T(\mathbf{y}^*,\mathbf{u}^*) + \mathbf{b}_{\mathbf{u}}^T(\mathbf{y}^*,\mathbf{u}^*)\mathbf{p}^* &= \mathbf{0}, \\
\mathbf{b}(\mathbf{y}^*,\mathbf{u}^*) &= \mathbf{0},
\end{aligned}
\tag{B.6}
$$

More generally, the first order optimality conditions state that if $\mathbf{J}$ and $\mathbf{b}$ are twice continuously differentiable with Lipschitz continuous second derivatives and $(\mathbf{y}^*,\mathbf{u}^*)$ is a minimizer of (B.1) then there exist $\mathbf{p}^*$ such that (B.6) holds. A Newton-type method for solving (B.6) are iterations of the type

$$
\begin{pmatrix} \mathbf{H}_{\mathbf{yy}}^k & \mathbf{H}_{\mathbf{yu}}^k & \mathbf{b}_{\mathbf{y}}^T(\mathbf{y}^k,\mathbf{u}^k) \\ \mathbf{H}_{\mathbf{uy}}^k & \mathbf{H}_{\mathbf{uu}}^k & \mathbf{b}_{\mathbf{u}}^T(\mathbf{y}^k,\mathbf{u}^k) \\ \mathbf{b}_{\mathbf{y}}(\mathbf{y}^k,\mathbf{u}^k) & \mathbf{b}_{\mathbf{u}}(\mathbf{y}^k,\mathbf{u}^k) & \mathbf{0} \end{pmatrix} \begin{pmatrix} \mathbf{y}^{k+1} - \mathbf{y}^k \\ \mathbf{u}^{k+1} - \mathbf{u}^k \\ \mathbf{p}^{k+1} \end{pmatrix} = - \begin{pmatrix} J_{\mathbf{y}}^T(\mathbf{y}^k,\mathbf{u}^k) \\ J_{\mathbf{u}}^T(\mathbf{y}^k,\mathbf{u}^k) \\ \mathbf{b}(\mathbf{y}^k,\mathbf{u}^k) \end{pmatrix}
\tag{B.7}
$$

with

$$
\begin{aligned}
\begin{pmatrix} \mathbf{H}_{\mathbf{yy}}^k & \mathbf{H}_{\mathbf{yu}}^k \\ \mathbf{H}_{\mathbf{uy}}^k & \mathbf{H}_{\mathbf{uu}}^k \end{pmatrix} :=& \begin{pmatrix} \mathbf{H}_{\mathbf{yy}}(\mathbf{y}^k,\mathbf{u}^k,\mathbf{p}^k) & \mathbf{H}_{\mathbf{yu}}(\mathbf{y}^k,\mathbf{u}^k,\mathbf{p}^k) \\ \mathbf{H}_{\mathbf{uy}}(\mathbf{y}^k,\mathbf{u}^k,\mathbf{p}^k) & \mathbf{H}_{\mathbf{uu}}(\mathbf{y}^k,\mathbf{u}^k,\mathbf{p}^k) \end{pmatrix} := \\
& \begin{pmatrix} J_{\mathbf{yy}}(\mathbf{y}^k,\mathbf{u}^k) & J_{\mathbf{yu}}(\mathbf{y}^k,\mathbf{u}^k) \\ J_{\mathbf{uy}}(\mathbf{y}^k,\mathbf{u}^k) & J_{\mathbf{uu}}(\mathbf{y}^k,\mathbf{u}^k) \end{pmatrix} + \begin{pmatrix} \mathbf{b}_{\mathbf{yy}}^T(\mathbf{y}^k,\mathbf{u}^k)\mathbf{p}^k & \mathbf{b}_{\mathbf{yu}}^T(\mathbf{y}^k,\mathbf{u}^k)\mathbf{p}^k \\ \mathbf{b}_{\mathbf{uy}}^T(\mathbf{y}^k,\mathbf{u}^k)\mathbf{p}^k & \mathbf{b}_{\mathbf{uu}}^T(\mathbf{y}^k,\mathbf{u}^k)\mathbf{p}^k \end{pmatrix} ,
\end{aligned}
$$

which corresponds to the following quadratic optimization problem with linear constraints:

$$\min_{\mathbf{u}^{k+1}, \mathbf{y}^{k+1}} \left(\frac{1}{2} \begin{pmatrix} \mathbf{y}^{k+1} - \mathbf{y}^k \\ \mathbf{u}^{k+1} - \mathbf{u}^k \end{pmatrix}^T \begin{pmatrix} \mathbf{H}_{\mathbf{yy}}^k & \mathbf{H}_{\mathbf{yu}}^k \\ \mathbf{H}_{\mathbf{uy}}^k & \mathbf{H}_{\mathbf{uu}}^k \end{pmatrix} + \begin{pmatrix} J_{\mathbf{y}}^T(\mathbf{y}^k, \mathbf{u}^k) \\ J_{\mathbf{u}}^T(\mathbf{y}^k, \mathbf{u}^k) \end{pmatrix} \right) \begin{pmatrix} \mathbf{y}^{k+1} - \mathbf{y}^k \\ \mathbf{u}^{k+1} - \mathbf{u}^k \end{pmatrix} \right)$$

$$\text{s.t} \quad \mathbf{b}(\mathbf{y}^k, \mathbf{u}^k) + \mathbf{b}_{\mathbf{y}}(\mathbf{y}^k, \mathbf{u}^k)(\mathbf{y}^{k+1} - \mathbf{y}^k) + \mathbf{b}_{\mathbf{u}}(\mathbf{y}^k, \mathbf{u}^k)(\mathbf{u}^{k+1} - \mathbf{u}^k) = \mathbf{0} \,.$$

This sequence of quadratic optimization problems is at the origin of the name *sequential quadratic programming.*

If the linear systems in (B.7) become too large, it is the common practice to pursue the *null space approach* to arrive at the SQP formulation with the reduced Hessian. In introducing

$$\mathbf{Z}_k = \begin{pmatrix} -\mathbf{b}_{\mathbf{y}}^{-1}(\mathbf{y}^k, \mathbf{u}^k)\mathbf{b}_{\mathbf{u}}(\mathbf{y}^k, \mathbf{u}^k) \\ \mathbf{1} \end{pmatrix} \quad \text{and} \quad \mathbf{Y}_k = \begin{pmatrix} -\mathbf{b}_{\mathbf{y}}^{-1}(\mathbf{y}^k, \mathbf{u}^k) \\ \mathbf{0} \end{pmatrix} \tag{B.8}$$

we obtain the identity

$$\begin{pmatrix} \mathbf{y}^{k+1} - \mathbf{y}^k \\ \mathbf{u}^{k+1} - \mathbf{u}^k \end{pmatrix} = \mathbf{Z}_k(\mathbf{u}^{k+1} - \mathbf{u}^k) + \mathbf{Y}_k \mathbf{b}(\mathbf{y}^k, \mathbf{u}^k) \tag{B.9}$$

and find the following linear system for the increment $\mathbf{u}^{k+1} - \mathbf{u}^k$

$$\mathbf{M}(\mathbf{y}^k, \mathbf{u}^k)(\mathbf{u}^{k+1} - \mathbf{u}^k) = -\mathbf{m}(\mathbf{y}^k, \mathbf{u}^k) \tag{B.10}$$

with

$$\mathbf{M}(\mathbf{y}^k, \mathbf{u}^k) := \mathbf{Z}_k^T \begin{pmatrix} \mathbf{H}_{\mathbf{yy}}^k & \mathbf{H}_{\mathbf{yu}}^k \\ \mathbf{H}_{\mathbf{uy}}^k & \mathbf{H}_{\mathbf{uu}}^k \end{pmatrix} \mathbf{Z}_k$$

and

$$\mathbf{m}(\mathbf{y}^k, \mathbf{u}^k) := \mathbf{Z}_k^T \left(\begin{pmatrix} J_{\mathbf{y}}^T(\mathbf{y}^k, \mathbf{u}^k) \\ J_{\mathbf{u}}^T(\mathbf{y}^k, \mathbf{u}^k) \end{pmatrix} + \begin{pmatrix} \mathbf{H}_{\mathbf{yy}}^k & \mathbf{H}_{\mathbf{yu}}^k \\ \mathbf{H}_{\mathbf{uy}}^k & \mathbf{H}_{\mathbf{uu}}^k \end{pmatrix} \mathbf{Y}_k \mathbf{b}(\mathbf{y}^k, \mathbf{u}^k) \right) \,.$$

It is insightful to compare the expressions involved in the reduced formulation (B.10) of SQP to the gradient (B.4) and the Hessian (B.5) of the reduced objective function: the gradient and Hessian of the reduced objective are equal to $\mathbf{m}(\mathbf{y}, \mathbf{u})$ and $\mathbf{M}(\mathbf{y}, \mathbf{u})$ only when the state $\mathbf{y}$ and control $\mathbf{u}$ verify the non-linear direct problem.

In general, iterative methods, such as the conjugate gradient (CG) methods, are used to solve (B.10). Within each iteration step two linear systems corresponding to $\mathbf{b}_{\mathbf{y}}^{-1}(\mathbf{y}^k, \mathbf{u}^k)$ and $\mathbf{b}_{\mathbf{y}}^{-T}(\mathbf{y}^k, \mathbf{u}^k)$ (see Algorithm 3) need to be inverted. The CG algorithm (Algorithm 3) appears different than standard formulations, as we update within the

Algorithm 3 SQP with CG iterative solver (less memory intensive)

1: $\Delta \mathbf{u} \leftarrow 1$, $\Delta \mathbf{y} \leftarrow 1$, $\mathbf{y} \leftarrow \mathbf{y}^0$, $\mathbf{u} \leftarrow \mathbf{u}^0$, $\mathbf{p} \leftarrow \mathbf{p}^0$

2: **while** $\|\Delta \mathbf{u}\|/\|\mathbf{u}\| > tol$, $\|\Delta \mathbf{y}\|/\|\mathbf{y}\| > tol$ **do**

3: $\quad \Delta \mathbf{u} \leftarrow 0$, $\Delta \mathbf{y} \leftarrow -\mathbf{b_y}^{-1}(\mathbf{y}, \mathbf{u})\mathbf{b}(\mathbf{y}, \mathbf{u})$

4: $\quad \Delta \mathbf{p} \leftarrow -\mathbf{b_y}^{-T}(\mathbf{y}, \mathbf{u})(J_{\mathbf{y}}^T(\mathbf{y}, \mathbf{u}) + \mathbf{H_{yy}}(\mathbf{y}, \mathbf{u}, \mathbf{p})\Delta \mathbf{y})$

5: $\quad \mathbf{r} \leftarrow J_{\mathbf{u}}^T(\mathbf{y}, \mathbf{u}) + \mathbf{H_{uy}}(\mathbf{y}, \mathbf{u}, \mathbf{p})\Delta \mathbf{y} + \mathbf{b_u}^T(\mathbf{y}, \mathbf{u})\Delta \mathbf{p}$

6: $\quad \mathbf{s} \leftarrow -\mathbf{r}$

7: $\quad$ **while** $\|\mathbf{r}\| > tol$ **do**

8: $\quad\quad \mathbf{a} \leftarrow -\mathbf{b_y}^{-1}(\mathbf{y}, \mathbf{u})\mathbf{b_u}(\mathbf{y}, \mathbf{u})\mathbf{s}$

9: $\quad\quad \mathbf{b} \leftarrow -\mathbf{b_y}^{-T}(\mathbf{y}, \mathbf{u})(\mathbf{H_{yu}}(\mathbf{y}, \mathbf{u}, \mathbf{p})\mathbf{s} + \mathbf{H_{yy}}(\mathbf{y}, \mathbf{u}, \mathbf{p})\mathbf{a})$

10: $\quad\quad \widetilde{\mathbf{s}} \leftarrow \mathbf{H_{uu}}(\mathbf{y}, \mathbf{u}, \mathbf{p})\mathbf{s} + \mathbf{H_{uy}}(\mathbf{y}, \mathbf{u}, \mathbf{p})\mathbf{a} + \mathbf{b_u}^T(\mathbf{y}, \mathbf{u})\mathbf{b}$

11: $\quad\quad \alpha \leftarrow \frac{\mathbf{r}^T\mathbf{r}}{\mathbf{s}^T\widetilde{\mathbf{s}}}$

12: $\quad\quad \Delta \mathbf{u} \leftarrow \Delta \mathbf{u} + \alpha\mathbf{s}$, $\Delta \mathbf{y} \leftarrow \Delta \mathbf{y} + \alpha\mathbf{a}$, $\Delta \mathbf{p} \leftarrow \Delta \mathbf{p} + \alpha\mathbf{b}$

13: $\quad\quad \widetilde{\mathbf{r}} \leftarrow \mathbf{r} + \alpha\widetilde{\mathbf{s}}$

14: $\quad\quad \beta \leftarrow \frac{\widetilde{\mathbf{r}}^T\widetilde{\mathbf{r}}}{\mathbf{r}^T\mathbf{r}}$

15: $\quad\quad \mathbf{s} \leftarrow -\widetilde{\mathbf{r}} + \beta\mathbf{s}$

16: $\quad\quad \mathbf{r} \leftarrow \widetilde{\mathbf{r}}$

17: $\quad$ **end while**

18: $\quad \mathbf{u} \leftarrow \mathbf{u} + \Delta \mathbf{u}$, $\mathbf{y} \leftarrow \mathbf{y} + \Delta \mathbf{y}$, $\mathbf{p} \leftarrow \Delta \mathbf{p}$

19: **end while**

B. FAST ALGORITHM FOR OPTIMAL CONTROL PROBLEMS

CG-iterations not only the control but also the state unknown. This avoids solving one additional non-linear direct problem after each CG call.

Alternatively, if we have sufficient memory to store $\mathbf{M}(\cdot, \cdot)$, we can compute $\mathbf{M}(\cdot, \cdot)$ explicitly. We never compute neither $\mathbf{b}_{\mathbf{y}}^{-1}(\mathbf{y}^k, \mathbf{u}^k)$ nor $\mathbf{b}_{\mathbf{y}}^{-T}(\mathbf{y}^k, \mathbf{u}^k)$ explicitly. This alternative approach is summarized in Algorithm 4. While the stopping criteria on Algorithm 1, 2, 3 and 4 use the magnitude of the relative increments, other stopping criteria, such as magnitude of relative residuals, could be used. We refer to [106] for details of stopping criteria for Newton-type methods for non-linear problems.

Algorithm 4 SQP with direct solver (memory intensive)

1: $\Delta\mathbf{u} \leftarrow 1$, $\Delta\mathbf{y} \leftarrow 1$, $\mathbf{y} \leftarrow \mathbf{y}^0$, $\mathbf{u} \leftarrow \mathbf{u}^0$, $\mathbf{p} \leftarrow \mathbf{p}^0$

2: **while** $\|\Delta\mathbf{u}\|/\|\mathbf{u}\| > tol$, $\|\Delta\mathbf{y}\|/\|\mathbf{u}\| > tol$ **do**

3:     $(\Delta\mathbf{y}, \mathbf{Y}) \leftarrow -\mathbf{b}_{\mathbf{y}}^{-1}(\mathbf{y}, \mathbf{u})(\mathbf{b}(\mathbf{y}, \mathbf{u}), \mathbf{b}_{\mathbf{u}}(\mathbf{y}, \mathbf{u}))$

4:     $\mathbf{m} \leftarrow J_{\mathbf{u}}^T(\mathbf{y}, \mathbf{u}) + \mathbf{Y}^T J_{\mathbf{y}}^T(\mathbf{y}, \mathbf{u}) + \mathbf{H}_{\mathbf{uy}}(\mathbf{y}, \mathbf{u}, \mathbf{p})\Delta\mathbf{y} + \mathbf{Y}^T \mathbf{H}_{\mathbf{yy}}(\mathbf{y}, \mathbf{u}, \mathbf{p})\Delta\mathbf{y}$

5:     $\mathbf{M} \leftarrow \mathbf{H}_{\mathbf{uu}}(\mathbf{y}, \mathbf{u}, \mathbf{p}) + \mathbf{Y}^T \mathbf{H}_{\mathbf{yu}}(\mathbf{y}, \mathbf{u}, \mathbf{p}) + \mathbf{H}_{\mathbf{uy}}(\mathbf{y}, \mathbf{u}, \mathbf{p})\mathbf{Y} + \mathbf{Y}^T \mathbf{H}_{\mathbf{yy}}(\mathbf{y}, \mathbf{u}, \mathbf{p})\mathbf{Y}$

6:     $\Delta\mathbf{u} \leftarrow -\mathbf{M}^{-1}\mathbf{m}$

7:     $\Delta\mathbf{y} \leftarrow \Delta\mathbf{y} + \mathbf{Y}\Delta\mathbf{u}$

8:     $\mathbf{p} \leftarrow -\mathbf{b}_{\mathbf{y}}^{-T}(\mathbf{y}, \mathbf{u})(J_{\mathbf{y}}^T(\mathbf{y}, \mathbf{u}) + \mathbf{H}_{\mathbf{yy}}(\mathbf{y}, \mathbf{u}, \mathbf{p})\Delta\mathbf{y} + \mathbf{H}_{\mathbf{yu}}(\mathbf{y}, \mathbf{u}, \mathbf{p})\Delta\mathbf{u})$

9:     $\mathbf{u} \leftarrow \mathbf{u} + \Delta\mathbf{u}$

10:     $\mathbf{y} \leftarrow \mathbf{y} + \Delta\mathbf{y}$

11: **end while**

Appendix C

Penalization term for the CS separating force

C.1 Re-expressing the CS separating force constraint in a form compatible with our approach

In ITER, the CS coils $CS3U, CS2U, \ldots CS3L$ undergo electromagnetic forces $F_Z(CS3U)$, $F_Z(CS2U), \ldots F_Z(CS3L)$ (the averaged z-component of the force). The forces $F_Z(up, 1), F_Z(up, 2)$, $\ldots, F_Z(up, 6)$ and $F_Z(dn, 1), F_Z(dn, 2), \ldots, F_Z(dn, 6)$, are based on those forces and their definitions can be found in Chapter 3.1.3. $F_Z(Upward)$ is the maximum value of $(0, F_Z(up, 1), F_Z(up, 2), \ldots, F_Z(up, 6))$, while $F_Z(Downward)$ is the minimum value of $(0, F_Z(dn, 1), F_Z(dn, 2), \ldots, F_Z(dn, 6))$. The separating force on the CS coils is defined as:

$$F_Z(Sep) := \frac{|F_Z(Upward)| + |F_Z(Downward)|}{2} \tag{C.1}$$

with

$$\begin{aligned} F_Z(Upward) &:= \max\left(0, F_Z(up, 1), F_Z(up, 2), \ldots, F_Z(up, 6)\right) \\ F_Z(Downward) &:= \min\left(0, F_Z(dn, 1), F_Z(dn, 2), \ldots, F_Z(dn, 6)\right) \end{aligned} \tag{C.2}$$

C. PENALIZATION TERM FOR THE CS SEPARATING FORCE

We can simplify it as:

$$
\begin{aligned}
|F_Z(Upward)| &= F_Z(Upward) \\
&= \max\Big(0, F_Z(up,1), F_Z(up,2), \ldots, F_Z(up,6)\Big) \geq 0 \\
|F_Z(Downward)| &= -F_Z(Downward) \\
&= -\min\Big(0, F_Z(dn,1), F_Z(dn,2), \ldots, F_Z(dn,6)\Big) \\
&= \max\Big(0, -F_Z(dn,1), -F_Z(dn,2), \ldots, -F_Z(dn,6)\Big) \geq 0
\end{aligned}
\tag{C.3}
$$

Using the following definitions:

$$
\begin{aligned}
F_{Z0}(up,i) &= \max\Big(0, F_Z(up,i)\Big) \quad 1 \leq i \leq 6 \\
F_{Z0}(dn,j) &= \max\Big(0, -F_Z(dn,j)\Big) \quad 1 \leq j \leq 6
\end{aligned}
\tag{C.4}
$$

it is easy to show that:

$$
F_Z(Sep) = \max_{1 \leq i,j \leq 6} \frac{F_{Z0}(up,i) + F_{Z0}(dn,j)}{2}
\tag{C.5}
$$

The inequality $F_Z(Sep) \leq F_{max,Sep}$ (separating force limit) is thus equivalent to the 6×6 inequalities:

$$
\frac{F_{Z0}(up,i) + F_{Z0}(dn,j)}{2} \leq F_{max,Sep} \quad 1 \leq i,j \leq 6
\tag{C.6}
$$

In order to account for the limit on the CS separating force, we therefore use the following penalization terms:

$$
\mathbf{P_{Force-Sep}}(I_{coils}, \psi) = \sum_{i=1}^{6} \sum_{j=1}^{6} f_P\Big(\frac{\frac{F_{Z0}(up,i) + F_{Z0}(dn,j)}{2} - F_{max,Sep}}{|F_{max,Sep}|} \Big)
\tag{C.7}
$$

where f_P represents the penalization function (e.g., *quasi-rectifier* or *quasi-softplus*). This implementation should have roughly the same effect as a single penalization term based directly on $F_Z(Sep)$, but it offers the advantage of being differentiable.

The first and second derivatives are calculated in the forthcoming section.

C.2 Calculation of the derivatives

We are interested to enforce $\max(0, f(y,u)) + \max(0, g(y,u)) \leq C$ via penalty terms. We introduce $f^+(y,u) = \max(0, f(y,u))$ and $f_s(y,u) = \frac{1}{2}(\text{sign}(f(y,u)+1)$ and the first

and second derivatives are:

$$Q_n(y, u) = \max(0, f^+(y, u) + g^+(y, u) - C)^n := Q_1^n(y, u)$$

$$Q_n^{(1,0)}(y, u) = nQ_{n-1}(y, u)\left(f_s(y, u)f^{(1,0)}(y, u) + g_s(y, u)g^{(1,0)}(y, u)\right)$$

$$Q_n^{(0,1)}(y, u) = nQ_{n-1}(y, u)\left(f_s(y, u)f^{(0,1)}(y, u) + g_s(y, u)g^{(0,1)}(y, u)\right)$$

$$Q_n^{(2,0)}(y, u) = n(n-1)Q_{n-2}(y, u)$$
$$\left(f_s(y, u)f^{(1,0)}(y, 0) + g_s(y, u)g^{(1,0)}(y, u))(f_s(y, u)f^{(1,0)}(y, u) + g_s(y, u)g^{(1,0)}(y, u)\right)$$
$$+ nQ_{n-1}(y, u)\left(f_s(y, u)f^{(2,0)}(y, u)) + g_s(y, u)g^{(2,0)}(y, u)\right)$$

$$Q_n^{(1,1)}(y, u) = n(n-1)Q_{n-2}(y, u)$$
$$\left(f_s(y, u)f^{(0,1)}(y, 0) + g_s(y, u)g^{(0,1)}(y, u))(f_s(y, u)f^{(1,0)}(y, u) + g_s(y, u)g^{(1,0)}(y, u)\right)$$
$$+ nQ_{n-1}(y, u)\left(f_s(y, u)f^{(1,1)}(y, u) + g_s(y, u)(g^{(1,1)}(y, u)\right)$$

$$Q_n^{(0,2)}(y, u) = n(n-1)Q_{n-2}(y, u)$$
$$\left(f_s(y, u)f^{(0,1)}(y, 0) + g_s(y, u)g^{(0,1)}(y, u))(f_s(y, u)f^{(0,1)}(y, u) + g_s(y, u)g^{(0,1)}(y, u)\right)$$
$$+ nQ_{n-1}(y, u)\left(f_s(y, u)f^{(0,2)}(y, u)) + g_s(y, u)g^{(0,2)}(y, u)\right)$$

$$(C.8)$$

In FEEQS.M, these derivatives are applied in the **Objective** function, especially for the penalization terms of CS separating force $F_Z(Sep)$.

C. PENALIZATION TERM FOR THE CS SEPARATING FORCE

Bibliography

[1] N NAKIĆENOVIĆ, A GRÜBLER, AND A MCDONALD. *Global energy perspectives.* Cambridge University Press, 1998. 1, 2

[2] J ONGENA AND G V OOST. **Energy for future centuries: prospects for fusion power as a future energy source**. *Fusion science and technology*, **61**[2T]:3–16, 2012. 2

[3] B P GLOBAL. **Statistical review of world energy 2009**, 2009. 2

[4] F JOOS. **The atmospheric carbon dioxide perturbation**. *Europhysics News*, **27**[6]:213–218, 1996. 3

[5] J WESSON AND D J CAMPBELL. *Tokamaks*, **149**. Oxford University Press, 2011. 4

[6] AE COSTLEY. **On the fusion triple product and fusion power gain of tokamak pilot plants and reactors**. *Nuclear Fusion*, **56**[6]:066003, 2016. 4

[7] G H MILLER, E I MOSES, AND C R WUEST. **The national ignition facility**. *Optical Engineering*, **43**[12]:2841–2854, 2004. 4

[8] L SPITZER J. **The stellarator concept**. *The Physics of Fluids*, **1**[4]:253–264, 1958. 4

[9] M KATSURAI AND M YAMADA. **Studies of conceptual spheromak fusion reactors**. *Nuclear Fusion*, **22**[11]:1407, 1982. 4

[10] EDA ITER ET AL. **Plasma operation and control**. *Nuclear Fusion*, **39**[12 ITER physics basis]:2577–2625, 1999. 7

[11] V ERCKMANN AND U GASPARINO. **Electron cyclotron resonance heating and current drive in toroidal fusion plasmas**. *Plasma physics and controlled fusion*, **36**[12]:1869, 1994. 7

[12] D TONY AND V TOON. *Ec-10: Proceedings Of The 10th Joint Workshop On Electron Cyclotron Emission And Electron Cyclotron Resonance*. World Scientific, 1998. 7

[13] J Adam. **Review of tokamak plasma heating by wave damping in the ion cyclotron range of frequency**. *Plasma Physics and Controlled Fusion*, **29**[4]:443, 1987. 7

[14] J-G Wégrowe. **Lower Hybrid Heating and Current Drive: Experimental Results Versus Theoretical Expectations**. *Fusion Technology*, **7**[2]:250–274, 1985. 7

[15] T Oikawa, K Ushigusa, CB Forest, M Nemoto, O Naito, Y Kusama, Y Kamada, K Tobita, S Suzuki, T Fujita, et al. **Heating and non-inductive current drive by negative ion based NBI in JT-60U**. *Nuclear Fusion*, **40**[3Y]:435, 2000. 7

[16] JD Strachan, H Adler, P Alling, C Ancher, H Anderson, JL Anderson, D Ashcroft, Cris W Barnes, G Barnes, S Batha, et al. **Fusion power production from TFTR plasmas fueled with deuterium and tritium**. *Physical review letters*, **72**[22]:3526, 1994. 7

[17] Jet Team et al. **Fusion energy production from a deuterium-tritium plasma in the JET tokamak**. *Nuclear Fusion*, **32**[2]:187, 1992. 7

[18] AE Costley, J Hugill, and PF Buxton. **On the power and size of tokamak fusion pilot plants and reactors**. *Nuclear Fusion*, **55**[3]:033001, 2015. 7

[19] M Wakatani, VS Mukhovatov, KH Burrell, JW Connor, JG Cordey, Yu V Esipchuk, X Garbet, SV Lebedev, M Mori, K Toi, et al. **Plasma confinement and transport**. *Nuclear Fusion*, **39**[12]:2175–2249, 1999. 7

[20] F Wagner, G Becker, K Behringer, D Campbell, A Eberhagen, W Engelhardt, G Fussmann, O Gehre, J Gernhardt, G v Gierke, et al. **Regime of improved confinement and high beta in neutral-beam-heated divertor discharges of the ASDEX tokamak**. *Physical Review Letters*, **49**[19]:1408, 1982. 7

[21] T Kass, S Günter, M Maraschek, W Suttrop, H Zohm, and ASDEX Upgrade Team. **Characteristics of type I and type III ELM precursors in ASDEX upgrade**. *Nuclear fusion*, **38**[1]:111, 1998. 7

[22] M Keilhacker, JET Team, et al. **Latest JET results in deuterium and deuterium-tritium plasmas**. *Plasma Physics and Controlled Fusion*, **39**:B1–B18, 1997. 7

[23] Y Kamada, K Ushigusa, O Naito, Y Neyatani, T Ozeki, K Tobita, S Ishida, R Yoshino, M Kikuchi, M Mori, et al. **Non-inductively current driven H mode with high beta N and high beta p values in JT-60U**. *Nuclear fusion*, **34**[12]:1605, 1994. 7

[24] H Zohm, TH Osborne, KH Burrell, MS Chu, EJ Doyle, P Gohil, DN Hill, LL Lao, AW Leonard, TS Taylor, et al. **ELM studies on DIII-D and a comparison with ASDEX results**. *Nuclear fusion*, **35**[5]:543, 1995. 7

[25] JA Snipes, RS Granetz, M Greenwald, AE Hubbard, IH Hutchinson, J Irby, J Kesner, S Migliuolo, T Sunn Pedersen, J Ramos, et al. **ELMs and fast edge fluctuations in Alcator C-Mod**. *Plasma physics and controlled fusion*, **40**[5]:765, 1998. 7

[26] H Weisen, MJ Dutch, F Hofmann, Y Martin, JM Moret, Ch Nieswand, ZA Pietrzyk, RA Pitts, and A Pochelon. **Effect on confinement of edge-localized modes in TCV**. *Plasma Physics and Controlled Fusion*, **38**[8]:1415, 1996. 7

[27] XR Duan, JQ Dong, LW Yan, XT Ding, QW Yang, J Rao, DQ Liu, WM Xuan, LY Chen, XD Li, et al. **Preliminary results of ELMy H-mode experiments on the HL-2A tokamak**. *Nuclear Fusion*, **50**[9]:095011, 2010. 7

[28] GS Xu, BN Wan, JG Li, XZ Gong, JS Hu, JF Shan, H Li, DK Mansfield, DA Humphreys, Volker Naulin, et al. **Study on H-mode access at low density with lower hybrid current drive and lithium-wall coatings on the EAST superconducting tokamak**. *Nuclear Fusion*, **51**[7]:072001, 2011. 7

[29] SW Yoon, J-W Ahn, YM Jeon, T Suzuki, SH Hahn, WH Ko, KD Lee, JI Chung, YU Nam, J Kim, et al. **Characteristics of the first H-mode discharges in KSTAR**. *Nuclear Fusion*, **51**[11]:113009, 2011. 7

[30] N Holtkamp et al. **An overview of the ITER project**. *Fusion Engineering and Design*, **82**[5-14]:427–434, 2007. 7

[31] G Brumifel. **Financial meltdown imperils reactor: faced with a huge budget shortfall, Europe rethinks future of ITER fusion project**. *Nature*, **465**[7298]:532–534, 2010. 8

[32] M Shimada, DJ Campbell, V Mukhovatov, M Fujiwara, N Kirneva, K Lackner, M Nagami, VD Pustovitov, N Uckan, J Wesley, et al. **Overview and summary**. *Nuclear Fusion*, **47**[6]:S1, 2007. 8, 11

[33] J Bucalossi, M Missirlian, P Moreau, F Samaille, E Tsitrone, D van Houtte, T Batal, C Bourdelle, M Chantant, Y Corre, et al. **The WEST project: Testing ITER divertor high heat flux component technology in a steady state tokamak environment**. *Fusion Engineering and Design*, **89**[7-8]:907–912, 2014. 8

BIBLIOGRAPHY

[34] RJ Dumont, M Goniche, Annika Ekedahl, B Saoutic, JF Artaud, V Basiuk, C Bourdelle, Y Corre, J Decker, D Elbeze, et al. **Multi-megawatt, gigajoule plasma operation in Tore Supra**. *Plasma Physics and Controlled Fusion*, **56**[7]:075020, 2014. 8

[35] C Bourdelle, JF Artaud, V Basiuk, M Bécoulet, S Brémond, J Bucalossi, H Bufferand, G Ciraolo, L Colas, Y Corre, et al. **WEST physics basis**. *Nuclear Fusion*, **55**[6]:063017, 2015. 8, 36

[36] ITER Physics Expert Group on Disrup MHD, ITER Physics Expert Group on Energe Drive, ITER Physics Expert Group on Diagnostics, and ITER Physics Basis Editors. **Chapter 8: Plasma operation and control**. *Nuclear Fusion*, **39**[12]:2577–2625, dec 1999. 11

[37] TC Hender, JC Wesley, J Bialek, A Bondeson, AH Boozer, RJ Buttery, A Garofalo, TP Goodman, RS Granetz, Y Gribov, et al. **MHD stability, operational limits and disruptions**. *Nuclear fusion*, **47**[6]:S128, 2007. 12

[38] M Greenwald. **Density limits in toroidal plasmas**. *Plasma Physics and Controlled Fusion*, **44**[8]:R27, 2002. 12

[39] F Troyon, R Gruber, H Saurenmann, S Semenzato, and S Succi. **MHD-limits to plasma confinement**. *Plasma physics and controlled fusion*, **26**[1A]:209, 1984. 13

[40] Ge Ambrosino and R Albanese. **Magnetic control of plasma current, position, and shape in Tokamaks: a survey or modeling and control approaches**. *IEEE control systems*, **25**[5]:76–92, 2005. 14

[41] R Albanese and F Villone. **The linearized CREATE-L plasma response model for the control of current, position and shape in tokamaks**. *Nuclear Fusion*, **38**[5]:723, 1998. 15

[42] G De Tommasi, BJ Xiao, R Albanese, R Ambrosino, A Castaldo, ZP Luo, A Mele, A Pironti, and QP Yuan. **Model-based plasma vertical stabilization and position control at EAST**. *Fusion Engineering and Design*, **129**:152–157, 2018. 15

[43] M Ariola, A Pironti, et al. *Magnetic control of tokamak plasmas*, **187**. Springer, 2008. 15

[44] Marc A Firestone and Charles E Kessel. **Plasma kinetic control in a tokamak**. *IEEE Transactions on Plasma Science*, **19**[1]:29–41, 1991. 15

[45] Jo B Lister, Alfredo Portone, and Yuri Gribov. **Plasma control in ITER**. *IEEE control systems*, **26**[2]:79–91, 2006. 15

[46] E Maljaars, F Felici, TC Blanken, Christian Galperti, O Sauter, MR De Baar, F Carpanese, TP Goodman, D Kim, SH Kim, et al. **Profile control simulations and experiments on TCV: a controller test environment and results using a model-based predictive controller**. *Nuclear Fusion*, **57**[12]:126063, 2017. 15

[47] Mark D Boyer, J Barton, E Schuster, Tim C Luce, John R Ferron, Michael L Walker, D A Humphreys, Ben G Penaflor, and Robert D Johnson. **First-principles-driven model-based current profile control for the DIII-D tokamak via LQI optimal control**. *Plasma Physics and Controlled Fusion*, **55**[10]:105007, 2013. 15

[48] D Moreau, JF Artaud, JR Ferron, CT Holcomb, DA Humphreys, F Liu, TC Luce, JM Park, R Prater, F Turco, et al. **Combined magnetic and kinetic control of advanced tokamak steady state scenarios based on semi-empirical modelling**. *Nuclear Fusion*, **55**[6]:063011, 2015. 15

[49] D Moreau, Mike L Walker, John R Ferron, F Liu, E Schuster, Justin E Barton, Mark D Boyer, Keith H Burrell, SM Flanagan, P Gohil, et al. **Integrated magnetic and kinetic control of advanced tokamak plasmas on DIII-D based on data-driven models**. *Nuclear Fusion*, **53**[6]:063020, 2013. 15

[50] H Grad and J Hogan. **Classical diffusion in a tokomak**. *Physical review letters*, **24**[24]:1337, 1970. 18

[51] J Blum. **Numerical simulation and optimal control in plasma physics**. 1989. 19, 25, 34, 35

[52] S Jardin. *Computational methods in plasma physics*. CRC Press, 2010. 19

[53] H Grad and H Rubin. **Hydromagnetic equilibria and force-free fields**. *Journal of Nuclear Energy (1954)*, **7**[3-4]:284–285, 1958. 19

[54] VD Shafranov. **On magnetohydrodynamical equilibrium configurations**. *Soviet Phys. JETP*, **6**, 1958. 19

[55] R Lüst and A Schlüter. **Axialsymmetrische magnetohydrodynamische gleichgewichtskonfigurationen**. *Zeitschrift für Naturforschung A*, **12**[10]:850–854, 1957. 19

[56] C Angioni, E Fable, M Greenwald, M Maslov, AG Peeters, H Takenaga, and H Weisen. **Particle transport in tokamak plasmas, theory and experiment**. *Plasma Physics and Controlled Fusion*, **51**[12]:124017, 2009. 20

[57] JL Luxon and BB Brown. **Magnetic analysis of non-circular cross-section tokamaks**. *Nuclear Fusion*, **22**[6]:813, 1982. 21

BIBLIOGRAPHY

[58] PB SNYDER, HR WILSON, TH OSBORNE, AND AW LEONARD. **Characterization of peeling–ballooning stability limits on the pedestal**. *Plasma physics and controlled fusion*, **46**[5A]:A131, 2004. 21

[59] PB SNYDER, RJ GROEBNER, JW HUGHES, TH OSBORNE, M BEURSKENS, AW LEONARD, HR WILSON, AND XQ XU. **A first-principles predictive model of the pedestal height and width: development, testing and ITER optimization with the EPED model**. *Nuclear Fusion*, **51**[10]:103016, 2011. 21

[60] J BLUM, H HEUMANN, E NARDON, AND X SONG. **Automating the design of tokamak experiment scenarios**. *Journal of Computational Physics*, 2019. 25

[61] J BLUM, J LE FOLL, AND B THOORIS. **The self-consistent equilibrium and diffusion code SCED**. *Computer Physics Communications*, **24**[3-4]:235–254, 1981. 25

[62] P HERTOUT, CÉDRIC BOULBE, ERIC NARDON, J BLUM, SYLVAIN BRÉMOND, JÉROME BUCALOSSI, BLAISE FAUGERAS, VIRGINIE GRANDGIRARD, AND P MOREAU. **The CEDRES++ equilibrium code and its application to ITER, JT-60SA and Tore Supra**. *Fusion Engineering and Design*, **86**[6]:1045–1048, 2011. 25

[63] J R SHEWCHUK. **Triangle: Engineering a 2D quality mesh generator and Delaunay triangulator**. In *Applied computational geometry towards geometric engineering*, pages 203–222. Springer, 1996. 25

[64] TIMOTHY A DAVIS. **UMFPACK version 5.2. 0 user guide**. *University of Florida*, 2007. 25

[65] T A DAVIS AND Y HU. **The University of Florida sparse matrix collection**. *ACM Transactions on Mathematical Software (TOMS)*, **38**[1]:1, 2011. 25

[66] J NOCEDAL AND S J WRIGHT. *Sequential quadratic programming*. Springer, 2006. 25, 107, 109

[67] M. HINZE, R. PINNAU, M. ULBRICH, AND S. ULBRICH. *Optimization with PDE constraints*, **23** of *Mathematical Modelling: Theory and Applications*. Springer, New York, 2009. 25, 107

[68] H HEUMANN, J BLUM, C BOULBE, B FAUGERAS, G SELIG, J-M ANÉ, S BRÉMOND, V GRANDGIRARD, P HERTOUT, AND E NARDON. **Quasi-static free-boundary equilibrium of toroidal plasma with CEDRES++: Computational methods and applications**. *Journal of Plasma Physics*, **81**[3], 2015. 25, 30, 33, 61

[69] P HAJŁASZ. **Sobolev spaces on an arbitrary metric space**. *Potential Analysis*, **5**[4]:403–415, 1996. 27

[70] R Albanese, J Blum, and O Barbieri. **On the solution of the magnetic flux equation in an infinite domain**. In *EPS. 8th Europhysics Conference on Computing in Plasma Physics*, pages 41–44, 1986. 28

[71] V Grandgirard. *Modélisation de l'équilibre d'un plasma de tokamak*. PhD thesis, Besançon, 1999. 29, 34, 35

[72] B Faugeras and H Heumann. **FEM-BEM coupling methods for Tokamak plasma axisymmetric free-boundary equilibrium computations in unbounded domains**. *Journal of Computational Physics*, **343**:201–216, 2017. 29

[73] G N Gatica and G C Hsiao. **The Uncoupling of Boundary Integral and Finite Element Methods for Nonlinear Boundary**. *Journal of Mathematical Analysis and Applications*, **189**:442–46, 1995. 29

[74] Karl Lackner. **Computation of ideal MHD equilibria**. *Computer Physics Communications*, **12**[1]:33–44, 1976. 29

[75] J-F Bonnans, J C Gilbert, C Lemaréchal, and C A Sagastizábal. *Numerical optimization: theoretical and practical aspects*. Springer Science & Business Media, 2006. 32, 107

[76] Q Li et al. **The component development status of HL-2M tokamak**. *Fusion Engineering and Design*, **96**:338–342, 2015. 44

[77] X Song, E Nardon, H Heumann, and B Faugeras. **Automatic identification of the plasma equilibrium operating space in tokamaks**. *Fusion Engineering and Design*, 2019. 49

[78] Y Gribov, N Mitchell, C Jong, F Simon, and A Loarte. *CS and PF coils data and requirements to separatrix positioning for analysis of ITER plasma equilibria and poloidal field scenarios*. ITER-D-2ACJT3, Version, 3.2 edition, July 13, 2017. 50, 55

[79] Timothy C Luce, David A Humphreys, Gary L Jackson, and Wayne M Solomon. **Inductive flux usage and its optimization in tokamak operation**. *Nuclear Fusion*, **54**[9]:093005, 2014. 55

[80] Fujieda H et al. **TOSCA equilibrium code**. *Report Japan Atomic Energy Research Institue, Ibaraki, JAERT-M*, pages 08–256 (in Japanese), 1996. 56

[81] TA Casper, WH Meyer, LD Pearlstein, and A Portone. **ITER shape controller and transport simulations**. *Fusion Engineering and Design*, **83**[2-3]:552–556, 2008. 56

[82] G Ambrosino, R Albanese, M Ariola, A Cenedese, F Crisanti, G De Tommasi, Massimiliano Mattei, F Piccolo, A Pironti, F Sartori, et al. **XSC plasma**

control: Tool development for the session leader. *Fusion engineering and design*, **74**[1-4]:521–525, 2005. 56

[83] F Najmabadi, A Abdou, L Bromberg, T Brown, VC Chan, MC Chu, F Dahlgren, L El-Guebaly, P Heitzenroeder, D Henderson, et al. **The ARIES-AT advanced tokamak, advanced technology fusion power plant**. *Fusion Engineering and Design*, **80**[1-4]:3–23, 2006. 56

[84] CE Kessel, D Campbell, Yu Gribov, G Saibene, G Ambrosino, RV Budny, T Casper, M Cavinato, H Fujieda, R Hawryluk, et al. **Development of ITER 15 MA ELMy H-mode inductive scenario**. *Nuclear Fusion*, **49**[8]:085034, 2009. 56, 57, 73

[85] M Mattei, M Cavinato, G Saibene, A Portone, R Albanese, G Ambrosino, LD Horton, C Kessel, F Koechl, PJ Lomas, et al. **ITER operational space for full plasma current H-mode operation**. *Fusion Engineering and Design*, **84**[2]:300–304, 2009. 56, 58, 59

[86] T Casper, Y Gribov, A Kavin, V Lukash, R Khayrutdinov, H Fujieda, C Kessel, ITER Domestic Agencies, et al. **Development of the ITER baseline inductive scenario**. *Nuclear Fusion*, **54**[1]:013005, 2013. 58, 59

[87] Andrew L Maas, Awni Y Hannun, and Andrew Y Ng. **Rectifier nonlinearities improve neural network acoustic models**. In *Proc. icml*, **30**, page 3, 2013. 60

[88] A Senior and X Lei. **Fine context, low-rank, softplus deep neural networks for mobile speech recognition**. In *Acoustics, Speech and Signal Processing (ICASSP), 2014 IEEE International Conference on*, pages 7644–7648. IEEE, 2014. 61

[89] E Joffrin, M Baruzzo, M Beurskens, C Bourdelle, S Brezinsek, J Bucalossi, P Buratti, G Calabro, CD Challis, M Clever, et al. **First scenario development with the JET new ITER-like wall**. *Nuclear fusion*, **54**[1]:013011, 2013. 77

[90] GJ Van Rooij, JW Coenen, L Aho-Mantila, S Brezinsek, M Clever, R Dux, M Groth, K Krieger, S Marsen, GF Matthews, et al. **Tungsten divertor erosion in all metal devices: Lessons from the ITER like wall of JET**. *Journal of Nuclear Materials*, **438**:S42–S47, 2013. 77

[91] GF Matthews, JET EFDA Contributors, et al. **Plasma operation with an all metal first-wall: comparison of an ITER-like wall with a carbon wall in JET**. *Journal of Nuclear Materials*, **438**:S2–S10, 2013. 77

[92] MNA Beurskens, J Schweinzer, C Angioni, A Burckhart, CD Challis, I Chapman, R Fischer, J Flanagan, Lorenzo Frassinetti, C Giroud, et al.

The effect of a metal wall on confinement in JET and ASDEX Upgrade. *Plasma Physics and Controlled Fusion*, **55**[12]:124043, 2013. 77

[93] Rudolf Neu, A Kallenbach, M Balden, V Bobkov, JW Coenen, R Drube, R Dux, H Greuner, A Herrmann, J Hobirk, et al. **Overview on plasma operation with a full tungsten wall in ASDEX Upgrade**. *Journal of Nuclear Materials*, **438**:S34–S41, 2013. 77

[94] O Gruber, ACC Sips, R Dux, T Eich, JC Fuchs, A Herrmann, A Kallenbach, CF Maggi, R Neu, T Pütterich, et al. **Compatibility of ITER scenarios with full tungsten wall in ASDEX Upgrade**. *Nuclear Fusion*, **49**[11]:115014, 2009. 77

[95] JM Ané, V Grandgirard, F Albajar, and J Johner. **Design of next step tokamak: consistent analysis of plasma performance flux composition and poloidal field system**. Technical report, 2001. 77

[96] R Nouailletas, N Ravenel, J Signoret, W Treutterer, A Spring, M Lewerentz, CJ Rapson, H Masand, J Dhongde, P Moreau, et al. **From the conceptual design to the first simulation of the new WEST plasma control system**. *Fusion Engineering and Design*, **96**:680–684, 2015. 78

[97] W Treutterer, R Cole, K Lüddecke, G Neu, C Rapson, G Raupp, D Zasche, T Zehetbauer, and ASDEX Upgrade Team. **ASDEX Upgrade Discharge Control SystemA real-time plasma control framework**. *Fusion Engineering and Design*, **89**[3]:146–154, 2014. 78

[98] E Nardon, H Heumann, JF Artaud, J Bucalossi, D Douai, N Fedorczak, and T Loarer. **Magnetic configuration and plasma start-up in the WEST tokamak**. 78

[99] R Nouailletas, J Colnel, N Ravenel, J Signoret, W Treutterer, P Moreau, F Saint Laurent, E Nardon, C Reux, D Douai, et al. **The WEST plasma control system: Integration, commissioning and operation on first experimental campaigns**. *Fusion Engineering and Design*, 2019. 78, 88

[100] R Nouailletas, E Nardon, P Moreau, C Reux, and T-P-H Truong. **WEST Magnetic Control**. *To be submitted*, 2019. 79, 81

[101] B Faugeras, J Blum, C Boulbe, P Moreau, and E Nardon. **2D interpolation and extrapolation of discrete magnetic measurements with toroidal harmonics for equilibrium reconstruction in a Tokamak**. *Plasma Physics and Controlled Fusion*, **56**[11]:114010, 2014. 79

[102] P Moreau, A Le-Luyer, P Spuig, P Malard, F Saint-Laurent, JF Artaud, J Morales, B Faugeras, H Heumann, B Cantone, et al. **The new magnetic**

diagnostics in the WEST tokamak. *Review of Scientific Instruments*, **89**[10]:10J109, 2018. 79

[103] G De Tommasi, R Albanese, G Ambrosino, M Ariola, Peter J Lomas, A Pironti, F Sartori, and JET-EFDA Contributors. **Current, position, and shape control in tokamaks**. *Fusion Science and Technology*, **59**[3]:486–498, 2011. 81

[104] R Nouailletas, O Barana, F Saint-Laurent, S Brémond, P Moreau, A Ekedahl, and J-F Artaud. **Multi-Inputs/Multi-Outputs control of plasma current and loop voltage on Tore Supra**. *Fusion Engineering and Design*, **88**[6-8]:525–528, 2013. 81, 90

[105] J Johner. **Helios: a zero-dimensional tool for next step and reactor studies**. *Fusion Science and Technology*, **59**[2]:308–349, 2011. 85

[106] P Deuflhard. *Newton methods for nonlinear problems: affine invariance and adaptive algorithms*, **35**. Springer Science & Business Media, 2011. 112